Excitation and superfocusing of the radially polarized conical surface plasmon polaritons

Dissertation
zur Erlangung des akademischen Grades
doctor rerum naturalium (Dr. rer. nat.)

vorgelegt dem Rat der Physikalisch-Astronomischen Fakultät
der Friedrich-Schiller-Universität Jena

von M.Sc Bayarjargal Narantsatsralt Tugchin
geboren am 08.03.1984 in Ulaanbaatar

Gutacher / Referees
1. Prof. Dr. Thomas Pertsch, Friedrich-Schiller-Universität Jena
2. Prof. Dr. Bert Hecht, Universität Würzburg
3. Prof. Dr. Mario Agio, Universität Siegen

Tag der Disputation / Day of defense: 15.05.2018

Contents

1 Introduction

The microscope has, since its conception, been a vital investigative tool for science and technology, and generations of scientist have been and still are investing their efforts to improve its performance and the ability to see better smaller and smaller features. This challenging task can be approached step by step starting with understanding the problem and its conditions. The fundamental resolution limit of an imaging lens has been demonstrated mathematically by Ernst Abbe in 1873.[1] He showed that the smallest feature one can resolve with an objective lens is limited to the imaging wavelength (λ) over twice the numerical aperture (NA) of the lens ($\lambda/2NA$). Since the resolution limit of an objective lens is largely defined by the imaging light wavelength and the numerical aperture of the lens, there are two general strategies for improving the resolution of the microscope: reducing the imaging light wavelength and increasing the numerical aperture of the lens. In lithography applications, the illumination light wavelength has been pushed toward deep and extreme ultraviolet (DUV and EUV) regimes over recent years to produce smaller features on electronic chips.[2] Nowadays, it is a common practice to work at a wavelength of 193 nm (illuminated through special mask) to produce 20 nm nodes,[3] and even the production of 7 nm nodes will be soon possible with an EUV laser operating at a wavelength of 13.5 nm.[2,4,5] Water or oil immersion objectives are normally used to increase the numerical aperture of a lens up to 1.57.[6] Although in lithography the resolution is as small as about 10 nm, EUV light is not suitable for many other applications since the photon at EUV regime has such a high energy that it can damage most type of samples. However, particularly biological samples typically need to be observed in the visible spectral range, and for this range, the Abbe limit for the classical light microscopy is still about 200 nm. This might sound discouraging, but if one looks at the derivation assumptions from which the Abbe limit was formulated and derived, there are hints to overcome this fundamental limit. The so-called Abbe formula makes several assumptions during derivation,[1,7] and by violating one or several of these assumptions, one can go beyond what limits the classical microscope. For example, the Abbe formula considers the illuminating light to be unpolarized and uniform in intensity distribution, and these assumptions can be violated by using

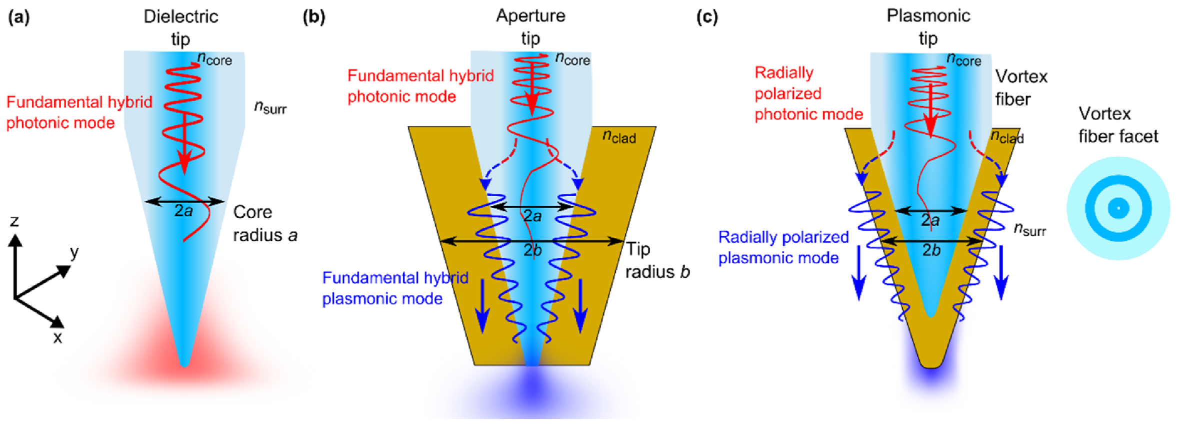

Figure 1. Schematic illustrations of fiber based SNOM tips: **(a)** the dielectric tip, **(b)** the aperture tip, and **(a)** the plasmonic tip. Dielectric tips are tapered optical fibers where the main mode is the fundamental hybrid photonic mode that is illustrated with red. The mode property is largely influenced by the core radius a, and core and surrounding medium refractive indices n_{core} and n_{surr}, respectively. Meanwhile, aperture tips are tapered and metal coated fiber tips where small apertures are made at the apex. The fundamental hybrid photonic mode (illustrated with red) is coupled into the fiber tip that later excites the fundamental hybrid plasmonic mode (illustrated with blue) before experiencing cutoff. The plasmonic mode reaches the aperture and thus governs the near-field interaction outside the tip aperture. The tip's behavior is influenced by the core and the tip radiuses (a and b, respectively) and the core and the cladding refractive indices (n_{core} and n_{clad}, respectively). Plasmonic tips are tapered and fully metal-coated vortex fiber tips where the radially polarized photonic (illustrated with red) and plasmonic (illustrated with blue) modes play the main role.

polarized and patterned light. In fact, the focus spot size of a radially polarized doughnut beam is about 16% smaller than that of a linearly polarized Gaussian beam.[8,9] Since the Abbe formula also considers a linear emission and excitation process, one can think of a non-linear excitation and emission schemes. In stimulated emission depletion (STED)[10] microscopy, the sample marked with fluorescent molecules is excited by a normal Gaussian beam, and the molecules in the outer region are depleted and turned off by the subsequent doughnut shaped pulse. Such scheme can give a resolution well below 50 nm in the visible range since the resolution ($\sim 1/\sqrt{N}$) depends on the total number of photons (N) collected from one particular fluorescent molecule.[10–13] One can also turn on and off the fluorescent molecules with subsequent pulses whilst tracking the center of the excited fluorescent molecules in space and time to achieve 20 nm resolution as it is done in photoactivated localization microscopy (PALM)[14] or in stochastic optical reconstruction microscopy (STORM).[15] These super-resolution microscopy methods offer far-field access to the sample and image it with high contrast and good resolution, yet they require the sample to be marked with fluorescent molecules and illuminated with high energy pulses. Thus, they also cannot be the universal imaging tools to study living cells (due to the phototoxicity and toxicity from organic fluorophores), nano-particles, or other plasmonic effects. The key to improve the imaging resolution and capture the finer details of an image is to include the higher spatial frequencies of emitted light from the sample in the imaging process. Structured illumination microscopy (SIM) also offers superresolution by expanding the collectable spatial frequencies to higher frequencies with the Moiré effect.[16,17] However, no matter how much the collectable spatial frequencies are increased, both the objective lens and the propagation of light to the objective lens act as a low pass filter. There always will be the propagating and non-propagating evanescent waves with higher spatial frequencies that cannot be captured even with SIM. The direct and surest way to tackle this problem is to measure the light in the near-field before any propagation to occur instead of imaging in the far-field.

Various types of scanning probe microscopy (SPM) techniques have been developed over the years to push the capability of microscope imaging down to an atomic and molecular level.[18–28] In SPM, a sharp tip/probe is raster scanned over a sample surface to form an image pixel-by-pixel where the resolution of the image is largely defined by the size of the tip apex. The height information of the sample is obtained at each pixel by measuring and tracking the interaction force between the tip and the sample surface. There are different techniques to measure the interaction force and to control the tip-sample distance. In atomic force microscopy (AFM), a sharp tip is attached to a cantilever, and a laser beam is shined onto the cantilever back surface and deflected back to a quadrant detector to measure the magnitude of cantilever bending due o the force acting between the tip and the sample.[19,25–27] In so called tapping mode operation, a cantilevered tip is connected to a piezo-electric element and is electrically driven at its resonance frequency that makes the tip oscillate perpendicular to the sample surface. Piezo-electric tuning forks are also used in SPMs especially with fiber based tips (see **Figure 1**).[29–32] The fiber based tip is glued onto one of the prongs, and the tuning fork is driven at its resonance frequencies. The tuning fork oscillates the tip parallel to the sample surface in so called shear-force mode.[29–32] Upon approach of the tip to the sample surface, the oscillation amplitude reduces, the phase shifts, and also the resonance frequency slightly shifts in both tapping and the shear-force modes. By tracking either the amplitude or the phase change while the tip approaches the sample surface, one can bring the tip in contact with the surface or at a distance of about 50 nm or below.

The SPM technique can be accompanied with an optical detection mechanism either by collecting the scattered light by the tip apex or directly collecting the field at the sample surface through the fiber based tip at each point of the scanning plane. Such technique is called scanning near-field optical microscopy (SNOM). While the topographic resolution of some SPM techniques, such as AFM, scanning tunneling microscopy (STM), and magnetic force microscopy (MFM), have already reached an atomic resolution,[28] the optical and topographic resolution of SNOM is not quite there yet. Depending on the size and shape of the SNOM tip and the detection and illumination method, the quality of the measurement (resolution, signal to noise ratio, contrast, etc.) varies greatly. The earliest SNOM technique used fiber based aperture tips (see **Figure 1b**) that were tapered and metal coated fiber tips with small apertures at the front for light in- and out-coupling.[20–22] The near-field of the sample can be directly coupled into the aperture then guided through the fiber and detected at the other end of the fiber. The aperture size determines the optical resolution; the smaller is the aperture, the better is the optical resolution. However, with decreasing aperture size, the transmission and collection efficiencies reduce resulting in poor signal to noise ratio (SNR) in optical measurements. Depending on the coating metal, the taper angle, and the operating wavelength, typical transmission efficiencies are about $10^{-7}\%$ or lower for tips with aperture sizes of about 100 nm.[33] Despite these adversities, single fluorescent molecules have been successfully studied with aperture tips.[22–24] The aperture size can be made as small as few tens of nanometers, but the tip size will be always as large as 200 – 300 nm since the coating thickness is about 100 nm to prevent in-coupling of stray slight. This means that the topographic resolution is about 200 – 300 nm in SNOM measurements with aperture tips. A better alternative that can guarantee good resolution in both optical and topographic measurements is a scattering SNOM (s-SNOM). The s-SNOM method uses apertureless AFM cantilever tips with an apex size of about 20 nm to scatter the near-field of the sample and detect it in the far-field.[25–27] When illuminated with a focused beam, the tip apex acts as an antenna and mediates between the far-field illumination and the sample under study. Since the tip apex is as small as about 10 – 20 nm, both the optical and topographic resolution is about 20 nm.[34–36] Since the tip apex is illuminated from far-field either by a parabolic mirror or an objective lens, the majority of the reflected light comes from the sample surface and the tip shaft and not from the tip apex. Thus, s-SNOM requires other techniques to suppress this background light and increase the SNR in the optical measured images. Common techniques are lock-in detection,[37–39] cross polarization technique,[40] homodyne, heterodyne,[27,41,42] or pseudoheterodyne.[43] Despite these complicated techniques, the SNR and optical resolution of s-SNOM measurements degrades with decreasing illumination wavelength which is the typical reason why s-SNOM is mostly used in infrared regime.[44–47]

Both of these two types of SNOM tips, aperture and apertureless, have their pros and cons. The aperture SNOM tip measurements offer great flexibility in measurements, versatile illumination and collection possibilities, and good background suppression. However, the topographic and optical resolution are not as good as that of the s-SNOM measurements and the transmission efficiency of the tip needs to be improved. Meanwhile, the apertureless AFM tip based s-SNOM produces good images with high topographic and optical resolutions, but there is still the problem of far-field detection, low SNR, and complicated techniques to suppress the background scattered light. Furthermore, only a tiny fraction of the illuminated light contributes to the real near-field imaging so that the far- to near-field conversion efficiency is as bad as or even worse than the aperture SNOM tip. By combining advantageous features of both of these two SNOM tips, one can create a new super-performing tip. The best case scenario would be making the tip out of fiber so that the simplicity and versatility of fiber SNOM measurements is inherited and yet adapting the tip shape and size of AFM tips.

It would also be advantageous to incorporate plasmonics in creating a new type of SNOM tip since plasmonic fields, the so called plasmon polaritons which are composed of electromagnetic fields coupled with free electron oscillations at a metal surface, can be confined to a subwavelength structure without limitation in its geometrical size.[48,49] Plasmonic nanoantennas, a spherical gold particle or a gold nano-rod, have been attached to the apexes of fiber based SNOM tips to enhance field localization and detection ability.[50–52] Instead of a conventional circular aperture, a bow-tie metal antenna has been fabricated on the aperture plane of the aperture SNOM tip to enhance the tip's transmission effiency.[53,54] Assisted with plasmonic nano-antennas, these tips have been successfully used in measuring fluorescence of a single molecule proving the benefit of incorporating plasmonics in SNOM.[50–54] In addition to localized plasmons bound to nano-antennas, one can also use propagating surface plasmon polaritons (SPPs) that are surface waves existing at the dielectric-metallic interface.[55,56] These electromagnetic fields coupled with free electron oscillations at a metal surface are confined transversally at the dielectric-metallic interface where the full-width half maxima (FWHM) is about 200 nm.[56] If SPPs are symmetrically excited on a metallic conical structure, there occurs a very peculiar phenomenon. Suppose a radially polarized plasmonic mode (has symmetric radial electric fields) is excited on a metallic conical structure, and it is propagating toward the sharp apex. During the propagation, two important changes happen to the radially polarized plasmonic mode. First, the effective index of the mode increases with decreasing tip radius so the mode's effective wavelength shrinks toward the apex so the mode becomes confined longitudinally along the tip axis in addition to the natural transverse confinement. Second, while the mode propagates toward the tip apex, the mode field amplitude increases with decreasing tip radius due to the decreasing transverse dimension of the structure and the in-phase electron oscillation at the metal surface. Hence, as the radially polarized plasmonic mode propagates toward the tip apex, the electromagnetic field becomes more and more confined both transversally and longitudinally while increasing in field amplitude strength. This phenomenon is called plasmonic superfocusing effect,[57–59] and the radially polarized plasmonic mode on a conical metallic structure is called a superfocusing mode. There have been many attempts in producing tips that employ this plasmonic superfocusing effect, where different methods were used to excite the symmetric radially polarized plasmonic mode on a metallic (mostly gold) conical structure. The most successful type of method was engraving gratings on a shaft of a solid gold tip about 20 μm away from the tip apex.[60–62] When the grating is illuminated from a far-field, SPPs are excited on the tip shaft and propagate toward the tip apex. In this case, the far- to near-field conversion efficiency is improved up to 0.1–1%, which is better than the s-SNOM case.[60] The greatest advantage of this method over the conventional s-SNOM method is, however, the background suppression. Since the tip apex is not directly illuminated, the excitation and detection spots are separated thus reducing the influence of the far-field illumination. In addition, carefully designed photonic crystal structures have been fabricated on a cantilever platform of a cantilevered tip to excite the radially polarized plasmonic mode on a solid silver tip.[63] Aluminum coated and cantilevered dielectric tips also have been employed where the plasmonic mode is excited by far-field illumination.[64] These experimental studies demonstrated that when the tip structure is properly designed, and the radially polarized plasmonic mode is employed, the plasmonic superfocusing effect can enhance SNOM performance greatly.[60,61,65] However, we still prefer the versatility and simplicity of the fiber based SNOM tips so it is worth exploring a way to incorporate the superfocusing effect in fiber based SNOM tips.

Theoretical studies showed that such super-performing tips can be made by tapering and fully metal coating an optical fiber where the superfocusing plasmonic mode can be resonantly excited by a radially polarized fiber mode.[66–71] Hereafter, we refer to the tapered and fully metal coated fiber tips as plasmonic tips (see **Figure 1c**). To produce the plasmonic tip, we use vortex fibers that have double ring cores and are especially designed for guiding the radially polarized fiber mode over a long distance with high modal purity.[72–74] When the radially polarized fiber mode is excited in the vortex fiber, it propagates in the tapered region where the propagation constant of the fiber mode decreases with the shrinking core radius. At a certain tip radius, the longitudinal wavevector components become equal for both of the radially polarized fiber mode in the fiber core and the plasmonic mode at the outer metallic surface. Due to this phase matching and the similar symmetric field distribution, the radially polarized fiber mode can resonantly excite the radially polarized plasmonic mode at the outer metallic surface (at outer interface between metal cladding-surrounding medium). When the resonantly excited radially polarized plasmonic mode reaches the tip apex, it is localized creating a hot spot at the tip apex owing to the superfocusing effect.[57–59] On top of inheriting the best qualities of the aperture SNOM tips, versatility and simplicity in measurements, and of the apertureless SNOM tips, good optical and topographic resolution, the plasmonic tip employs the plasmonic superfocusing effect in its functionality. These features make the fiber based plasmonic tip a very promising new technique for SNOM.

A fully functioning fiber based plasmonic tip is not yet realized let alone demonstrated in near-field SNOM measurements. In light of recent developments of vortex fibers,[72–74] we are able to produce fiber based plasmonic tips and study their detection and excitation characteristics in the near- and far-fields. The aim of the current work is to realize fiber based plasmonic tips and study analytically and experimentally their detection and excitation characteristics in the near- and far-fields.

The current work is structured as follows. We will start with modal analysis of the fiber based SNOM tips to understand their functionality and behavior in the near-field excitation and detection scheme in Chapter 2. This section will help us to compare the performances of different fiber based SNOM tips and most importantly highlight the advantages of plasmonic tips. In Section 2.1, we will introduce the fiber based SNOM tips and discuss briefly about their properties and working mechanism so that we can choose the right mode for modal analysis. In Section 2.2, a quasi-linearly polarized modal analysis is formulated in a general form to express the modes in cylindrical waveguides that can be either dielectric, aperture, or plasmonic tips depending on the chosen core and cladding refractive indices. Due to the tapering and the metal cladding, the linearly polarized (LP) mode approximation, which is commonly used to express linearly polarized degenerate modes in optical fibers, cannot be used to decouple the hybrid modes into two degenerate orthonormal basis. Thus, we use the quasi-linearly polarized mode formalism where the quasi-linearly polarized modes in tapered waveguides are analogous to the LP modes in weakly guiding waveguides. By analyzing the field distributions and amplitude evolution through the tapered region of the tips, it is possible to understand the behavior of different fiber based SNOM tips and their detection and excitation characteristics during the near-field measurements. Dielectric, aperture, and plasmonic SNOM tips are analyzed analytically in Sections 2.3, 2.3, and 2.4.6, respectively. In Chapter 3, we study the emission characteristics of the plasmonic tip in the far- and near-fields. First, we explain the procedures to fabricate the plasmonic tip and to excite the radially polarized mode in the vortex fiber of the plasmonic tip in Section 3.1. Then, we study the evolution of the radially polarized modes through the plasmonic tip starting from the fiber mode in the vortex fiber and in the tapered vortex fiber to the plasmonic mode at the tip apex in Section 3.2. Since the superfocusing plasmonic mode is excited at the outer metal-surrounding medium interface, it is highly sensitive to the surrounding medium's refractive index change. We investigate the influence of the surrounding medium on the tip emission behavior by immersing the plasmonic tip in different liquids while probing the tip emission with a microscope objective in Section 3.3. The plasmonic tip is also used to excite SPPs on a planar gold surface. By scattering these excited planar SPPs with an annular gratings, we study the apex near-field of the plasmonic tip in Section 3.4 . We study the plasmonic tip's detection behavior in Chapter 4. To eliminate the interaction between the tip and the sample and its influence on the detected near-field, we first scan over a tightly focused beam to explore the detection characteristics of the plasmonic tip in Section 4.1. After understanding the detection characteristics depending on the tip apex size and shape, we explore fluorescent beads with the plasmonic tip and perform SNOM measurements in Section 4.2 . Finally, we wrap up the current work with conclusion and outlook in Chapter 5.

2 Modal analysis of fiber based SNOM tips

In this chapter, we study analytically the modes in different fiber based scanning near-field optical microscope (SNOM) tips and their properties. In Section 2.1 , we introduce different types of fiber based SNOM tips, and these are the dielectric fiber tips, aperture tips, and plasmonic tips. We will discuss these tips' properties and the main modes that influence each tip's behavior in the far- and near-fields. Only these main modes will be considered in Sections 2.3 – 2.5 that discuss in detail dielectric fiber tips, aperture tips, and plasmonic tips, respectively. The other supported higher order modes in these tips will not be discussed since in practice, their excitation is intentionally avoided at the fiber end of the tips for example, by using single mode fiber for dielectric and aperture tips. In Section 2.2 , we establish the general analytical description of modes in cylindrical waveguides without restrictions on the cladding and core materials. By appropriately choosing the core and cladding materials, the general expression can be used for different fiber tips. After this analytical establishment, we analyze the simplest of fiber SNOM tips, that is the dielectric tapered fiber tip and discuss it in Section 2.3 . In Section 0, we examine the main mode of interest that is the fundamental quasi linearly-polarized hybrid mode in the dielectric fiber tip in a dielectric surrounding medium. In Section 2.4 , we discuss the aperture tip that is a tapered and metal coated fiber tip with a small aperture at the apex for light in- and out- coupling. We particularly focus on the fundamental quasi linearly-polarized hybrid plasmonic mode at the inner metallic interface and the fundamental quasi linearly-polarized photonic mode in the fiber core. We analyze these modes and their dispersion relations in Section 2.4.1. Plasmonic and photonic modes and their transformations through the tapered metal coated waveguide (aperture tip) are studied in detail in sections 2.4.2 and 2.4.3. It is commonly believed that the evanescent tail of the fundamental photonic mode participates in the near-field interaction outside the tip aperture and determines the detection and excitation characteristics of aperture tips. We will question this matter in Section 2.4.5 by comparing these modes' characteristics with the previously reported experimental studies in the literature.[22,75,76] Meanwhile, Section 2.4.4 concerns the coupling between these two modes. Last but not least, in Section 2.5 , we talk about the plasmonic tip that is a tapered and fully metal-coated fiber tip. In Section 2.5.1, we study the conical surface plasmonic (Co-SP) modes at the interface between the outer metallic surface and the surrounding medium. As we will show in Section 2.5.1, only the fundamental radially polarized conical plasmonic mode can reach the tip apex and be confined in the subwavelength apex. Meanwhile, other higher order modes experience cutoff and thus radiate to the far-field before reaching the tip apex. To excite the fundamental Co-SP mode, we employ the radially polarized fiber mode within the tapered fiber core that offers both non-orthogonality and phase-matching with the fundamental plasmonic mode. This resonant excitation process is discussed in Section 2.5.2. The resonant excitation efficiency is determined by the plasmonic tip structure and its constituents such as a metal coating material, a coating thickness, a surrounding medium refractive index, and a core refractive index. The tips can be fabricated easily with different coating thicknesses so we study the coupling efficiency depending on the coating thickness in Section 2.5.3. The surrounding medium also can be altered easily to influence the behavior of the Co-SP modes on the outer surface of the plasmonic tip and the excitation efficiency. We analyze the excitation efficiency of the fundamental Co-SP mode in different surrounding media in Section 2.5.4.

2.1 Fiber based SNOM tips

Before analytically describing the modes in fiber based SNOM tips, we want to give an overview on fiber based SNOM tips. This section will allow us to anticipate the behavior of each type of SNOM tips and choose the right modes that can exist and participate in the near-field detection and excitation processes for each tip. **Figure 1** illustrates the three main fiber based SNOM tips that are the dielectric tip, the aperture tip, and the plasmonic tip. As shown in **Figure 1a**, a tapered optical fiber is called a dielectric tip, and it is the most basic form of a fiber based SNOM tip. Made of a single mode fiber that is tapered either by chemical etching[77–79] or by heating and pulling techniques,[80,81] the dielectric tip has the smallest apex size, about 30 nm,[82] among the fiber based SNOM tips and thus offers the best topographic resolution of all fiber based tips. Here, when it is said a single mode fiber, keep in mind that the fiber's core radius and the refractive index vary depending on the operation vacuum wavelength. The mode of choice and its propagation in the dielectric tip are also rather simple and straight forward. The Gaussian free-space beam is coupled into the fiber where it excites the fundamental Gaussian-like hybrid mode of the fiber. As the mode propagates toward the tip apex through the tapered dielectric fiber, its effective index decreases, and the mode's tail extends into the air with the decreasing core radius of the fiber. Thus, the mode starts to leak into the surrounding medium as it propagates toward the apex as it is illustrated in **Figure 1a**. When the dielectric tip is used as a local light source, the illumination spot will be non-local covering a broad range of area that is about an order of magnitude larger than the tip size. Besides this poor field confinement at the tip apex, light can couple into the tip not only through the tip apex but also different parts of the tip since there is no metal layer forbidding such coupling possibilities. Furthermore, near the tip apex, any imperfection and dust on the tip shaft can enable coupling between the guided mode within the tip and incident light on the tip shaft since the guided mode's tail stretches into the surrounding medium. This means that when the dielectric tip is used as a detector, the tip can collect both near- and far-fields over a large area. Consequently, the dielectric tip suffers from poor optical resolution.

Figure 1b illustrates the aperture tip that is a tapered and metal coated fiber where a small aperture is made at the apex for in- and out-coupling of light. As the idea was first suggested by E. H. Synge,[83] the electromagnetic field is transmitted through a small aperture with a diameter of 50 – 200 nm that is surrounded by metal. Since the optical resolution of such aperture is defined by the aperture size,[84,85] this configuration offers subwavelength optical resolution. For manufacturing the aperture tip, the tapered dielectric fiber tip (in **Figure 1a**) is often metal-coated with a physical vapor deposition method[86] where a small aperture is made with a Focused Ion Beam (FIB). Common choices for the metal coating are aluminum and gold, but in principal, one can use any other metal that is available. The metal coating thickness is often about 150 nm or more to prevent light leakage through the metal layer. Due to this thick metal coating around the tip aperture, the total size or the diameter of the tip is about 300 nm or more so the topographic resolution (smallest lateral feature size measured by a tip) is at best about 300 nm. Thus, the aperture tip is not the tip of choice for the best topographic resolution. As for the fiber, one can use either single mode or multimode fibers depending on the tip's role in the experiment. Aperture SNOM tips made from single mode fibers offer a predictable optical emission pattern with a better polarizability.[75] Thus, they are better suited for use as local light sources. Meanwhile, aperture tips made from multimode fibers, though they give an unpredictable emission pattern in the near-field, have higher light throughput efficiency for both in- and out-coupling. Consequently, they are better suited for use as local detectors. The fundamental hybrid photonic mode is always excited at the fiber end of the aperture tip that is made of a single mode fiber. This mode is expected to go through a transformation in the tapered region of the tip and to excite the fundamental hybrid plasmonic mode at the fiber core-metal cladding interface as illustrated in **Figure 1b**.[76] We will discuss these aspects in detail in Section 2.4.

The plasmonic tip is a tapered and fully metal-coated fiber tip that is illustrated in **Figure 1c**. As the name suggests, the power conversion between the near-field and the far-field is mediated by the radially polarized plasmonic mode at the surrounding medium-metal coating interface. This radially polarized plasmonic mode plays the fundamental and essential role in the plasmonic tip's function. Depending on the application, the plasmonic tip can be made of different fibers. When the tip is used as a local light source, the plasmonic tip is made of a vortex fiber[74] that has double ring cores (see **Figure 1c**) for safely guiding the doughnut shaped radially polarized photonic mode over a long distance. When the in-coupled radially polarized photonic mode into the vortex fiber reaches the tapered region of the plasmonic tip, it excites the radially polarized plasmonic mode on the outer metallic layer of the tip at a certain tip radius. The excited plasmonic mode then propagates toward the tip apex and creates a localized strong field at the tip apex that can be used as a local light source. Meanwhile, one can use multimode fibers for manufacturing the plasmonic tip when it is employed as a local detector. When the plasmonic tip is raster scanned over a sample surface for light detection in collection mode, the local near-field of a sample will excite a longitudinal field at the apex of the plasmonic tip. The longitudinal field becomes a source of the radially polarized plasmonic mode that will propagate away from the apex and excite a photonic mode inside the tapered fiber.[69] Consequently, one can detect the light at the other end of the fiber tip. With regards to the metal coating, gold or silver is preferred in the visible range, because they have smaller losses compared with other metals such as aluminum or tungsten (which are better suited for UV range). The coating thickness can be 50 – 100 nm depending on the purpose: too thin and light will leak into or out of the tip, too thick and the light throughput efficiency drops significantly with the increasing coating thickness. For a 100 nm of coating thickness, the typical apex size of the plasmonic tip is about 250 nm when a physical vapor deposition method is used for coating the tip. An additional sharpening method is required to achieve a smaller tip apex and improve both the optical and topographic resolution in SNOM applications.

The plasmonic tip's structure and working principal offer not only a greater power conversion efficiency but also huge improvements in both optical and topographic resolution compared with the dielectric and the aperture tip. Since the plasmonic tip is fully covered with a metal coating layer, one can achieve an apex size that is as small as that of the dielectric fiber tip (~ 30 nm) either by sharpening with a FIB or by dry etching with Ar^+ ions. Furthermore, light can be confined onto the plasmonic tip apex where the spot size is only limited by its geometrical dimension.[87] Consequently, the plasmonic tip has the ultimate potential to have the best topographic resolution by having a small apex size and optical resolution by confining light onto this small apex.[57–59,66] The properties of the plasmonic tip are amendments to the previously mentioned two types of tips and thus can bring the performance of the fiber based SNOM to a whole new level that can be even better than the atomic force microscope (AFM) tip based scattering SNOM. We will discuss the plasmonic tip in detail in Section 2.4.5.

2.2 General analytical description of modes in cylindrical waveguides

We establish here the analytical basis of the guided modes in a cylindrical waveguide with arbitrary core and cladding media. The equations derived in this sections are adapted from "Light Transmission Optics" 2nd ed. by Dietrich Marcuse[88] and "Fundamentals of Optical Waveguides" 2nd ed. by Katsunari Okamoto.[89] We derive the equations in a cylindrical coordinate system that is defined by a radial coordinate ρ, an azimuthal coordinate φ, and a propagation coordinate z. Maxwell's equations in frequency domain allow us to express ρ and φ field components (electric and magnetic complex fields) with z components (E_z and H_z) as[88]

$$E_\rho = \frac{-i}{\zeta^2}\left[\beta\frac{\partial E_z}{\partial\rho} + \frac{\omega\mu_0}{\rho}\frac{\partial H_z}{\partial\varphi}\right], \tag{1a}$$

$$E_\varphi = \frac{-i}{\zeta^2}\left[\frac{\beta}{\rho}\frac{\partial E_z}{\partial\varphi} - \omega\mu_0\frac{\partial H_z}{\partial\rho}\right], \tag{1b}$$

$$H_\rho = \frac{-i}{\zeta^2}\left[\beta\frac{\partial H_z}{\partial\rho} - \frac{\omega\varepsilon_0\varepsilon_l}{\rho}\frac{\partial E_z}{\partial\varphi}\right], \tag{1c}$$

and

$$H_\varphi = \frac{-i}{\zeta^2}\left[\frac{\beta}{\rho}\frac{\partial H_z}{\partial\varphi} + \omega\varepsilon_0\varepsilon_l\frac{\partial E_z}{\partial\rho}\right]. \tag{1d}$$

Here, ω is the angular frequency, μ_0 is the vacuum permeability, ε_0 is the vacuum permittivity, and $\varepsilon_l = n_l^2$ is the dielectric constants of a medium l where n_l is the refractive index. We consider the media to be linear, isotropic, and dispersive so the permittivity is given as $\varepsilon_l(\omega) = n_l^2(\omega)$ where ω is the angular frequency of the operating laser. In the experiment, we operate with a continuous wave laser where the laser operating wavelength in vacuum is often used instead of the angular frequency. Henceforth, the laser operating wavelength in vacuum will be given. Furthermore, β is the propagation constant or the wavevector along z-axis, and ζ is the transverse wavevector. With Equation (1) and Maxwell's equations, one can derive the wave equation as

$$\frac{\partial^2 F}{\partial\rho^2} + \frac{1}{\rho}\frac{\partial F}{\partial\rho} + \frac{1}{\rho^2}\frac{\partial^2 F}{\partial\varphi^2} + \zeta^2 F = 0, \tag{2}$$

where F is either E_z or H_z fields. With an ansatz $F = \bar{A}\bar{F}(r)\exp[i(\nu\varphi + \psi - \omega t + \beta z)]$ where $\bar{A}, \nu, \omega,$ and ψ are constants, and t is a time variable; we can deduce above equation to

$$\frac{\partial^2 \bar{F}}{\partial \rho^2} + \frac{1}{\rho}\frac{\partial \bar{F}}{\partial \rho} + \left(\zeta^2 - \frac{\nu^2}{\rho^2}\right)\bar{F} = 0. \tag{3}$$

Physical meanings of the constants are: $\bar{A}$ is the field amplitude, ν is an azimuthal mode number, ω is the angular frequency, and ψ is a phase constant. In later calculations, we consider a steady state case and thus drop the term with $\exp(i(\beta z - \omega t))$ for simplicity. It can be added any time later.

Equation (3) is the differential equation for Bessel functions. To have a converging physical solution in the core, we choose Bessel function of the 1st kind ($\mathrm{J}_\nu(r)$). For the cladding, we choose Hankel function of the 1st kind ($\mathrm{H}_\nu^{(1)}(r)$). Once appropriate functions are chosen, we get a general ansatz in the core as

$$E_z = A\mathrm{J}_\nu(\zeta\rho)\exp(i\nu\varphi + i\psi), \tag{4a}$$

and

$$H_z = B\mathrm{J}_\nu(\zeta\rho)\exp(i\nu\varphi + i\psi), \tag{4b}$$

where A and B are field amplitudes, $\zeta = \sqrt{k_0^2\varepsilon_1 - \beta^2}$ is the transverse wavevector with the core dielectric constant of ε_1, and $k_0 = 2\pi/\lambda_0$ is the wavenumber with the free-space wavelength of λ_0. In the cladding, we substitute $\zeta = i\gamma$ in Equation (3) and obtain the fields as

$$E_z = C\mathrm{H}_\nu^{(1)}(i\gamma\rho)\exp(i\nu\varphi + i\psi)\ , \tag{5a}$$

and

$$H_z = D\mathrm{H}_\nu^{(1)}(i\gamma\rho)\exp(i\nu\varphi + i\psi), \tag{5b}$$

where C and D are field amplitudes, and $\gamma = \sqrt{\beta^2 - k_0^2\varepsilon_2}$ is the transverse wavevector with the cladding dielectric constant of ε_2.

With equations (4) and (5), waveguide modes are solved and classified into hybrid modes that are mostly transverse magnetic (HE) and mostly transverse electric (EH) type of modes, transverse electric (TE) modes, and transverse magnetic (TM) modes. For the dielectric and the aperture tips, the HE mode is of interest since the lowest order mode can be found from this branch by setting the azimuthal mode number to $\nu = 1$ as HE$_{1m}$ where m is the radial mode number. For plasmonic tips, the TM mode is of interest for which the azimuthal mode number is $\nu = 0$ since this branch has a radial electric field component ($E_\rho \neq 0$) and no azimuthal field component ($E_\varphi = 0$).

Before finding the rest of the field components, we would like to modify equations (4) and (5) because in the current state, they do not describe modes properly in the dielectric and the aperture tips. Hybrid modes are mixture of two orthogonally polarized degenerate states, yet the input beam into the fibers of the dielectric and the aperture tips is linearly polarized. Thus, we need to find a proper expression for a mode that can be excited by a linearly polarized input beam and exist in tapered fiber tips or tapered and metal coated fiber tips. Due to the tapering and the metal cladding, there cannot exist purely linearly polarized modes in dielectric or aperture tips; therefore, we cannot use the conventional linearly polarized (LP) mode approximation that are commonly used in optical fibers. To circumvent this issue, we use the quasi-linearly polarized mode formalism as it is the most accurate description of modes in any type of waveguides. The quasi-linearly polarized mode formalism is established by replacing $\exp(i\nu\varphi + i\psi)$, that describes the azimuthal variation of fields with a constant phase of ψ, in equations (4) and (5) with $\cos(\nu\varphi + \psi)$ and $\sin(\nu\varphi + \psi)$. By doing so, we can decompose the hybrid modes into two orthogonal quasi-linearly polarized hybrid modes (for details see Reference 88 and 89). For example, the fundamental hybrid photonic mode of HE_{11} can be decomposed into the quasi x-polarized $\mathrm{HE}_{11}^{\mathrm{x}}$ mode when $\psi = 0$ and the quasi y-polarized $\mathrm{HE}_{11}^{\mathrm{y}}$ mode when $\psi = \frac{\pi}{2}$. The quasi-linearly polarized modes have all 6 vector field components. For the quasi x-polarized mode, the electric field's x-component is the dominant one, and the y-component is for the quasi y-polarized mode.

With the above mentioned modification, we can find ρ and φ components of the electromagnetic field by using equations (1), (4), and (5). Thus, for a waveguide with a radius of ρ_0, the field components in the core ($\rho \leq \rho_0$) are given as

$$E_z = A\mathrm{J}_\nu(\zeta\rho)\cos(\nu\varphi + \psi), \tag{6a}$$

$$H_z = B\mathrm{J}_\nu(\zeta\rho)\sin(\nu\varphi + \psi), \tag{6b}$$

$$E_\rho = \frac{-i}{\zeta^2}\left[\beta\zeta A\mathrm{J}_\nu^{'}(\zeta\rho) + \frac{\omega\mu_0\nu}{\rho}B\mathrm{J}_\nu(\zeta\rho)\right]\cos(\nu\varphi + \psi), \tag{6c}$$

$$E_\varphi = \frac{-i}{\zeta^2}\left[\frac{-\beta\nu}{\rho}A\mathrm{J}_\nu(\zeta\rho) - \omega\mu_0\zeta B\mathrm{J}_\nu^{'}(\zeta\rho)\right]\sin(\nu\varphi + \psi), \tag{6d}$$

$$H_\rho = \frac{-i}{\zeta^2}\left[\frac{\omega\varepsilon_0\varepsilon_1\nu}{\rho}A\mathrm{J}_\nu(\zeta\rho) + \beta\zeta B\mathrm{J}_\nu^{'}(\zeta\rho)\right]\sin(\nu\varphi + \psi), \tag{6e}$$

and

$$H_\varphi = \frac{-i}{\zeta^2}\left[\omega\varepsilon_0\varepsilon_1\zeta A \mathrm{J}_\nu^{'}(\zeta\rho) + \frac{\beta\nu}{\rho} B \mathrm{J}_\nu(\zeta\rho)\right]\cos(\nu\varphi + \psi), \tag{6f}$$

where $\mathrm{J}_\nu^{'}(\zeta\rho) = \partial \mathrm{J}_\nu(\zeta\rho)/\partial(\zeta\rho)$. Here, ρ_0 can be either the core radius a or the tip radius b in **Figure 1**.

In the cladding ($\rho > \rho_0$), the field components are given as

$$E_z = C\mathrm{H}_\nu^{(1)}(i\gamma\rho)\cos(\nu\varphi + \psi), \tag{7a}$$

$$H_z = D\mathrm{H}_\nu^{(1)}(i\gamma\rho)\sin(\nu\varphi + \psi), \tag{7b}$$

$$E_\rho = \frac{i}{\gamma^2}\left[i\beta\gamma C\mathrm{H}_\nu^{(1)'}(i\gamma\rho) + \frac{\omega\mu_0\nu}{\rho} D\mathrm{H}_\nu^{(1)}(i\gamma\rho)\right]\cos(\nu\varphi + \psi), \tag{7c}$$

$$E_\varphi = \frac{i}{\gamma^2}\left[\frac{-\beta\nu}{\rho} C\mathrm{H}_\nu^{(1)}(i\gamma\rho) - i\omega\mu_0\gamma D\mathrm{H}_\nu^{(1)'}(i\gamma\rho)\right]\sin(\nu\varphi + \psi), \tag{7d}$$

$$H_\rho = \frac{i}{\gamma^2}\left[\frac{\omega\varepsilon_0\varepsilon_2\nu}{\rho} C\mathrm{H}_\nu^{(1)}(i\gamma\rho) + i\beta\gamma \mathrm{D}\mathrm{H}_\nu^{(1)'}(i\gamma\rho)\right]\sin(\nu\varphi + \psi), \tag{7e}$$

and

$$H_\varphi = \frac{i}{\gamma^2}\left[i\omega\varepsilon_0\varepsilon_2\gamma C\mathrm{H}_\nu^{(1)'}(i\gamma\rho) + \frac{\beta\nu}{\rho} D\mathrm{H}_\nu^{(1)}(i\gamma\rho)\right]\cos(\nu\varphi + \psi), \tag{7f}$$

where $\mathrm{H}_\nu^{(1)'}(i\gamma\rho) = \partial \mathrm{H}_\nu^{(1)}(i\gamma\rho)/\partial(i\gamma\rho)$.

Meanwhile, to convert from the cylindrical to the Cartesian coordinate systems, we can use the following relations

$$F_x = F_\rho\cos(\varphi) - F_\varphi\sin(\varphi), \tag{8a}$$

and

$$F_y = F_\rho\cos(\varphi) + F_\varphi\sin(\varphi), \tag{8b}$$

where *F* represents either the electric or magnetic fields.

To find the amplitudes B, C, and D, we use the continuity of the transverse fields (E_z, H_z, E_φ, and H_φ) at the core-cladding interface at a core radius of $\rho = \rho_0$ and find them as

$$C = A\frac{\mathrm{J}_\nu(\zeta\rho_0)}{\mathrm{H}_\nu^{(1)}(i\gamma\rho_0)}, \tag{9a}$$

$$D = B\frac{\mathrm{J}_\nu(\zeta\rho_0)}{\mathrm{H}_\nu^{(1)}(i\gamma\rho_0)}, \tag{9b}$$

and

$$B = A\frac{-\beta\nu}{\rho_0\omega\mu_0}\left[\frac{1}{\gamma^2}+\frac{1}{\zeta^2}\right]\left[\frac{\mathrm{J}_\nu'(\zeta\rho_0)}{\zeta\mathrm{J}_\nu(\zeta\rho_0)}-\frac{\mathrm{H}_\nu^{(1)'}(i\gamma\rho_0)}{i\gamma\mathrm{H}_\nu^{(1)}(i\gamma\rho_0)}\right]^{-1}. \tag{9c}$$

The amplitude A can be set as 1 or found by making the total time averaged power to unity that is $P = \iint_{-\infty}^{\infty} 0.5\mathrm{Re}[(\mathbf{E}\times\mathbf{H})\cdot\mathbf{u}_z]dS$ for lossy waveguides and $P = \iint_{-\infty}^{\infty} 0.5\mathrm{Re}[(\mathbf{E}\times\mathbf{H}^*)\cdot\mathbf{u}_z]dS$ for non-lossy waveguides. The continuity of the transverse fields also gives the dispersion relation as

$$\begin{vmatrix} \mathrm{J}_\nu(\zeta\rho_0) & 0 & -\mathrm{H}_\nu^{(1)}(i\gamma\rho_0) & 0 \\ \frac{\beta\nu}{\rho_0\zeta^2}\mathrm{J}_\nu(\zeta\rho_0) & \frac{i\omega\mu_0}{\zeta}\mathrm{J}_\nu'(\zeta\rho_0) & \frac{\beta\nu}{\rho_0\gamma^2}\mathrm{H}_\nu^{(1)}(i\gamma\rho_0) & \frac{-i\omega\mu_0}{\gamma}\mathrm{H}_\nu^{(1)'}(i\gamma\rho_0) \\ 0 & \mathrm{J}_\nu(\zeta\rho_0) & 0 & -\mathrm{H}_\nu^{(1)}(i\gamma\rho_0) \\ \frac{-i\omega\varepsilon_0\varepsilon_1}{\zeta}\mathrm{J}_\nu'(\zeta\rho_0) & \frac{\beta\nu}{\rho_0\zeta^2}B\mathrm{J}_\nu(\zeta\rho_0) & \frac{\omega\varepsilon_0\varepsilon_2}{\gamma}\mathrm{H}_\nu^{(1)'}(i\gamma\rho_0) & \frac{\beta\nu}{\rho_0\gamma^2}\mathrm{H}_\nu^{(1)}(i\gamma\rho_0) \end{vmatrix} = 0. \tag{10}$$

This general dispersion relation can be decomposed into two separate equations that are for HE and EH type of modes. By solving the quadratic equation of (10) for $\frac{\mathrm{J}_\nu(\zeta\rho_0)}{\zeta\rho_0\,\mathrm{J}_\nu'(\zeta\rho_0)}$, we obtain

$$\begin{aligned} &\frac{\mathrm{J}_\nu(\zeta\rho_0)}{\zeta\rho_0\,\mathrm{J}_\nu'(\zeta\rho_0)}-\frac{(\varepsilon_1+\varepsilon_2)}{2\varepsilon_1}\frac{\mathrm{H}_\nu^{(1)'}(i\gamma\rho_0)}{i\gamma\rho_0\mathrm{H}_\nu^{(1)}(i\gamma\rho_0)} \\ &\pm\frac{1}{2\varepsilon_1}\sqrt{\left((\varepsilon_1+\varepsilon_2)\frac{\mathrm{H}_\nu^{(1)'}(i\gamma\rho_0)}{i\gamma\rho_0\mathrm{H}_\nu^{(1)}(i\gamma\rho_0)}\right)^2-4\varepsilon_1\left(\left(\frac{\mathrm{H}_\nu^{(1)'}(i\gamma\rho_0)}{i\gamma\rho_0\mathrm{H}_\nu^{(1)}(i\gamma\rho_0)}\right)^2-\left(\frac{1}{(\rho_0\gamma)^4}-\frac{1}{(\rho_0\zeta)^4}\right)^2(\beta\nu)^2\right)}=0. \end{aligned} \tag{11}$$

The minus and plus signs in front of the square root in Equation (11) give dispersion relations for HE ('–' in front of the square root) and EH ('+' in front of the square root) type of modes, respectively. Furthermore, if we set the azimuthal mode number to $\nu = 0$ in HE ('–' in front of the square root) and EH ('+' in front of the square root) dispersion relation equations, we can find the dispersion relations for TM and TE modes, respectively.

So far, we have obtained all the necessary equations for analyzing the modes in different fiber SNOM tips. Before we start analyzing and discussing different tips and modes within them, we will make some assumptions for simplicity in evaluating the modes and their propagation in the tapered fiber tips that will be discussed in later sections. *First*, we will assume that the waveguide's cladding is infinitely thick so that there are only two media (core and cladding) taken into consideration. This assumption is justified for most fiber SNOM tips. During the tapering process of the optical fiber, either the core or the cladding of the optical fiber vanishes depending on the tapering method. In the heating and pulling method, the fiber core shrinks in size and becomes irrelevant near the apex region. In the chemical etching method, the optical fiber is etched starting from the fiber cladding so only the core remains near the apex region. Thus, when we calculate modes in the dielectric tips, we consider the core as a tapered fiber and the cladding as the surrounding medium. For the aperture and the plasmonic tips, the field's penetration depth in the metal (~ 20 nm at a wavelength of 784 nm) is smaller than the metal layer thickness (> 100 nm). Thus, again the 3rd medium can be overlooked. *Second*, the tapered fiber tip is considered as conjoined cylindrical waveguides with decreasing radiuses and infinitesimal thicknesses. Thus, we can consider modes in each cylindrical structure instead of calculating a mode in a conical structure. *Third*, since the typical taper angle of tapered fiber tips is smaller than 20° (with the heating and pulling method), we assume that the modes propagate adiabatically in the most part except near the mode cutoff radius. The adiabatic propagation of modes ensures that the transition of these local modes from one cylinder to the neighboring cylinder will not give rise to excitation of other higher order modes or back propagating counter parts. With this assumption, we can consider the local modes in each local cylindrical structure as the eigen modes of the tapered fiber tip. An exception occurs only within the last micrometer of the tip because the dispersion curves of modes depending on the core radius bend sharply toward the mode cutoff. This behavior results in high non-adiabaticity in the mode propagation regardless of the small taper angle. Since such a region is short, we can neglect it in most cases and discuss it separately.

The fields at the apex or aperture plane of fiber based SNOM tips can also be studied by doing numerical calculations (finite difference time domain or multiple multipole methods)[66,90,91] or using a dipole approximation (Bethe-Bouwkamp theory).[92–96] As we will show in upcoming sections, the analytical calculations agree well with the numerical calculations. However, unlike our analytical calculations, the numerical calculation is of little help in understanding the mode propagation and its field transformation during the propagation toward the tip apex or aperture.

2.3 Dielectric tips

In this section, we consider the dielectric tapered fiber tip and the fundamental hybrid mode (HE_{11}) that is guided within the tip. We use equations (6), (7), and (11) introduced in Section 2.2 to find the field distributions and the dispersion relations of the fundamental hybrid mode. In these equations, we have transverse wavevectors as $\zeta = \sqrt{\beta^2 - k_0^2\varepsilon_{\mathrm{core}}}$ and $\gamma = \sqrt{k_0^2\varepsilon_{\mathrm{surr}} - \beta^2}$ where the core and cladding dielectric constants are $\varepsilon_1 = \varepsilon_{\mathrm{core}}$ and $\varepsilon_2 = \varepsilon_{\mathrm{surr}}$. To calculate the dispersion relation of HE_{11}, we use Equation (11) with a minus sign in front of the square root. In the calculations, we choose a core refractive index of $n_{\mathrm{core}} = 1.4535$,[97] a surrounding medium refractive index of $n_{\mathrm{surr}} = 1.0$, and a laser vacuum wavelength of $\lambda_0 = 784$ nm. The dielectric tip is expected to have a taper angle no larger

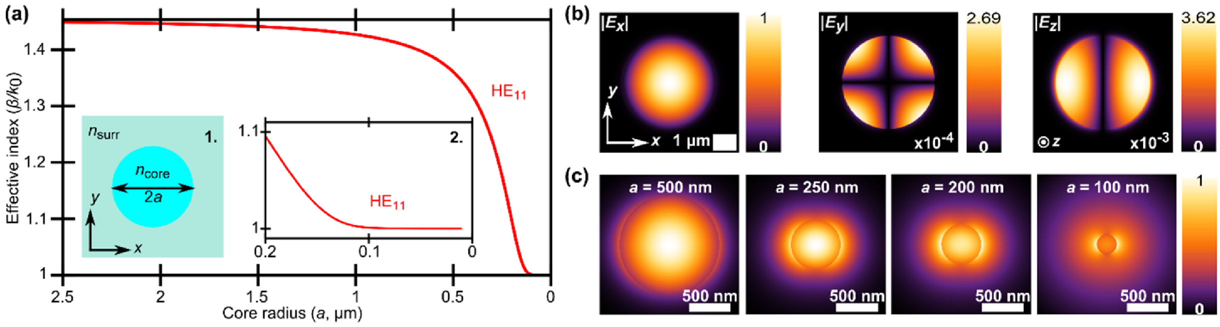

Figure 2. (a) Effective index curve of the fundamental hybrid mode (HE$_{11}$) in the dielectric tip. The dielectric tip structure is illustrated in Inset 1. The effective index curve slowly decreases with the decreasing core radius a, and near the core radius a of 100 nm, it becomes almost 1. The close-up of this region is shown in Inset 2. Having an effective index close to 1 means that the mode is turning into a free space beam. Thus, it is no longer guided in the dielectric core. **(b)** Absolute of the electric field components ($|E_x|$, $|E_y|$, and $|E_z|$) at a core radius a of 2 μm. Here, we consider the quasi x-polarized mode that is noted as HE$^x_{11}$. **(c)** Absolute of the total electric field ($|E_\perp| = \sqrt{|E_x|^2 + |E_y|^2 + |E_z|^2}$) at different core radiuses a: 500 nm, 250 nm, 200 nm, and 100 nm.

than 20° and an apex size/diameter of about 30 nm. In Section 0, we discuss in detail the dispersion relation of the HE$_{11}$ mode and its evolution in the taper during propagation toward the apex.

The fundamental quasi x-polarized hybrid mode in dielectric tips. First, we will discuss the dispersion relation of the fundamental hybrid mode (HE$_{11}$) in the dielectric tip. The effective index curve (β/k_0) of the fundamental hybrid mode is shown in **Figure 2a**. The waveguide structure is illustrated in **Figure 2a** in Inset 1. Since the surrounding medium of the waveguide is considered to be air (n_{surr} = 1.0), and the core is also assumed to be lossless, the imaginary part of the effective index is negligible. There are several aspects we can learn from this dispersion curve. First, we need to observe the rate of change of the effective index. The effective index at a larger core radius a changes smoothly and adiabatically never exceeding the core refractive index (n_{core}). Here, the mode will propagate rather smoothly preserving its properties. Below the core radius a of 600 nm, the effective index depending on the core radius a changes rapidly. This indicates that the mode's propagation is largely non-adiabatic in this region, and there will be coupling to the back-propagating counterpart. Next, we take a close look at Inset 2 in **Figure 2a** which is a close-up of the dispersion relation below the core radius a of 200 nm. The inset shows that the dispersion curve changes from the concave-down curve into a concave-up curve near the core radius a of 150 nm that is called the point of inflection. It is expected that there will be significant changes in the mode and its field components ratios at the point of inflection. Furthermore, Inset 2 also shows that at a core radius a of 100 nm, the effective index of the HE$_{11}$ mode becomes $\beta/k_0 = 1.00103$ and is very close to 1. The closer the mode's effective index is to the cladding refractive index (in this case air), the weaker the mode is guided in the waveguide. The 780HP fiber (Thorlabs) with $n_{\text{core}} = 1.4593$ and $n_{\text{clad}} = 1.4535$ is considered a weakly guiding waveguide[97] as the difference between the mode's effective index and the cladding refractive index ($\beta_{\text{HE11,780HP}}/k_0 - n_{\text{clad}}$) is 0.004. If we compare this number ($\beta_{\text{HE11}}/k_0 - n_{\text{air}} = 0.001$) with that of the dielectric tip, there is 4× difference. This means that at a core radius a of 100 nm, the HE_{11} mode is guided much weaker in the dielectric tip than in the weakly guiding fiber case. The mode will be largely extended into the free space almost like a free space beam. Hence, one can say that the HE_{11} mode will experience cutoff shortly after the core radius a of 100 nm. With the increasing wavelength, this cutoff radius will increase, and the field confinement in the core will reduce. For a typical dielectric tip with an apex size of about 30 nm,[98] the confinement of the electromagnetic fields is expected to be very inefficient and consequently the conversion efficiency or the delivered power from the fiber end to the apex. The majority of the light will escape the tip before reaching the apex and hinder the signal to noise ratio in measurements by acting as a background light.

Next, we take a look at the fundamental, quasi x-polarized, hybrid mode in dielectric tips that is denoted as HE_{11}^{x}. We are especially interested in the evolution of the mode profile and the electric field components ratios during the propagation toward the tip apex. Here, we arbitrary define the x-axis as the input polarization axis. We calculate the absolute of the electric field components ($|E_x|$, $|E_y|$, and $|E_z|$) at a core radius a of 2 µm and present the results in **Figure 2b**. The field components of the HE_{11}^{x} mode resemble that of a focused linearly x-polarized Gaussian beam.[99] This means that for dielectric tips made of single mode fibers, the HE_{11}^{x} mode can be excited by the x-polarized Gaussian beam. Furthermore, the mode is confined within the dielectric tip at a core radius a of 2 µm. This mode profile changes, however, as the core radius a decreases. We calculate the absolute of the total electric field ($|E_\perp| = \sqrt{|E_x|^2 + |E_y|^2 + |E_z|^2}$) at core radiuses a of 500 nm, 250 nm, 200 nm, and 100 nm and present the results in **Figure 2c**. As the figures show, the fields stretch into the surrounding medium with the decreasing core radius a due to the decreasing index difference between the refractive index of the cladding (air) and the mode's effective index. We can see this clearly if we calculate the penetration depth of fields in air that is the radial distance from the core radius a to the point where the field intensity reduces to 1/e (Beer-Lambert Law) of the value at the core radius a.

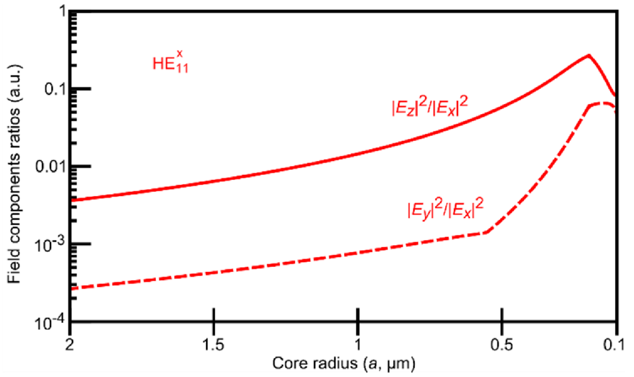

Figure 3. Field components ratios of the HE_{11}^{x} mode depending on the core radius a. $|E_y|^2/|E_x|^2$ is in a dashed red line, and $|E_z|^2/|E_x|^2$ is in a solid red line. We calculate the field components ratios only until a core radius a of 100 nm since below this point the effective index of mode is nearly 1 indicating the mode has turned into a free space beam.

The penetration depth of the fields at a core radius a of 500 nm is 59.54 nm, and it increases to 158.28 nm at a core radius a of 100 nm. At a core radius a of 100 nm, the field strength in the core is weaker than in the cladding. Essentially, the mode is experiencing cutoff at a core radius a of 100 nm so the mode energy is escaping the core.

Lastly, we calculate the field components ratios that are $|E_y|^2/|E_x|^2$ (dashed red line) and $|E_z|^2/|E_x|^2$ (solid red line) and present the results in **Figure 3**. At each core radius a, the maxima of $|E_x|^2$, $|E_y|^2$, and $|E_z|^2$ are found, and the y- and z-components are compared with the x-component which is the dominant one for the HE_{11}^{x} mode at a large core radius a. As the figure shows, the y- and z-components increase in strength compared with the dominant x-component with a decreasing core radius a. This behavior is very similar to the focusing of a free space Gaussian beam by a lens. Here, the increasing numerical aperture (NA) of the lens is analogous to the decreasing core radius a of the dielectric tip. In both cases, however, the y- and z-components never become larger than the x-component as can be seen in **Figure 3**. By the time the ratios reach their maxima near the core radius a of 150 nm (point of inflection in **Figure 2a**), the mode starts to leak into the air turning into a free space beam. Since the mode is no longer guided in the waveguide, the ratios cannot increase further.

2.4 Aperture tips

In this section, we will discuss the aperture tip which is a tapered metal coated fiber tip where a small aperture is made at the tip for in- and out-coupling of light. In aperture tips, there exist photonic modes that are guided in the area of increased index in the fiber core and plasmonic modes that are confined at the fiber core and the metal cladding interface. Among the many possible modes, we will concentrate on the two main modes that are the fundamental hybrid plasmonic and photonic modes since they play essential roles in the aperture tips' functionality. First, we will take a look at the dispersion relations of the fundamental plasmonic and photonic modes in Section 2.4.1. Properties of each mode will then be discussed individually in sections 2.4.2 and 2.4.3. We will discuss the coupling between the fundamental plasmonic and photonic modes in Section 2.4.5. The roles of the fundamental photonic and plasmonic modes in aperture tips are discussed in Section 2.4.4. Lastly, we will discuss the influence of the metal cladding material on aperture tip's functionality in Section 2.4.6. We use the formalism in Section 2.2 to analyze the fundamental hybrid photonic mode in the dielectric core and fundamental hybrid conical surface plasmon (Co-SP) mode at the inner (dielectric core-metal cladding) interface. To determine the dispersion relations of the fundamental plasmonic and photonic modes, we use Equation (11) with a minus sign in front of the square root that describes the HE type of photonic and plasmonic modes. The field components are calculated using equations (6 – 9). In these equations, we have the core and cladding dielectric constants of $\varepsilon_1 = \varepsilon_{\mathrm{core}}$ and $\varepsilon_2(\lambda_0) = \varepsilon_{\mathrm{metal}}(\lambda_0)$, respectively. The transverse wavevectors in the core and the cladding are $\zeta = \sqrt{\beta^2 - k_0^2\varepsilon_{\mathrm{core}}}$ and $\gamma = \sqrt{k_0^2\varepsilon_{\mathrm{metal}} - \beta^2}$. In sections 2.4.1–2.4.5, we will consider gold cladded aperture tips. We designate the plasmonic mode at the inner (dielectric core – metal cladding) interface as νCo-SPin where ν is the azimuthal mode number and "in" refers to the inner interface. This helps us to distinguish them from the plasmonic modes at the outer (metal cladding-dielectric surrounding medium) interface that will be discussed in Section 2.5 . For calculating the modes in aperture tips, we choose a core refractive index of $n_{\mathrm{core}} = 1.4535$,[97] a gold refractive index of $n_{\mathrm{gold}}(\lambda_0) = \sqrt{-20.95 + 1.68i}$,[100] and a laser vacuum wavelength of $\lambda_0 = 784$ nm. The aperture tip is expected to have a typical taper angle of about 20° and an aperture size/diameter of about 100 nm.

2.4.1 Dispersion relations of modes in aperture tips

We consider a dielectric conical structure with a core radius a in an infinitely large metal surrounding medium as illustrated in **Figure 4a** in Inset 1. In this structure, the fundamental photonic and plasmonic modes have the smallest cutoff radius and thus can propagate to a tapered region with the smallest core radius a. We show the calculated effective indices of the fundamental photonic (red lines) and plasmonic (blue lines) modes depending on the core radius a in **Figure 4a** and **b** which are for the real (β'/k_0) and imaginary (β''/k_0) parts, respectively. As it can be seen in the figures, the effective index value decreases slowly and adiabatically above a core radius a of 600 nm so modes are expected to propagate and transform adiabatically in this region. In this region, the imaginary part of the effective index is greater for the plasmonic mode than the photonic mode indicating the propagation loss is large for the plasmonic mode. However, the effective indices start to change rapidly below the core radius a of 600 nm for both modes. This rapid change of the effective index indicates that the modes will propagate non-adiabatically despite the small taper angle. Since the local modes can no longer be approximated as the eigen modes, there can occur a coupling between different modes and their backward propagating counterparts in this region. Inset 2 in **Figure 4a** zooms into the region where the core radius a is smaller than 500 nm. It shows that the dispersion

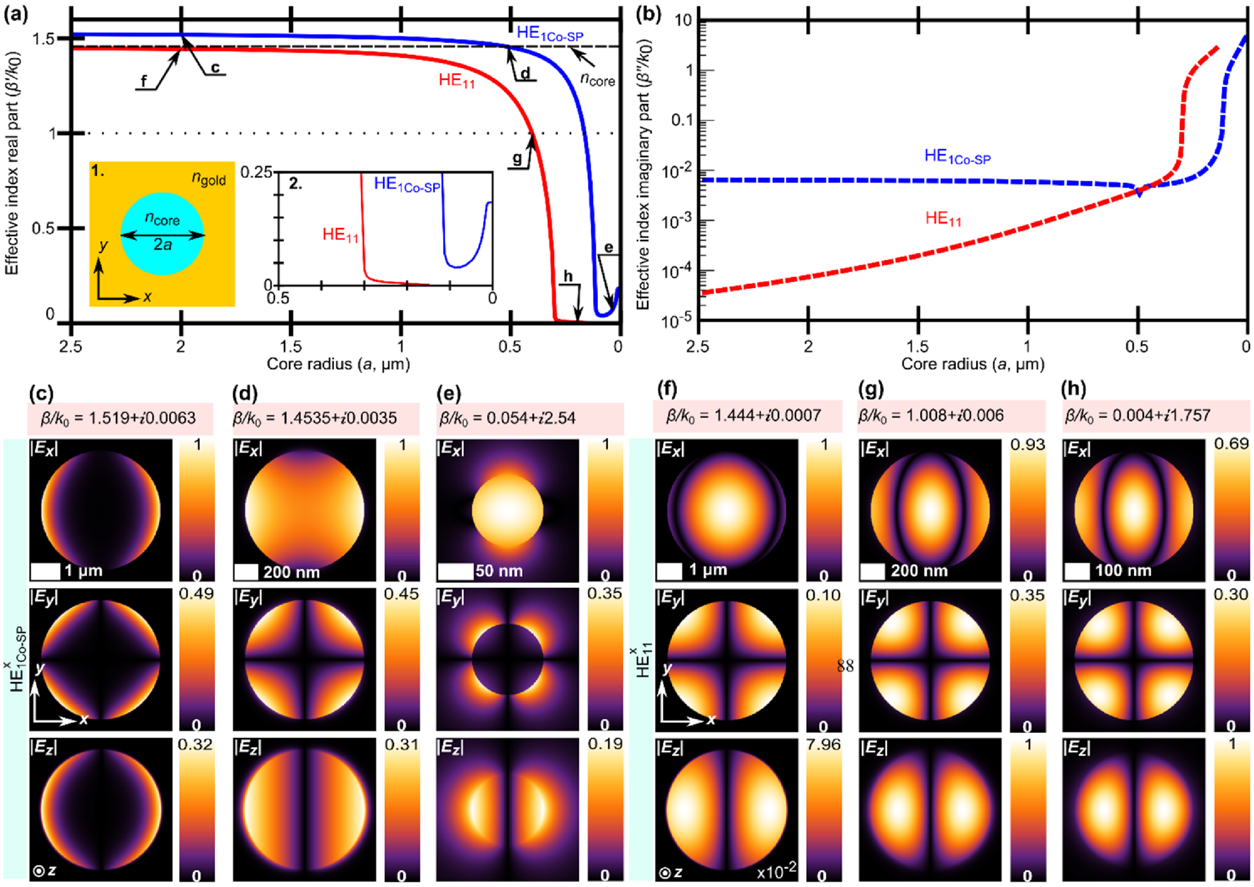

Figure 4. **(a)** Effective index's real part for the fundamental plasmonic ($\mathrm{HE}_{1\mathrm{Co\text{-}SPin}}$, blue curve) and photonic (HE_{11}, red curve) modes depending on the core radius a. Inset 1 illustrates the waveguide structure that has a dielectric core with a radius of a and an infinitely large gold cladding. Meanwhile, Inset 2 shows the close-up of the near cutoff region. **(b)** Effective index's imaginary part for the fundamental plasmonic (blue dashed curve) and photonic (red dashed curve) modes depending on the core radius a. **(c-e)** Absolute of the electric field components ($|E_x|$, $|E_y|$, and $|E_z|$) for the $\mathrm{HE}^x_{1\mathrm{Co-SPin}}$ mode at core radiuses a of (c) 2 μm, (d) 502 nm, and (e) 25 nm. The superscript x denotes that the mode is quasi x-polarized. **(f-h)** Absolute of the electric field components ($|E_x|$, $|E_y|$, and $|E_z|$) for the HE^x_{11} mode at core radiuses a of (f) 2 μm, (g) 405 nm, and (h) 200 nm. Adapted from Reference 76.

curves change from a concave-down to a concave-up type of curve (inflection point) near the core radius a of 300 nm for the photonic mode and 120 nm for the plasmonic mode. As we will show later, this curvature change of the effective index curve indicates a major shift in mode behavior such as the mode profile and its maximum intensity ratios between the different field components. Furthermore, in this region, the photonic mode approaches closer to the mode cutoff and so the imaginary part of the effective index increases. Thus, the propagation loss of the photonic mode becomes larger than the plasmonic mode.

Depending on the real part of the effective index, modes can be distinguished as a guided mode, a leaky mode, or an evanescent mode. This classification differs slightly for the plasmonic and the photonic modes. For the plasmonic mode, we have a bound mode when the effective index's real part is larger than the core refractive index ($\beta'/k_0 \geq n_{\text{core}}$). At a large core radius a say above 2 μm, we can see that the effective index of the plasmonic mode ($\beta/k_0 = 1.519 + 0.0063i$) is converging to a certain value (see **Figure 4a**). This value is indeed closer to the effective index value of the planar SPPs ($\beta_{\text{P-SPP}}/k_0 = 1.5328 + 0.0069i$) at a planar dielectric-gold interface. We can say that at a larger core radius a, the conical plasmonic mode behaves more like surface plasmon polaritons at a flat surface since the fields and electron oscillations from different sides of the cylinder interact weakly. If $\beta'/k_0 < n_{\text{core}}$, the plasmonic mode is a leaky mode. A leaky mode means that the plasmonic mode will gradually stretch into the dielectric core. This boundary between the bound and leaky mode region is marked with a dashed line in **Figure 4a**. When the effective index of the mode becomes 0, a mode should turn into an evanescent mode. As **Figure 4a** shows, this cutoff never occurs for the fundamental plasmonic mode.

Meanwhile, for the photonic modes in an aperture tip, the mode's effective index never gets larger than the core refractive index ($\beta'/k_0 < n_{\text{core}}$) as it is shown in **Figure 4a**. This is an important indicator showing the mode is indeed a photonic mode not a plasmonic one. The photonic mode is a bound mode if the effective index's real part larger than 0 ($\beta'/k_0 \geq 0$). There is no leaky mode region for the photonic modes in aperture tips since the modes cannot leak out due to the thick metal cladding surrounding the dielectric core. By calculating the field components at this point, we show that nothing happens to the fundamental photonic mode when its real part of the effective index becomes 1. If the effective index's real part becomes 0, the photonic mode reaches the cutoff and turns into an evanescent mode. The fundamental photonic mode experiences cutoff at a core radius a of 150 nm for our chosen calculation parameters. Due to the lossy metal cladding, all modes are lossy and the propagation loss increases toward the tip aperture as it can be seen in **Figure 4b**.

2.4.2 Fundamental quasi x-polarized hybrid plasmonic mode in aperture tips

We discuss the properties of the $\mathrm{HE}^{x}_{1\mathrm{Co-SPin}}$ mode that is the fundamental quasi x-polarized hybrid plasmonic mode at the dielectric fiber core and the metal cladding interface. Here, the superscript x denotes the mode is quasi x-polarized. Depending on the effective index value and the core radius a, this mode experiences major changes and possesses slightly different properties in different regions. We calculate the absolute of the electric field components ($|E_x|$, $|E_y|$, and $|E_z|$) at a core radius a of 2 µm, 502 nm, and 25 nm and present them in **Figure 4c-e**. These positions are noted in the dispersion curve of the mode that is illustrated in a blue line in **Figure 4a**.

At a core radius a of 2 µm in **Figure 4c**, the mode is a plasmonic bound mode so the field maxima is concentrated at the core and cladding interface for all electric field components. This is a typical characteristic that is common to all types of surface plasmons. **Figure 4d** illustrates the fundamental plasmonic mode at a core radius a of 502 nm that is the borderline between the bound mode and leaky

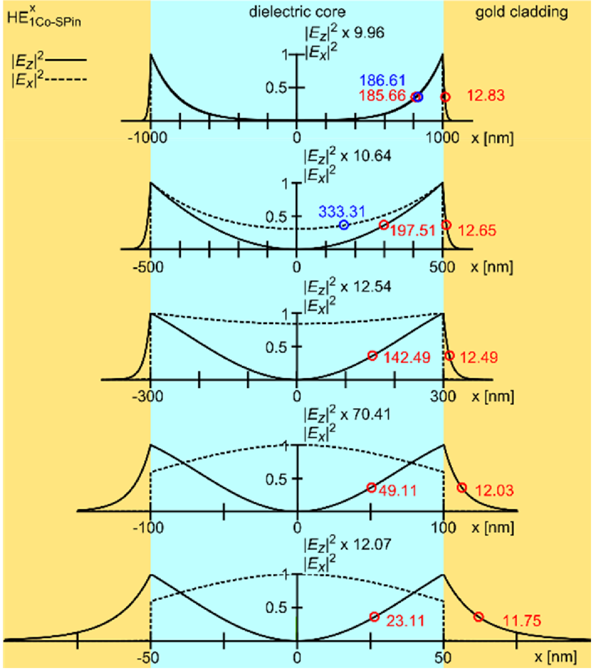

Figure 5. Normalized absolute square of x- and z-components (dashed and solid lines, respectively) along x-axis for the fundamental quasi x-polarized plasmonic mode. The field decay lengths (1/e of the maximum value) are noted with blue and red circles for the electric field's x- and z-components, respectively. For the x-component, the field tails start to overlap. Already at the core radius a of 300 nm, one cannot calculate the decay length in the core since the field maximum is now at the center of the core. Note, that the electric field's x-component is discontinuous along x-axis, but the electric flux is. Adapted from Reference 76.

mode regions. Toward the leaky mode region (small core radius a), fields starts to stretch into the dielectric core that can be clearly seen in the dominant x-component in **Figure 4d**. This change continues to build up as the mode enters deeply into the leaky mode region with the decreasing core radius a. At a core radius a of 25 nm in **Figure 4e**, the maximum field amplitude of the x-component is at the center of the core not at the core-cladding interface as it used to be.

The power concentration shifts from the core-cladding interface to the center of the dielectric core because the penetration depth of field intensity increases in the core for the dominant x-component. We calculate the absolute square of electric field components ($|E_x|^2$ and $|E_z|^2$) along the x-axis at different core radiuses a and present them in **Figure 5**. The penetration depth is calculated in the metal cladding and the dielectric core and noted with red and blue circles for z- and x-components, respectively. The electric field's x-component is plotted in a dashed line while the z-component is in a solid line. As the core radius decreases, the penetration depth of the x-component increases in the dielectric core and starts to overlap resulting in an increase of power at the center of the core. In contrast, the penetration depth decreases in the core for the z-component as well as for the y-component. Since the x-component is the dominant component for the $\mathrm{HE}_{1\mathrm{Co-SPin}}^{x}$ mode, the total power of the mode is majorly defined by the x-component. Having a mode profile whose power is concentrated in the core led many to misidentify the mode as the fundamental photonic mode.[101,102] Regardless of the shape of the x-component, the mode is a plasmonic mode that can be clearly seen in the surface confined y- and z-components in **Figure 4e** and **Figure 5**. Meanwhile, as the core radius a decreases, the penetration depth in the metal reduces slightly for all field components. This is an important feature indicating the plasmonic mode size shrinks with the decreasing dimension of the waveguide or the core radius a. Owing to this characteristics, the fundamental plasmonic mode can be confined in a subwavelength metallic aperture without limitation in its size.

Besides this change in the mode's field profile, the ratios between different field components change with the decreasing core radius a. We calculate the field components ratios that are $|E_y|^2/|E_x|^2$ (blue dashed line) and $|E_z|^2/|E_x|^2$ (blue solid line) depending on the core radius a and plot them in **Figure 6**. As the core radius a decreases, the y- and z-component's field strengths decrease compared with the dominant x-component up until a core radius a of 120 nm. This is the inflection point of the dispersion curve where the concave-down curve changes to a concave-up curve as it can be seen in Inset 2 in **Figure 4a**. With this change, the y- and z-component's field strengths start to increase but never becomes larger than the x-component for the fundamental quasi x-polarized plasmonic mode.

This means that regardless of the core radius a, the x-component is the ever dominant component for the $\mathrm{HE}_{1\mathrm{Co-SPin}}^{x}$ mode. Since only this mode reaches the tip aperture, it defines the aperture tip's detection and emission characteristics. Having a dominant transverse component makes the aperture tip mostly sensitive to the transverse field components during the detection and excitation of the near-field.[22,76,103,104]

2.4.3 Fundamental quasi x-polarized hybrid photonic mode in aperture tips

Here, we discuss the properties of the HE_{11}^{x} mode that is the fundamental quasi x-polarized hybrid photonic mode of aperture tips. We calculate the absolute of the electric field components ($|E_x|$, $|E_y|$, and $|E_z|$) at core radiuses a of 2 µm, 405 nm, and 200 nm and present them in **Figure 4f-h**. These positions are noted in the dispersion curve of the mode that is illustrated in a red line in **Figure 4a**. From a core radius a of 2 µm to 200 nm in **Figure 4f-h**, the HE_{11}^{x} mode is a bound mode whose field profile resembles greatly that of a free space focused linearly polarized Gaussian beam.[99] Unlike the fundamental plasmonic mode that experiences massive changes in its field distributions with the decreasing core radius a, this Gaussian-like hybrid photonic mode doesn't change much in shape as it propagates in the tapered waveguide. Even shortly before turning into an evanescent mode (see **Figure 4h**), the mode's field distributions are well preserved. The reason is that the photonic mode remains a bound mode throughout the entire length of the taper while the plasmonic mode changes from a bound mode to a leaky mode as we have discussed in Section 2.4.1.

Profiles of all field components maybe preserved for the fundamental photonic mode but not their relative ratios, and this can be clearly seen in **Figure 4f-h**. We calculate the field components ratios that are $|E_y|^2/|E_x|^2$ (red dashed line) and $|E_z|^2/|E_x|^2$ (red solid line) and plot them in **Figure 6**. As the core radius a decreases, the y- and z-components increase in strength compared with the x-component for the quasi x-polarized fundamental photonic mode, HE_{11}^{x}. This trend continues to accumulate rapidly for the z-component until the core radius a of about 300 nm where $|E_z|^2/|E_x|^2$ reaches about 150. This is the inflection point where the dispersion curve changes from concave-down to concave-up type of curve (see **Figure 4a**). From then on, the z-component starts to decrease in strength, yet it still remains larger than the x-component until the cutoff that is about 1.6× at core radius a of about 150 nm. Meanwhile, the y-component increases in strength with the decreasing core radius a, yet never becomes larger than the x-component. This overall trend shows that the HE_{11} mode's propagation in the aperture tip is akin to the focusing of a free-space Gaussian beam with high NA objectives. As we have mentioned earlier in Section 2.3, the HE_{11} mode's propagation in dielectric

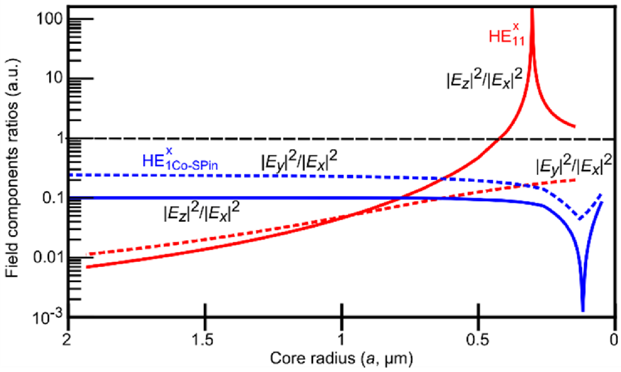

Figure 6. Field components ratios of the fundamental quasi x-polarized plasmonic ($\mathrm{HE}^x_{1\mathrm{Co-SPin}}$ in blue lines) and photonic (HE^x_{11} in red lines) modes depending on the core radius a. The maximum values of y- and z-components are compared with that of the dominant x-component at each core radius a where $|E_y|^2/|E_x|^2$ is in dashed lines, and $|E_z|^2/|E_x|^2$ is in solid lines. Adapted from Reference 76.

tips also has the same behavior. When a Gaussian-like beam or mode is either focused with a lens or is propagated in any type of tapered waveguide, the longitudinal component grows in strength compared with the dominant transverse component, depending on the NA of the lens or the core radius a of the tapered waveguide. The key difference is, however, that the ratio of 150× can only be achieved in aperture tips. The metal cladding forbids the leakage of the photonic mode. Thus, the aperture tip guides the mode long enough till it reaches the evanescent mode region during which the longitudinal field of the HE11 mode accumulates its strength. Conversely, the dielectric tips and lenses cannot keep confining the mode. In dielectric tips, the HE11 mode turns into a leaky mode and escapes the waveguide by changing into free space beam. For the lenses, the Gaussian beam diverges with wider angle after it is focused by a lens escaping the confinement. With a lens focusing, the ratio is always $|E_z|^2/|E_x|^2 < 1$ for the x-linearly polarized Gaussian beam.[8,105,106]

Lastly, it is essential to discuss the propagation loss of the fundamental photonic mode. Below a core radius a of about 500 nm, the imaginary part of the effective index of the mode increases and becomes 2 orders of magnitude greater than that of the fundamental plasmonic mode (see **Figure 4b**). This means that in this region, the fundamental photonic mode suffers from a great amount of propagation loss. We calculate the total power decay of the fundamental photonic mode (red line) and present it in **Figure 7** in comparison with the fundamental plasmonic mode (blue line). The power decay due to the propagation is given as $P(z') = P_0(z_0)\exp\left(-2\int_{z_0}^{z'} \beta''(z)\mathrm{d}z\right)$. Here, the distance to virtual apex (see the inset in **Figure 7**) is $z = \rho/\tan\theta$, and the taper angle of the tip is $\theta = 20°$. The modes are

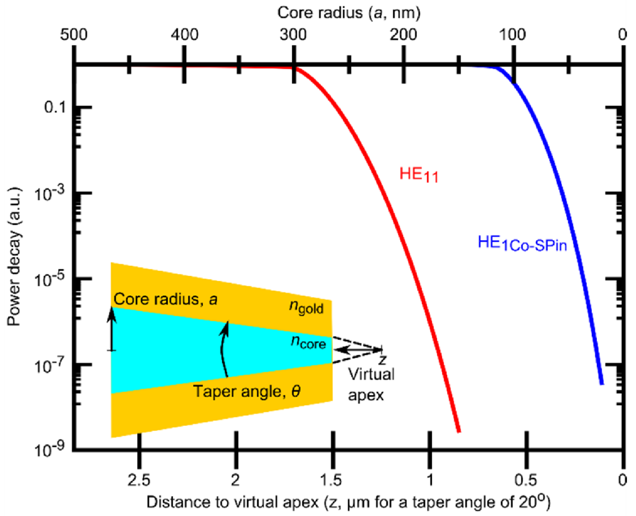

Figure 7. Power decay of the fundamental plasmonic ($\mathrm{HE_{1Co\text{-}SPin}}$, blue lines) and photonic ($\mathrm{HE_{11}}$, red lines) modes depending on the distance to the tip's virtual apex. The cross section of the aperture tip structure is illustrated as an inset where it is shown that the virtual apex locates outside the tip aperture. The total power of each mode is assumed to be unity at a core radius a of 500 nm. Adapted from Reference 76.

assumed to have a total power of unity at a core radius a of 500 nm ($z_0 = 500\ \mathrm{nm}/\tan 20°$ and $P_0(z_0) = 1$). From z_0 until z' where the photonic mode turns to an evanescent mode, the fundamental photonic mode experiences propagation loss of about 9 orders of magnitude. The overall loss of the mode has to include not only the propagation loss but also the coupling to the other modes that are propagating in both forward and backward directions. This hints that the transmission efficiency of the fundamental photonic mode will be less than 10^{-7} percent for an aperture tip with an aperture diameter of 300 nm.

2.4.4 Coupling between fundamental plasmonic and photonic modes

The coupling mechanism between the photonic and plasmonic modes can be anticipated from the dispersion curves of the modes. As we have discussed in Section 2.4.1 and shown in **Figure 4a**, the dispersion curves of the modes no longer change in an adiabatic manner below the core radius a of about 600 nm. The slopes of the curves become much steeper, and the effective indices change rapidly over a short distance. This means that the local modes, $\mathrm{HE_{11}}$ and $\mathrm{HE_{1Co\text{-}SP}}$, can no longer be approximated as the eigen modes of the tapered waveguide despite the small taper angle. Eigen modes would be orthogonal to each other so there would be no coupling between them. However, due to this non-adiabaticity, the orthogonality relation between the local modes is no longer valid. Consequently, there can and should occur coupling between not only $\mathrm{HE_{11}}$ and $\mathrm{HE_{1Co\text{-}SP}}$ local modes but also to the other modes including the back-propagating counter parts of the individual modes.

Here, we would like to estimate how much power can be transferred to the plasmonic mode when there exist only the photonic mode at the beginning of the taper. To calculate the coupling efficiency between the HE_{11} and $\mathrm{HE}_{1\mathrm{Co\text{-}SP}}$ modes in a tapered waveguide, we use the coupled mode theory for a nonuniform waveguides.[71,107,108] For the sake of simplicity, we only consider here the coupling between the forward propagating fundamental photonic and plasmonic modes. The evolution of the amplitudes of the photonic ($A_{\mathrm{ph}}\,(z)$) and the plasmonic ($A_{\mathrm{pl}}\,(z)$) modes can be evaluated as

$$\frac{dA_{\mathrm{ph}}(z)}{dz} = \alpha_{\mathrm{pl}\to\mathrm{ph}}(z)A_{\mathrm{pl}}(z) - i\beta_{\mathrm{ph}}(z)A_{\mathrm{ph}}(z), \tag{12a}$$

and

$$\frac{dA_{\mathrm{pl}}(z)}{dz} = \alpha_{\mathrm{ph}\to\mathrm{pl}}(z)A_{\mathrm{ph}}(z) - i\beta_{\mathrm{pl}}(z)A_{\mathrm{pl}}(z). \tag{12b}$$

Here, β_{ph} and β_{pl} are the propagation constants of the photonic and plasmonic modes that can be calculated by Equation (11) with a minus sign in front of the square root. $\alpha_{1\to2}$ is the coupling coefficient that describes the coupling strength from the mode 1 to the mode 2 and depends on the field overlap integral and the phase matching between the modes. Thus, the coupling coefficient $\alpha_{1\to2}$ is given as

$$\alpha_{1\to2}(z) = \frac{\omega\varepsilon_0(\varepsilon_{\mathrm{core}} - \varepsilon_{\mathrm{gold}})a\tan(\frac{\theta}{2})}{4P_2(\beta_2 - \beta_1)}\int_0^{2\pi}\left(\frac{\varepsilon_{\mathrm{core}}}{\varepsilon_{\mathrm{clad}}}E_\rho^1E_\rho^2 + E_\varphi^1E_\varphi^2 + E_z^1E_z^2\right)\Big|_{\rho=a}\mathrm{d}\varphi, \tag{13}$$

where θ is the taper angle. The subscripts 1 and 2 can be replaced either with ph or pl that denote photonic or plasmonic. P_2 is the mode's normalization factor given by the total time averaged power of the mode 2, and $E^{1,2}$ are the electric fields of modes 1 and 2. P_2 and $E^{1,2}$ can be found with Equations (6) and (7) when $A = 1$. As we have mentioned in Section 2.2 , the tapered waveguide is considered as a sequence of cylinders with an infinitesimal length and a decreasing cross section. If the waveguide is uniform or the taper angle θ is 0, there would be no coupling between modes and thus the coupling coefficient would be 0. When $\theta \neq 0$, however, the two neighboring cylinders have different cross sections so there exist discrepancies along the circumference of the conjoined cylinders. Since field perturbations arise at the rim of the waveguide's core, the field overlap integral is only calculated along the circumference of the waveguide core. Furthermore, due to the discontinuity across the boundary, the radial electric field requires some factors in the overlap integral in Equation (13). Details of the equations are given in references 71 and 107.

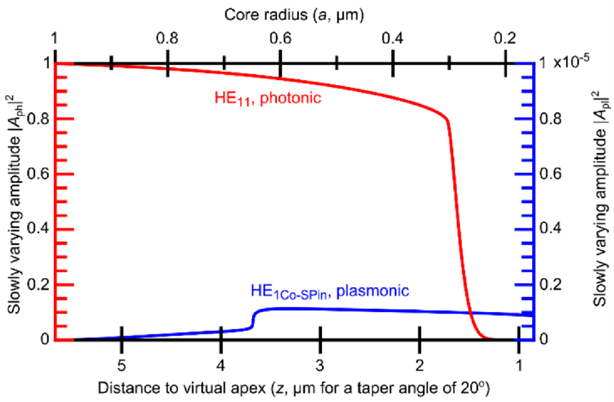

Figure 8. Absolute square of the slowly varying amplitude ($|A|^2$) depending on the distance to the virtual apex z. The HE_{11} mode is depicted with a red line, and the $\mathrm{HE}_{1\mathrm{Co}\text{-}\mathrm{SPin}}$ mode is with a blue line. The tip has a taper angle of 20°. At a core radius a = 150 nm, $|A_{\mathrm{pl}}|^2$ is about 0.9×10^{-6} so the coupling efficiency is estimated to be about 0.0001%. Adapted from Reference 76.

By using Equations (12) and (13), we calculate the absolute square of the slowly changing amplitudes depending on the distance to the virtual apex (see the inset in **Figure 7**) that is calculated for the taper angle θ of 20°. The results are presented in **Figure 8** where the amplitudes of the fundamental photonic and plasmonic modes are plotted in red and blue lines, respectively. At a core radius a of 1 µm, the photonic mode is considered to have an amplitude A_{ph} of 1 while the plasmonic mode has $A_{\mathrm{pl}} = 0$. Since the squared mode amplitude is proportional to the total power of the mode, both $|A_{\mathrm{pl}}|^2$ and $|A_{\mathrm{ph}}|^2$ represent the relative mode powers at a particular core radius a. For the plasmonic mode, $|A_{\mathrm{pl}}|^2$ at a certain core radius a (~50 nm) shows not only the gained power but also the total transmission efficiency of the aperture tip. As shown in **Figure 8**, $|A_{\mathrm{pl}}|^2$ is about 0.9×10^{-6} at a core radius a of 150 nm so the coupling efficiency from the photonic mode to the plasmonic mode is estimated to be about 0.0001%. Meanwhile, $|A_{\mathrm{ph}}|^2$ reduces with the decreasing core radius a due to the propagation loss and the coupling to the plasmonic mode and eventually becomes about 10^{-9} at a core radius a of 150 nm. From these calculations, it is clear that the transmission efficiency of the plasmonic mode is at least 3 orders of magnitude greater than that of the photonic mode.

The plasmonic mode's amplitude increases depending on the coupling coefficient ($\alpha_{\mathrm{ph}\to\mathrm{pl}}$), and there can be different reasons for the increase of the coupling coefficient. As we have mentioned at the beginning of the section, the coupling is inevitably due to the increased non-adiabaticity of modes toward the tip aperture. Besides this non-adiabaticity, the imaginary part of the propagation constant increases with decreasing core radius, and this imaginary part indicates not only the propagation loss of the modes but also the radiative loss. The high radiative loss, in case of our aperture tip, is responsible for the efficient coupling between the modes.[109] Furthermore, due to the tapered waveguide geometry, there seems to occur complex effects that result in the efficient field confinement of modes at particular core radiuses and eventually increase the coupling efficiency. For example, there can happen a radius dependent modal resonance[109–112] and a constructive interference between forward and backward propagating waves.[113] The modes can become resonant at a particular core radius a as if this part of the waveguide is a locally resonant metallic nanohole.[109,114] Metallic and dielectric cylindrical rods are shown to exhibit resonant behaviors at different wavelengths of the incident beam depending on their material constituents and geometrical parameters.[109–112] A uniform cylindrical rod shows resonance at a particular wavelength that shifts toward the red spectral region with the increasing radius of the cylindrical rod. To achieve a broad band of resonance spectrum from one sample, one can put together many cylindrical rods with different radiuses each offering different resonant wavelength.[112] Collectively, the sample will have a broad resonance spectrum. A more elegant way to realize this goal would be tapering the waveguide. Different section of the tapered waveguide have a different radius, and thus one tapered waveguide alone can act like many cylindrical rods with different sizes.[112] Hence, a tapered waveguide offers always a local resonance regardless of the incident beam wavelength or the material. For a fixed wavelength, a mode of the aperture tip is inevitably to experience a local resonant effect at a particular core radius a. When such mode resonance happens, the mode's fields are highly enhanced resulting in an increase of the coupling coefficient according to Equation (13). The plasmonic mode becomes resonant at a core radius a of 650 nm, and thus at this point, the amplitude increases at this point as it can be seen in **Figure 8**.

2.4.5 Which mode participates in the near-field interaction outside the tip aperture?

In the previous sections, we have discussed about the properties of the fundamental photonic and plasmonic modes and the coupling between them. Based on our analytical study in comparison with the previously reported experimental results, we aim to determine which mode or modes play the main role in the near-field interaction outside the tip aperture during SNOM measurements with aperture tips. Until recently, the aperture tip's functionality was explained with the fundamental photonic mode. It was commonly assumed that the evanescent decay of the fundamental photonic mode is transmitted through the tip aperture participating in the near-field interaction outside the tip aperture and determining the aperture tip's behavior.[115] However, there are several facts that suggest the fundamental photonic mode is not the main player in the near-field interaction outside the tip aperture but the fundamental plasmonic mode. *First*, the circular aperture tips are known to detect[22,103,104] (in collection) and excite[75,76,116] mostly transverse field components in near-field measurements. For the fundamental photonic mode, HE_{11}^{x}, the longitudinal z-component dominates at a small core radius a below 450 nm. This means that if the HE_{11}^{x} mode determines the near-field interaction outside the tip aperture, aperture tips should be sensitive to the z-component and thus contradicting the experimental results presented in references 22, 103 and 104. Meanwhile, the fundamental plasmonic mode, $\mathrm{HE}_{1\mathrm{Co-SPin}}^{x}$, has dominant transverse field components at any core radius a as was shown in **Figure 6**. Thus, if the fundamental plasmonic mode participates in the near-field interaction outside the tip aperture, the tip should excite and detect mostly the transverse field components just like what experimental results suggest. *Second*, the transmission efficiency of the photonic mode is several orders of magnitude smaller than that of the plasmonic mode. The power decay due to the propagation loss alone is about 10^{-9} for the fundamental photonic mode at a core radius a of 150 nm. If we include loss due to the coupling to other modes that are propagating in forward and backward directions, scattering, and the decay in the evanescent mode region, the total loss will increase by several orders of magnitude. Contrariwise, the transmission efficiency, including the coupling efficiency and the propagation loss, of the plasmonic mode is estimated to be about 0.0001% at a core radius a of 150 nm. Consequently, the fundamental photonic mode is unlikely to reach the tip aperture with a size of about 100 nm; instead, the fundamental plasmonic mode will be excited and participate in the near-field interaction outside the tip aperture. *Last but not least*, we have was shown experimentally that the measured near-field of an aperture tip is better explained with the fundamental plasmonic mode.[76] Polarization resolved near-field images of aperture tips were obtained and correlated with the different field components of the plasmonic and photonic modes. By comparing both the pattern and intensity ratios, it was concluded that the near-field of an aperture tip is best explained with the fundamental plasmonic mode.

2.4.6 Influence of the cladding metal type

So far, our analytical calculations are made for aperture tips with gold claddings so based on them, we made our conclusion in the previous section. However, we would like to stress that our conclusion remains valid for aperture tips with different metal claddings such as silver or aluminum. The fundamental plasmonic mode reaches the tip aperture and participates in the near-field interaction outside the tip aperture regardless of the metal cladding type. To demonstrate our claim, we performed the same calculations as we have done in Section 2.4.1. Parameters used in this calculation are a core refractive index of $n_{\text{core}} = 1.4535$, a laser vacuum wavelength of $\lambda_0 = 784$ nm, a silver refractive index of $n_{\text{silver}}(\lambda_0) = \sqrt{-23.75 + 1.78i}$, and an aluminum refractive index of $n_{\text{aluminum}}(\lambda_0) = \sqrt{-63.44 + 43.95i}$.

We calculate the dispersion relations of the fundamental plasmonic (blue lines) and photonic (red lines) modes for aperture tips with silver (solid lines) and aluminum (dashed lines) cladding and present the results in **Figure 9**. The real and imaginary parts of the effective indices are presented in **Figure 9a** and **b**, respectively. Inset 1 in **Figure 9a** illustrates the structure that is a dielectric cylinder with a core radius a and an infinitely large metal cladding. Inset 2 in **Figure 9a** shows the close-up region where the plasmonic bound modes turn into leaky modes by having real parts of the effective indices smaller than the core refractive index. The results presented in **Figure 9** are very similar to the ones we have already shown in **Figure 4** in Section 2.4.1. Based on these results, we can make three general conclusions. *First*, the fundamental photonic mode always experiences cutoff before reaching the tip aperture, typically at 100 nm in diameter, regardless of the cladding metal type. *Second*, the fundamental plasmonic mode does not experience cutoff and thus can reach all the way to the tip aperture. *Third*, the imaginary part of the effective index increases for the photonic mode toward the

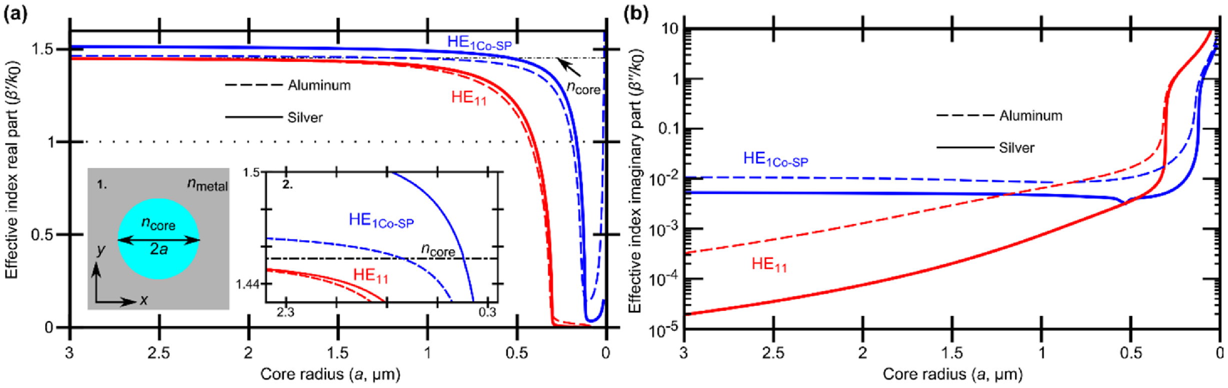

Figure 9. (a) Effective indices' real parts for the fundamental plasmonic (HE$_{1\text{Co-SPin}}$, blue curve) and photonic (HE$_{11}$, red curve) modes depending on the core radius a. Inset 1 illustrates the waveguide structure that has a dielectric core with a radius of a and an infinitely large metal cladding. Meanwhile, Inset 2 shows the region where the plasmonic mode changes from a bound mode to a leaky mode. **(b)** Effective indices' imaginary parts for the fundamental plasmonic (blue dashed curve) and photonic (red dashed curve) modes depending on the core radius a. The dispersion relations of silver and aluminum tips are plotted in solid and dashed lines, respectively. Parameters used in the calculation are a core refractive index of $n_{\text{core}} = 1.4535$, a laser vacuum wavelength of $\lambda_0 = 784$ nm, a silver refractive index of $n_{\text{silver}}(\lambda_0) = \sqrt{-23.75 + 1.78i}$, and an aluminum refractive index of $n_{\text{aluminum}}(\lambda_0) = \sqrt{-63.44 + 43.95i}$. Adapted from Reference 76.

tip aperture and eventually becoming larger than that of the plasmonic mode. This means that due to the propagation loss, the photonic mode is highly likely to die off before reaching the tip aperture.

The cladding metal type, however, influences the plasmonic mode's characteristics and the transmission efficiency of the aperture tip. If we look at the effective indices of the plasmonic mode in an aluminum tip (blue dashed curve) and in a silver tip (blue solid curve) in Inset 2 in **Figure 9a**, the effective index of the plasmonic mode in the aluminum tip becomes smaller than the core refractive index at a larger core radius a than the silver tip. This means that the plasmonic mode in the aluminum tip turns into a leaky mode earlier than that of the silver tip. The reason of such behavior is that aluminum exhibits poor plasmonic effect toward the red spectral range, and our calculation wavelength is 784 nm. Furthermore, aluminum is highly lossy at this wavelength so the propagation loss of the photonic mode is expected to be significantly larger than the aperture tips with silver or gold claddings. We calculate the propagation loss of the fundamental photonic mode as we did in **Figure 7**. When the power decay is calculated from the core radius a of 500 nm to 50 nm for a taper angle of 20°, the power decay of the photonic mode is about 10^{-29} while plasmonic mode has about 10^{-6}. Meanwhile, the permittivity of the silver is quite close to that of the gold so the propagation losses of the modes in silver tips is in a similar range to that of the gold tips.

Summarizing Section 2.4 , we would like to stress once more that the aperture tips are plasmonic in nature contrary to the previous SNOM paradigm. The fundamental plasmonic mode, not the photonic one, reaches the tip aperture participating in the near-field interaction and determining the excitation and detection behaviors of the tip. Our conclusion may be obvious if we think of the nature of light as photonic modes or beams are reluctant to be squeezed into subwavelength region due to the diffraction limit. As soon as the photonic mode is confined enough in the aperture tip, it escapes the confinement either through loss or reflection. Meanwhile, the plasmonic fields are naturally confined in transverse axis perpendicular to the propagation axis so as the waveguide dimension shrinks, the plasmonic mode size reduces in size adapting to the structure.

2.5 Plasmonic tips

In this section, we will discuss the plasmonic tip that is a tapered and fully metal-coated fiber as shown in **Figure 1c**. Before we start analyzing modes in the plasmonic tip, it is good to remind oneself of the assumptions that were discussed previously in Section 2.2 . In the first assumption, we considered that the metal cladding thickness is thick so the third medium can be neglected when calculating modes. For example, the surrounding medium was not considered when we calculate the photonic and plasmonic modes in aperture tips. This assumption is still valid for plasmonic tips since the coating thickness d is about 50 – 100 nm while the penetration depth of fields is no greater than 20 nm. Hence, the photonic mode within the tapered fiber core and the plasmonic mode on the gold-surrounding medium interface are weakly coupled in plasmonic tips so we can consider the photonic and plasmonic modes separately and describe their interaction in the framework of a perturbation theory. The photonic mode is analyzed in a cylindrical waveguide with a dielectric fiber core and an infinitely large metal cladding. Meanwhile, the plasmonic mode is obtained in a cylindrical waveguide with a metallic core and an infinitely large dielectric cladding (surrounding medium). With this assumption in mind, we proceed with our analysis. In Section 2.5.1, we first discuss the plasmonic modes on the outer metallic layer neglecting the dielectric fiber core. Here, we will show that the radially polarized plasmonic mode (E_ρ,0, E_z) is crucial for the operation of the plasmonic tip. Under the weakly coupled modes assumption, we study the resonant excitation of the radially polarized plasmonic mode by the radially polarized photonic mode in Section 2.5.2. In Sections 2.5.1 and 2.5.2, the plasmonic tip is considered to be in air so the surrounding medium's refractive index is $n_{\text{surr}} = 1.0$. Since the plasmonic mode is at the metal-surrounding medium outer interface, it is strongly influenced by the surrounding medium change. We consider different surrounding media and their influences on the coupling efficiency and the plasmonic mode in Section 2.5.3. Calculation parameters in this section are a fiber refractive index of $n_{\text{fiber}} = 1.4474$,[69] a gold refractive index of $n_{\text{gold}}(\lambda_0) = \sqrt{-20.95 + 1.68i}$,[100] and a laser vacuum wavelength of λ_0= 784 nm.

2.5.1 Conical plasmonic modes on the outer metallic surface of plasmonic tips

In this section, we consider a gold conical waveguide structure in a dielectric surrounding medium to analyze conical surface plasmonic (Co-SP) modes at the outer gold surface of a plasmonic tip. The inset in **Figure 10a** illustrates the cross section of the waveguide structure. To distinguish plasmonic modes from photonic modes within the tapered fiber, we denote the plasmonic modes as νCo-SP where ν is the azimuthal mode number. We use equations (6) and (7) to find the dispersion relations of the plasmonic modes. In these equations, the transverse wavevectors are given as $\zeta = \sqrt{\beta^2 - k_0^2\varepsilon_{\text{gold}}}$ and $\gamma = \sqrt{k_0^2\varepsilon_{\text{surr}} - \beta^2}$ where the core and cladding dielectric constants are $\varepsilon_1 = \varepsilon_{\text{gold}}$ and $\varepsilon_2 = \varepsilon_{\text{surr}}$. For calculating dispersion relations of HE ($\nu \neq 0$) and TM ($\nu = 0$) modes, we

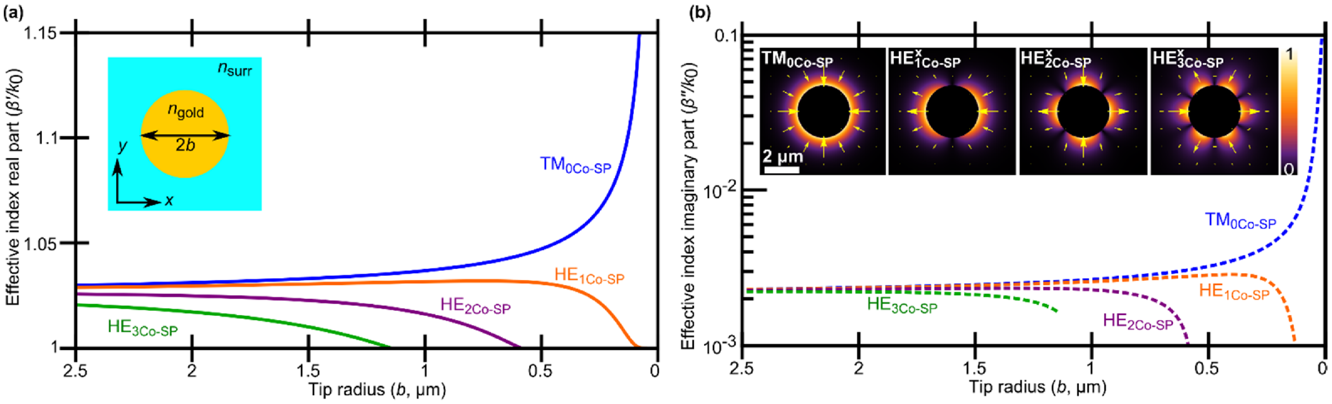

Figure 10. (a,b) Effective indices of conical plasmonic modes on the outer surface of the plasmonic tip depending on the plasmonic tip's radius b. The real (a) and imaginary (b) parts are in solid and dashed lines, respectively. The inset in (a) shows the waveguide structure that has a gold core (n_{gold}) with a radius b and an infinitely large dielectric cladding or the surrounding medium (n_{surr}). The fundamental and radially polarized plasmonic mode is labelled as $\text{TM}_{0\text{Co-SP}}$ and is plotted in blue. The higher order hybrid quasi x-polarized plasmonic modes are labelled as $\text{HE}^{\text{x}}_{1\text{Co}-\text{SP}}$, $\text{HE}^{\text{x}}_{2\text{Co}-\text{SP}}$, and $\text{HE}^{\text{x}}_{3\text{Co}-\text{SP}}$ that are plotted in orange, magenta, and green, respectively. Each mode's transverse electric field distribution ($\mathcal{Re}[\mathbf{E}_\perp]$) is calculated at a tip radius b of 1.5 μm and included as an inset in (b). The yellow arrows point the electric field vector's direction.

use Equation (11) with a minus sign in front of the square root in Section 2.2 . This equation describes the dispersion relations of the HE type of modes that have the transverse magnetic nature, and thus it is suitable for expressing the plasmonic modes.

Dispersion relation. First, we calculate the effective indices of the 4 lowest order conical plasmonic modes as a function of the tip radius b and plot the results in **Figure 10**. The effective indices' real and imaginary parts are shown in **Figure 10a** and **b**, respectively for the $\text{TM}_{0\text{Co-SP}}$ (blue), $\text{HE}_{1\text{Co-SP}}$ (orange), $\text{HE}_{2\text{Co-SP}}$ (magenta), and $\text{HE}_{3\text{Co-SP}}$ (green) modes. The insets in **Figure 10b** show the transverse electric field ($\mathcal{Re}[\mathbf{E}_\perp]$) profiles of these 4 lowest order modes. The electric field's real part is calculated at a tip radius b of 1.5 μm for each mode, and the yellow arrows show the transverse electric field's vector direction.

The inset in **Figure 10b** shows that the fundamental plasmonic mode ($\text{TM}_{0\text{Co-SP}}$) is radially polarized and has no azimuthal variation. As the fundamental plasmonic mode propagates toward the tip apex, its effective index (both the real and imaginary parts) increases without experiencing mode cutoff. The increase of the effective index's real part means that the phase velocity of the mode decreases, and the oscillation period or the effective wavelength of the mode shrinks toward the tip apex. Hence, the $\text{TM}_{0\text{Co-SP}}$ mode can reach all the way to the tip apex while shrinking in mode size in longitudinal direction (along z-axis). Furthermore, since the fundamental plasmonic $\text{TM}_{0\text{Co-SP}}$ mode is radially polarized, the electric field vector is symmetric around the tip axis (z-axis). For this reason, the $\mathrm{TM}_{0\mathrm{Co}\text{-}\mathrm{SP}}$ mode is sometimes called symmetric mode.[67] When such plasmonic electric fields reach the tip apex, the fields interfere constructively creating a strong longitudinal field ($E_{\parallel} = E_z$) along the tip axis. Therefore, there occurs two interesting effects to the $\mathrm{TM}_{0\mathrm{Co}\text{-}\mathrm{SP}}$ mode, those are the shrinking effective wavelength and the increasing longitudinal field strength during the propagation toward the tip apex. These two features enable the mode to be confined at a subwavelength apex without any restriction in its geometrical size. As a whole, this phenomenon is called plasmon superfocusing.[57–59] One drawback here is that the mode becomes more lossy toward the tip apex as it can be seen in **Figure 10b**. So the propagation loss effect competes with the field enhancement due to the shrinking size and also the superfocusing effect. The $\mathrm{TM}_{0\mathrm{Co}\text{-}\mathrm{SP}}$ mode can be excited resonantly by a radially polarized photonic mode within the core of the tapered fiber where the decreasing tip radius b enables the phase matching between the modes. This resonant excitation process will be discussed later in Section 2.5.2.

Meanwhile, the higher order hybrid quasi x-polarized plasmonic modes ($\mathrm{HE}^{\mathrm{x}}_{1\mathrm{Co-SP}}$, $\mathrm{HE}^{\mathrm{x}}_{2\mathrm{Co-SP}}$, and $\mathrm{HE}^{\mathrm{x}}_{3\mathrm{Co-SP}}$) are shown as insets in **Figure 10b**. Contrary to the fundamental plasmonic mode, their effective indices (both real and imaginary parts) decrease as the tip radius b decreases. More importantly, their effective indices' real parts approach the refractive index of the surrounding medium that is $n_{\mathrm{surr}} = 1$ at different tip radiuses of b. This means that these higher order plasmonic modes experience cutoff at different tip radiuses of b and radiate out of the plasmonic tip becoming free space beams. The lower the mode order is, the closer the mode propagates to the apex. Thus, the $\mathrm{HE}_{1\mathrm{Co}\text{-}\mathrm{SP}}$ mode reaches closest to the tip apex, at a tip radius b of 53 nm for our chosen tip parameters. If the plasmonic tip has an apex size greater than 106 nm, the $\mathrm{HE}_{1\mathrm{Co}\text{-}\mathrm{SP}}$ mode can exist near the tip apex along with the $\mathrm{TM}_{0\mathrm{Co}\text{-}\mathrm{SP}}$ mode. However, as it can be seen in the inset in **Figure 10b**, this higher order hybrid mode has an asymmetric field distribution meaning that if it reaches the tip apex, the plasmonic fields will interfere destructively at the apex. We can, thus, anticipate that the $\mathrm{HE}_{1\mathrm{Co}\text{-}\mathrm{SP}}$ mode probably does not participate in the near-field interaction at the tip apex. In general, even higher order plasmonic modes have symmetric field vectors while the odd ones are asymmetric as it can be seen in the inset in **Figure 10b**. Since the higher order modes other than the $\mathrm{HE}_{1\mathrm{Co}\text{-}\mathrm{SP}}$ mode cannot reach close enough to the apex of a typical plasmonic tip (< 200 nm), their field vectors' symmetry is not of interest to us.

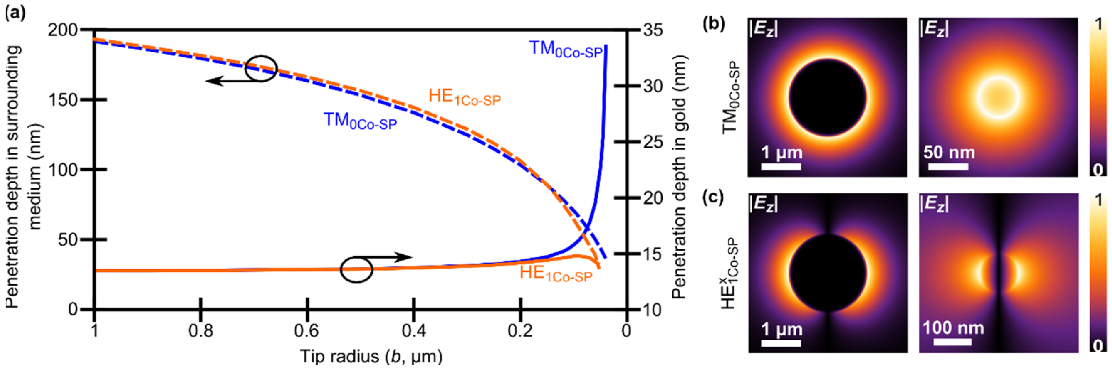

Figure 11. (a) Penetration depth of fields in a gold core (solid lines) and in a surrounding medium cladding (dashed lines) depending on a tip radius *b*. The penetration depth is calculated for the absolute square of the electric field's z-component ($|E_z|^2$). We consider only two lowest order modes, TM$_{0\text{Co-SP}}$ (blue) and HE$_{1\text{Co-SP}}$ (orange) since they are likely to exist at the tip apex for a tip with apex size of about 100 nm. **(b)** Absolute of the electric field's z-component ($|E_z|$) of the TM$_{0\text{Co-SP}}$ mode at a tip radius *b* of 1 μm (left) and 25 nm (right). **(c)** Absolute of the electric field's z-component ($|E_z|$) of the HE$_{1\text{Co-SP}}$ mode at a tip radius *b* of 1 μm (left) and 53 nm (right). The penetration depth increases in the core for the TM$_{0\text{Co-SP}}$ mode and thus starts to overlap in the metal core. Meanwhile, it is never the case for the higher order modes. The penetration depth decreases in the surrounding medium as the tip radius decreases meaning that the mode size shrinks with the structure dimension for both modes.

The higher order hybrid modes can be excited with respective hybrid photonic modes within the tapered fiber core. For example, the HE$^x_{1\text{Co}-\text{SP}}$ plasmonic mode can be excited with the HE$^x_{11}$ photonic mode that is the Gaussian-like fundamental photonic mode in the fiber core of the plasmonic tip. We will not discuss the excitation process of these hybrid plasmonic modes in detail since we are only interested in the fundamental and radially polarized plasmonic mode (TM$_{0\text{Co-SP}}$) that possesses the superfocusing capability.

The dispersion relations of the plasmonic modes give us the general understanding of the plasmonic modes in the plasmonic tips. To understand each mode in more detail, we take a look at the evolution of the field's penetration depth and field components' ratios during the propagation toward the tip apex.

Penetration depth of fields. Next, we calculate the penetration depth of the electric field's z-component (E_z) in the gold core (solid lines) and in the surrounding medium cladding (dashed lines) depending on a tip radius *b* and plot the results in **Figure 11a**. We choose the electric field's z-component because of its continuity over the metal-surrounding medium boundary. The penetration depth of a field is defined as the radial distance from the tip radius *b* to the point where $|E_z(\rho = b)|^2$ decreases by 1/e. We consider the fundamental TM$_{0\text{Co-SP}}$ (blue lines) mode and the 1st order hybrid HE$_{1\text{Co-SP}}$ (orange lines) mode since the hybrid higher order plasmonic modes behave in similar manner.

As both plasmonic modes propagate toward the apex, the penetration depth in the surrounding medium (dashed lines in **Figure 11a**) decreases with decreasing tip radius b. This means that the mode sizes of these plasmonic modes shrink with the decreasing structure dimension. Besides the longitudinal confinement, due to the increasing effective index of the $\mathrm{TM}_{0\mathrm{Co\text{-}SP}}$ mode (blue line in **Figure 10a**) towards the tip apex, this shrinking size of the $\mathrm{TM}_{0\mathrm{Co\text{-}SP}}$ mode in transverse axis allows the electromagnetic field to be confined at the tip apex without restriction on the tip radius b. Contrary to the 3D confinement of the $\mathrm{TM}_{0\mathrm{Co\text{-}SP}}$ mode in the plasmonic tip, the fundamental photonic mode in dielectric tips expands more and more and eventually escapes the waveguide with the decreasing tip size as we have discussed in Section 2.3. This difference highlights the advantange of plasmonic modes with their the ability to be confined in subwavelength region without limitation in dimension.[48,59,117]

Meanwhile, the penetration depth in the gold core behaves quite differently for the $\mathrm{TM}_{0\mathrm{Co\text{-}SP}}$ (solid blue line) and $\mathrm{HE}_{1\mathrm{Co-SP}}^{\mathrm{x}}$ (solid orange line) modes as it can be seen in **Figure 11a**. To illustrate this difference, we calculate the electric field profile ($|E_z|$) of the $\mathrm{TM}_{0\mathrm{Co\text{-}SP}}$ mode at a tip radius b of 1 µm (left) and 25 nm (right) and show the results in **Figure 11b**. As the tip radius b decreases, the penetration depth in the gold core increases for the $\mathrm{TM}_{0\mathrm{Co\text{-}SP}}$ mode and starts to overlap resulting in the field enhancement in the core. The enhanced field will drive the free electron oscillations harder along the tip axis in the gold core, and thus the plasmonic field is enhanced even more. Owing to this process, there occurs the plasmonic superfocusing effect: the field is confined both longitudinally and transversally, and the field amplitude is enhanced due to the decreasing tip radius b towards the tip apex and also the in-phase free electron oscillations in the metal core all around the tip radius.[57–59] As it can be seen in **Figure 11a**, the superfocusing effect happens close to the tip apex where the tip radius b is below 40 nm for our calculation parameters. With the increasing laser operation wavelength, it is expected that this threshold tip radius b will increase since the effective size of the apex compared with the wavelength will be small. The transverse fields of the $\mathrm{TM}_{0\mathrm{Co\text{-}SP}}$ mode, however, do not overlap in the gold core, and the penetration depth of transverse fields decrease slightly towards the tip apex avoiding overlap of fields in the core. Meanwhile, **Figure 11c** shows the electric field profile ($|E_z|$) of the $\mathrm{HE}_{1\mathrm{Co-SP}}^{\mathrm{x}}$ mode at a tip radius b of 1 µm (left) and 53 nm (right). Contrary to the fundamental $\mathrm{TM}_{0\mathrm{Co\text{-}SP}}$ mode, the penetration depth of fields in the gold core increases only by a small amount near the tip radius b of 100 nm and then decreases until the mode experiences cutoff. Not only do the fields destructively interfere at the tip apex due to the field vector's asymmetry,

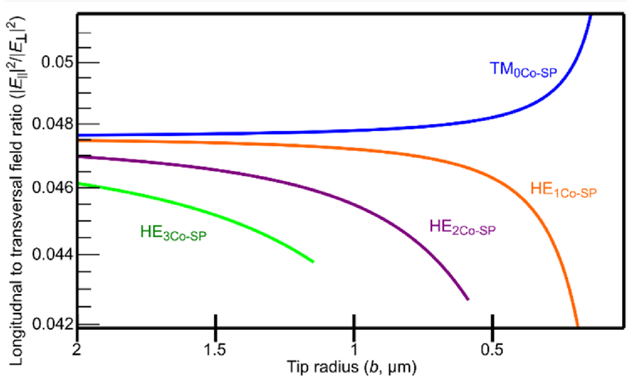

Figure 12. Longitudinal to transverse field ratios ($|E_{\|}|^2/|E_{\perp}|^2$) of $\mathrm{TM_{0Co\text{-}SP}}$ (blue), $\mathrm{HE^{x}_{1Co-SP}}$ (orange), $\mathrm{HE^{x}_{2Co-SP}}$ (magenta), and $\mathrm{HE^{x}_{3Co-SP}}$ (green) modes. Except for the fundamental plasmonic mode, the longitudinal field strength weakens compared with the transverse one for all higher order hybrid modes.

the fields do not overlap in the core and amplify the electron oscillation for the $\mathrm{HE^{x}_{1Co-SP}}$ mode. Therefore, the superfocusing effect doesn't occur for higher order hybrid plasmonic modes. This is the reason why the radially polarized fundamental $\mathrm{TM_{0Co\text{-}SP}}$ mode is crucial in the plasmonic tips' operation.

Field components ratios. Last but not least, we calculate the ratios between maximum of the longitudinal ($E_{\|} = E_z$) and transverse ($E_{\perp} = \sqrt{E_x^2 + E_y^2}$) fields of different modes and plot the results in **Figure 12**. As we showed in the previous part, the longitudinal field is important in achieving the superfocusing effect in the plasmonic tip's. Hence, the increase of the longitudinal field will enhance the superfocusing effect. As **Figure 12** shows, the longitudinal field of the $\mathrm{TM_{0Co\text{-}SP}}$ mode (blue) increases as the tip radius b decreases. At a tip radius b of 25 nm, the longitudinal to transverse field intensity ratios ($|E_{\|}|^2/|E_{\perp}|^2$) reaches 0.1. The ratio continues to increase with decreasing tip radius b, and at a tip radius b of 5 nm, it reaches 0.71. However, we have to keep in mind that our analytical calculation should not be used in the very near vicinity of the tip apex since the analytical model does not consider the roundness of the tip apex. At the very front of the tip apex, it is expected that only the longitudinal field remains due to constructively interfering plasmonic fields.[67,117–119] The finite difference time domain (FDTD) analysis has demonstrated that at the apex of the plasmonic tip, there exist only the longitudinal field.[118,120] The strength of the longitudinal field is thus underestimated with our modal analysis. Despite this fact, we can conclude that when the plasmonic tips are used as a local probe or a detector, the tip is mostly sensitive to the longitudinal field. This characteristic is vastly different from the aperture SNOM tips that are mostly sensitive to the transverse field components as we have discussed in Section 2.4 .[76,103,104]

Meanwhile, for $\mathrm{HE^{x}_{1Co-SP}}$ (orange), $\mathrm{HE^{x}_{2Co-SP}}$ (magenta), and $\mathrm{HE^{x}_{3Co-SP}}$ (green) modes, the longitudinal field decreases in strength compared with the transverse components and reaches a minimum at the mode cutoff radius as it can be seen in **Figure 12**. Experiencing mode cutoff means that these higher order modes are slowly turning into free space beams which usually have extremely weak longitudinal field when not being focused. Hence, this trend of decreasing longitudinal field strength is a natural consequence of the mode cutoff. Furthermore, the lowest order hybrid mode, $\mathrm{HE}_{1\mathrm{Co-SP}}^{\mathrm{x}}$, can reach near the tip apex if the tip apex (tip diameter) is larger than 100 nm. In this case, the plasmonic fields of the $\mathrm{HE}_{1\mathrm{Co-SP}}^{\mathrm{x}}$ mode can interfere destructively at the apex due to the field asymmetry (see the inset in **Figure 10b**).[67,118,119] Thus, the longitudinal field strength is expected to be smaller than what we estimate in **Figure 12**.

In general, one can conclude that the fundamental plasmonic mode's behavior is drastically different in many aspects compared with the other higher order plasmonic modes. The fundamental plasmonic mode is the superfocusing mode that can be confined to a small space by having a decreasing propagation constant and modes size and increasing longitudinal field amplitude with decreasing tip radius b. Owing to the superfocusing effect, the plasmonic tip has the potential to have superior optical and topographic resolutions compared with scattering SNOM tips or aperture SNOM tips once the tip parameters are optimized. Consequently, we aim to excite this fundamental and radially polarized plasmonic mode. The excitation process is discussed in next section.

2.5.2 Resonant excitation of the radially polarized plasmonic mode in plasmonic tips

In this section, we will discuss the resonant excitation of the radially polarized plasmonic mode which has the superfocusing capability. **Figure 13a** illustrates the plasmonic tip and the resonant coupling process between the fundamental and radially polarized plasmonic mode ($\mathrm{TM}_{0\mathrm{Co-SP}}$, blue) and the radially polarized photonic mode (red). The resonant coupling between the radially polarized photonic and plasmonic modes requires two conditions: nonzero field overlap integral and phase matching. First, to achieve a nonzero field overlap integral, we have to employ the same radially polarized photonic mode in the tapered fiber as an excitation source. We need the TM_{01} mode in the tapered fiber. It is the lowest order radially polarized photonic mode in the fiber core so it can propagate closest to the tip apex and thus reducing the propagation length of the plasmonic mode. Second, the phase matching is achieved with the tapering of the waveguide. The effective indices of the photonic and plasmonic mode change with the decreasing radius of the waveguide in an opposite manner. When the radially polarized photonic mode propagates in the tapered fiber core, its effective index decreases with the decreasing core radius a. The opposite happens to the fundamental plasmonic mode; its effective index increases with decreasing tip radius b. At a certain tip radius b, these dispersion curves

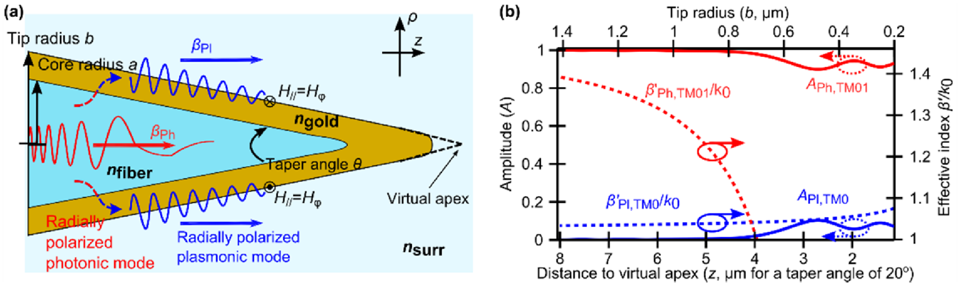

Figure 13 (a) Illustration of the resonant coupling process with the plasmonic tip. The radially polarized photonic mode (TM_{01}) is in a red line, and the radially polarized plasmonic mode ($\mathrm{TM}_{0\mathrm{Co\text{-}SP}}$) on the outer surface of the plasmonic tip in a blue line. **(b)** Real parts of effective indices (β'/k_0, dashed lines) and absolute squares of the slowly varying amplitudes (A, solid lines) for the TM_{01} (red) and $\mathrm{TM}_{0\mathrm{Co\text{-}SP}}$ (blue) modes depending on the distance to the apex z or the tip radius b. These value are calculated for the gold coating thickness d of 100 nm and a taper angle θ of 20°. The coupling amplitude of the $\mathrm{TM}_{0\mathrm{Co\text{-}SP}}$ mode is estimated to be 0.084, and the coupling efficieny ($|A_{\mathrm{Pl}}|^2$) is 0.7%. Adapted from Reference 69.

meet and intersect meaning that the modes are phase matched at this point. Consequently, some of the photonic mode's power transfers evanescently to the plasmonic mode. We can demonstrate this process by calculating the dispersion relation curves and the coupling amplitudes of the radially polarized photonic and plasmonic modes depending on the tip radius b.

The radially polarized plasmonic mode ($\mathrm{TM}_{0\mathrm{Co\text{-}SP}}$) is already calculated and analyzed in Section 2.5.1. We need to do the same calculation for the radially polarized photonic mode (TM_{01}) in the fiber core of the plasmonic tip. As we have mentioned at the beginning of this section, we will consider the photonic and plasmonic modes in the plasmonic tip as weakly coupled. Consequently, the photonic mode is calculated in a cylindrical waveguide with a dielectric fiber core and an infinitely large metal cladding. To find the dispersion relations of the radially polarized photonic mode (TM_{01}) in the fiber core, we use Equation (11) with a minus sign in front of the square root where the azimuthal mode number is $\nu = 0$. We also use equations (6), (7), and (9) for calculating the field components of the TM_{01} mode. In these equations, we have the core and cladding dielectric constants of $\varepsilon_1 = \varepsilon_{\mathrm{fiber}}$ and $\varepsilon_2 = \varepsilon_{\mathrm{gold}}$, respectively. Thus, the transverse wavevectors in the core and the cladding are $\zeta = \sqrt{\beta^2 - k_0^2 \varepsilon_{\mathrm{fiber}}}$ and $\gamma = \sqrt{k_0^2 \varepsilon_{\mathrm{gold}} - \beta^2}$. For the photonic mode, the dispersion relation are found depending on the fiber core radius a. The tip radius b and the core radius a are related through the coating thickness d as $b = a + d$.

We calculate the real part of effective indices (β'/k_0, dashed lines) of the radially polarized photonic (TM_{01} in red) and plasmonic ($\mathrm{TM}_{0\mathrm{Co\text{-}SP}}$ in blue) modes with their respective parameters. The effective indices are plotted in **Figure 13b** depending on the distance to the tip's virtual apex z and the tip radius b. The distance to the tip virtual apex z (along tip axis) is calculated with the tip radius b as $z = b \,/ \tan\theta$ for a taper angle of θ of 20° and a gold coating thickness d of 100 nm. As we can see in **Figure 13b**, the effective indices of the modes cross near the tip radius b of 700 nm, and thus we can expect that the resonant coupling will take place at this point. This resonant coupling point depends on the laser operating wavelength, the coating metal type, and the coating thickness. For a longer wavelength, the mode cutoff shifts to a larger tip radius b so we can anticipate that the resonant coupling point will also move to the larger tip radius b. If the gold coating thickness d decreases say smaller than 100 nm, the dashed red curve in **Figure 13b** will shift to the left while the plasmonic mode's dispersion curve remains at the same position. This is due to the dispersion curve of the photonic mode which is calculated at a different core radius a and then plotted against the tip radius $b = a + d$ by adding the gold coating thickness d. Consequently, we can foresee that the phase matching point shifts to the smaller tip radius b with decreasing gold coating thickness d. This shift of the phase matching point influences the coupling efficiency between the radially polarized photonic and plasmonic modes. We will discuss this effect in Sections 2.5.3 and 2.5.4.

When the phase matching occurs, some of the power of the photonic mode transfers to the plasmonic mode. By using the weakly coupled mode theory, we can calculate this transferred power from the photonic mode to the plasmonic mode or vice versa. Slowly varying amplitudes of the photonic ($A_{\mathrm{Ph}}(z)$) and plasmonic ($A_{\mathrm{Pl}}(z)$) modes at given z can be estimated with the following coupled wave equation

$$\frac{\mathrm{d}A_{\mathrm{Ph}}(z)}{\mathrm{d}z} = i\xi_{\mathrm{Ph}}A_{\mathrm{Ph}}(z) - i\eta_{\mathrm{Pl}}A_{\mathrm{Pl}}(z)\exp\left(-i\frac{|\beta_{\mathrm{Pl}}(z) - \beta_{\mathrm{Ph}}(z)|z}{2}\right), \tag{14a}$$

and

$$\frac{\mathrm{d}A_{\mathrm{Pl}}(z)}{\mathrm{d}z} = i\xi_{\mathrm{Pl}}A_{\mathrm{Co-SP}}(z) - i\eta_{\mathrm{Ph}}A_{\mathrm{Ph}}(z)\exp\left(-i\frac{|\beta_{\mathrm{Pl}}(z) - \beta_{\mathrm{Ph}}(z)|z}{2}\right). \tag{14b}$$

Here, β_{Ph} and β_{Pl} are the propagation constants of the photonic and plasmonic modes, respectively. Furthermore, ξ_{Ph} is the power of the photonic mode in the metal region and ξ_{Pl} is the power of the plasmonic mode in the tapered fiber core region. Meanwhile, η_{Ph} and η_{Pl} are the coupling coefficients of the photonic and plasmonic modes. Equation (14) describes the rate of change of the mode amplitude along z axis for the plasmonic and photonic modes based on their phase matching condition and non-orthogonality. Note that the metal loss is neglected in these calculations since it is expected that the loss will not significantly affect the coupling efficiency calculation. Further details of the equations and their derivations are available in Reference 68.

The slowly varying amplitudes (solid line) of radially polarized photonic (red) and plasmonic (blue) modes are calculated and plotted in **Figure 13b** depending on the tip radius b and the distance to the virtual apex z. We consider the photonic mode amplitude ($A_{\mathrm{Ph}}(b = 1.4\ \mu\mathrm{m}) = 1$) is 1 at a tip radius b of about 1.4 µm while the plasmonic mode amplitude ($A_{\mathrm{Pl}}(b = 1.4\ \mu\mathrm{m}) = 0$) is 0. As we have mentioned earlier, the effective index curves of both modes intersect at a tip radius b of about 700 nm. At this phase matching point, some power of the photonic mode is resonantly transferred to the plasmonic mode at the outer surface of the tip. Hence, the amplitude of the photonic mode decreases while that of the plasmonic mode increases. For our calculation parameter, we estimate that the plasmonic mode amplitude (A_{Pl}) is about 0.084 after the coupling. Since the absolute square of the slowly varying amplitude is proportional to the power of the mode, the absolute square of the plasmonic mode amplitude ($|A_{\mathrm{Pl}}|^2$) is proportional to the gained power or the coupling efficiency. Thus, we estimate that the total coupling efficiency of the plasmonic mode is about 0.7% for a gold coating thickness d of 100 nm.

2.5.3 Influence of the coating thickness on the coupling efficiency

The coupling efficiency depends on the coating material, the coating thickness d, the taper angle θ, the laser wavelength λ_0, and the surrounding medium's refractive index n_{surr}. Here, we would like to observe the change of the coupling efficiency depending on the gold coating thickness d. To do so, we calculate the coupling amplitude ($A_{\mathrm{Pl}}(z_0)$) of the plasmonic mode by the photonic mode at the phase matching or the resonant coupling point of z_0 where $\beta_{\mathrm{Pl}} - \beta_{\mathrm{Ph}} = 0$. The solution of Equation (14) can be well approximated to Landau-Zener formula to estimate the coupling amplitude as

$$A_{\mathrm{Pl}}(z_0) = 1 - \exp\left(-2\pi\frac{\delta^2}{\upsilon}\right). \tag{15}$$

Here, $\delta^2 = \eta_{\mathrm{Ph}} * \eta_{\mathrm{Pl}}$ is the coupling constant that is described by the overlap integral of the individual mode's field profile. Having a large coupling constant (δ^2) means that the coupling between the modes are efficient. Moreover, $\upsilon = \left.\frac{d|\beta_{\mathrm{Pl}}-\beta_{\mathrm{Ph}}|}{dz}\right|_{z=z_0}$ describes the rate of change of the propagation constant (β) difference with respect to z. The smaller the υ parameter is, the longer the interaction length is for the photonic and plasmonic modes, and thus higher the coupling efficiency. Consequently, Equation (15) calculates the coupling amplitude ($A_{\mathrm{Pl}}(z_0)$) based on the overlap of fields as well as the

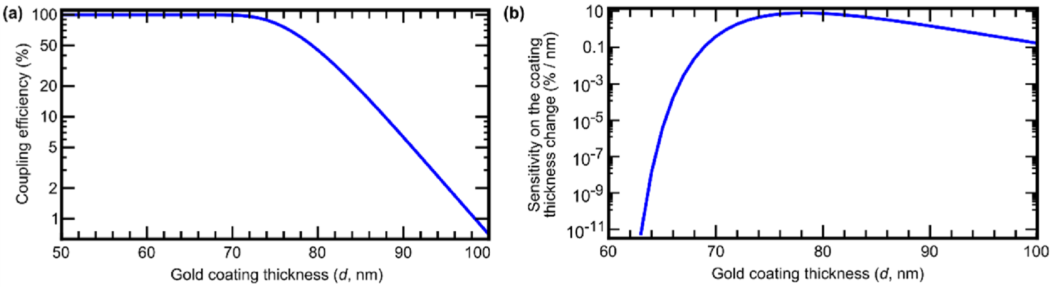

Figure 14 (a) Coupling efficiency of the TM_{01} mode to the $TM_{0Co\text{-}SP}$ mode depending on the gold coating thickness d of the plasmonic tip. We apply a logarithmic scale to the vertical axis to enhance the visibility of the region above the gold coating thickness d of 70 nm where the most dynamic and fast increase of the coupling efficiency occurs. **(b)** Sensitivity to the coating thickness change depending on the coating thickness d. These values are calculated for a taper angle θ of 20° and a surrounding medium with $n_{\mathrm{surr}} = 1$. Below the gold coating thickness d of 70 nm, the coupling efficiency becomes over 98%, but its increment with the decreasing coating thickness d is slow and minor.

interaction (phase matching) between the photonic and plasmonic modes for given parameters of the plasmonic tip. The coupling efficiency is proportional to the increased power of the mode and thus is comparable to the square of the coupling amplitude, which is $A_{\mathrm{Pl}}^2(z_0)$. Since the coupling efficiency is given in percentage, it is given as $A_{\mathrm{Pl}}^2(z_0)\times100\%$. Further details of Equation (15) can be found in Reference 68.

We calculate the coupling efficiency depending on the coating thickness d and show the results in **Figure 14**a. At a gold coating thickness of 50 nm, we obtain a plasmonic mode's coupling efficiency of about 99%. In general, the coupling efficiency becomes higher than 98% below a gold coating thickness of 70 nm so we can say that the coupling efficiency nearly saturates below this coating thickness as can be seen in **Figure 14a**. For a thick coating thickness d (> 75 nm), the coupling efficiency reduces dramatically with faster rate. As we have shown in **Figure 13b** and **Figure 14a**, the coupling efficiency is as small as 0.7% for the coating thickness d of 100 nm. However, this value is still larger than that of the aperture SNOM tips (the light transmission efficiency < 0.0001%) that is discussed in Section 2.4.4. This signifies one of the many advantages of plasmonic tips that is the efficient power conversion from the far-field to near-field compared with other SNOM tips.

In addition to the coupling efficiency depending on the coating thickness d, we can estimate how much the coupling efficiency will change if the coating thickness d changes by 1 nm. We name this parameter plasmonic tip's sensitivity to the coating thickness change, and it is calculated as $\partial A_{\mathrm{Pl}}^2(d)/\partial d\times100\%$. We are interested in this parameter because this number can imply the possibility to change the plasmonic tip's emission not only due to the coating thickness change but also due to the surrounding medium change. Having a low sensitivity to the change of the coating thickness and a large coupling efficiency means that the tip emission can only be altered by an insignificant amount. Hence, we can say plasmonic tips with such parameters are bad candidate for sensing applications.

The sensitivity to the change of the coating thickness is calculated and shown in **Figure 14b** as a function of the coating thickness d. We estimate that the sensitivity to the coating thickness change is 10^{-11}% per nm for a coating thickness d of 60 nm. This means that when the coating thickness d of a plasmonic tip is around 60 ± 1 nm, the coupling efficiency can differ by 10^{-11}%, which is an insignificant amount of change to detect. Thus, despite having a coupling efficiency above 98%, the increase of the coupling efficiency happens slowly and weakly below a coating thickness d of 70 nm as can be seen in both **Figure 14a** and **b**. Above a coating thickness d of 70 nm, however, the increase of the coupling efficiency is dynamic and strong. The sensitivity to the coating thickness change reaches as high as 7.93% per nm at a coating thickness d of 78 nm. Furthermore, the coupling efficiency is about 7.45% that is much smaller than the saturation level of 100%. Hence, we can anticipate that a plasmonic tip with a coating thickness d of $>$ 70 nm is a good candidate for experiments where the tip emission is manipulated by some means, such as by changing the surrounding medium. We will discuss this matter in next section.

We can also increase the coupling efficiency further by reducing the taper angle θ. Although the coupling efficiency increases with the decreasing coating thickness d and the taper angle θ, there can occur parasitic effects such as direct tunneling of light through the metal layer or multiple back and forth coupling of the photonic and plasmonic modes.

2.5.4 Influence of the surrounding medium on the coupling efficiency

For the given tip parameters of the plasmonic tip on page 37, the coupling efficiency of the plasmonic tip can be manipulated by simply changing the surrounding medium. We calculate the coupling efficiency with Equation (15) for different surrounding media and normalize it by the value that is in air. We call this new parameter the coupling enhancement factor. As the name suggests, the coupling enhancement factor shows an increase of the coupling efficiency due to the surrounding medium compared with air. **Figure 15a** shows the calculated coupling enhancement factor versus the surrounding medium's refractive index. For a coating thickness d of 100 nm, the coupling efficiency is estimated to be 0.7% for $n_{\text{surr}} = 1.0$ and 3.89% for $n_{\text{surr}} = 1.3$ so the coupling enhancement factor is estimated to be 5.55× in a medium with $n_{\text{surr}} = 1.3$. It is important to note here that such large enhancement factor is only possible when the coating thickness d is sufficiently large. In the previous

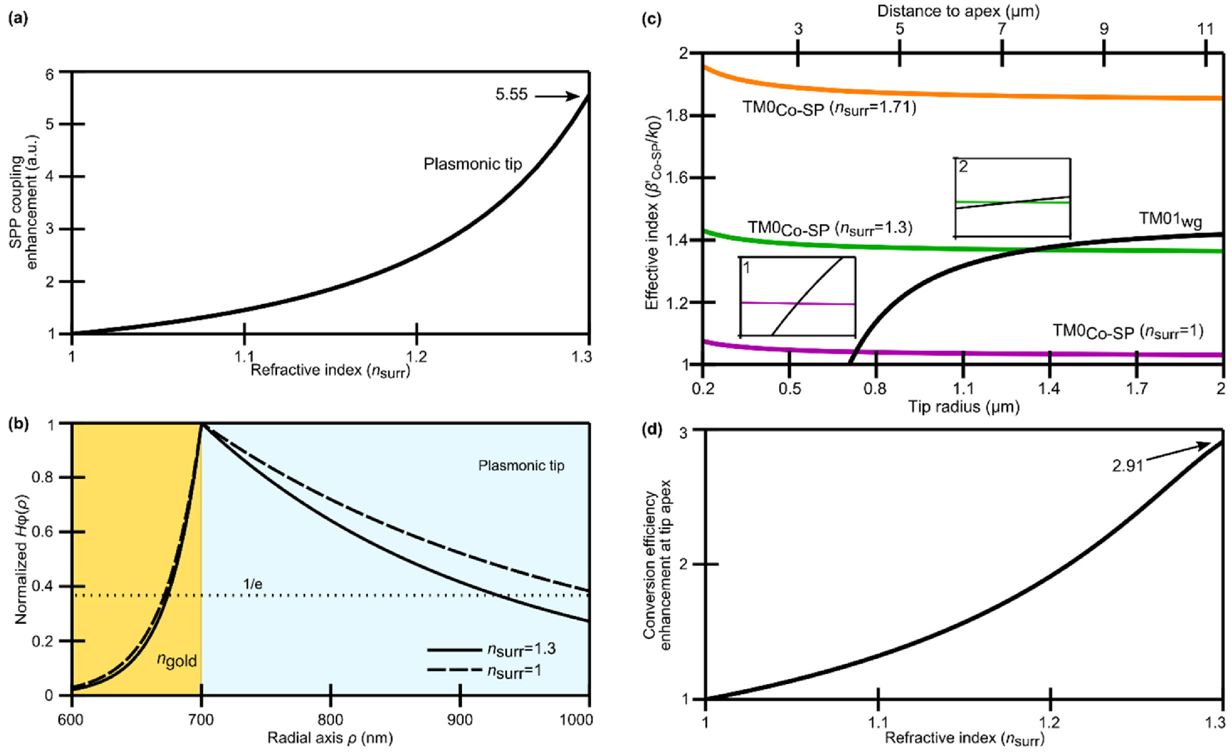

Figure 15. (a) Coupling enhancement factor of plasmonic tips depending on the surrounding medium refractive index n_{surr}. The coupling enhancement factor shows the increase of the coupling efficiency due to the surrounding medium compared with that of the air. The coating thickness d of 100 nm is considered for both cases. **(b)** Transverse magnetic field profile along radial axis in surrounding medium of $n_{surr} = 1.0$ (dashed line) and $n_{surr} = 1.3$ (solid line). **(c)** Real parts of the effective indices of the radially polarized waveguide ($TM_{01,WG}$, black) and plasmonic ($TM_{0Co\text{-}SP}$) modes in surrounding medium of $n_{surr} = 1.0$ (magenta), $n_{surr} = 1.3$ (green), and $n_{surr} = 1.71$ (orange). The insets 1 and 2 shows the close-up of the phase matching regions. **(d)** Conversion efficiency enhancement of a plasmonic tip depending on the refractive index of the surrounding medium. The conversion efficiency is the total power delivered to the plasmonic tip apex from waveguide mode within the tapered fiber at the coupling point. Thus, it includes both the coupling efficiency and the propagation loss from the coupling point to the tip apex. Adapted from Reference 121.

section, we showed that when the coating thickness d is below 70 nm, the coupling efficiency is already 98%, and it only slightly increases with the change of the coating thickness d. Since the coupling efficiency is already close to the saturation level of 100%, and the change is miniscule, there is not much room to increase it further by any measureable amount. Hence, we choose the coating thickness d of 100 nm for which the coupling efficiency is 0.7%. This thick coating thickness allows us to have a high dynamic range in manipulating the coupling enhancement factor with the refractive index of the surrounding medium n_{surr}.

According to Equation (15), the coupling enhancement factor is influenced by two parameters δ and υ, which describe the field overlap integral and the change rate of the effective index difference near the phase-matching region, respectively. We would like to look at each parameter and study its trend depending on the refractive index of the surrounding medium n_{surr}. First, we analyze the influence of the surrounding medium on the field overlap integral. Since the field overlap integral depends on the field's penetration depth, we calculate the transverse magnetic field ($H_{\varphi}(\rho)$) of the plasmonic mode ($\mathrm{TM}_{0\mathrm{Co\text{-}SP}}$) along the radial axis by using Equations (6f) and (7f). The real part of the magnetic field ($Re[H_{\varphi}(\rho)]$) is plotted in **Figure 15b** where the surrounding medium has a refractive index of $n_{\mathrm{surr}} = 1.0$ (solid line) and $n_{\mathrm{surr}} = 1.3$ (dashed line). As shown in the **Figure 15b**, the field's penetration depth in the metal reduces by 2.6 nm when the surrounding medium changes from $n_{\mathrm{surr}} = 1.0$ to $n_{\mathrm{surr}} = 1.3$. Due to this decrease of the field's penetration depth in the metal, the field overlap integral (parameter δ) decreases as well as the coupling efficiency.

Second, we take a look at the dispersion curve of the plasmonic mode in different media to see the influence of the surrounding medium on the rate of change of the effective indices' difference (parameter υ). We calculate the effective indices of the $\mathrm{TM}_{0\mathrm{Co\text{-}SP}}$ mode in a surrounding media with refractive indices of $n_{\mathrm{surr}} = 1.0$ (magenta), $n_{\mathrm{surr}} = 1.3$ (green), and $n_{\mathrm{surr}} = 1.71$ (orange). The results are presented in **Figure 15c** where the insets show the close-ups of the phase-matching regions in a surrounding medium of air and a medium with $n_{\mathrm{surr}} = 1.3$. As the surrounding medium's refractive index increases, the effective index of the plasmonic mode increases, and thus the dispersion curve shifts in the upward direction. Consequently, the phase-matching point moves toward the larger tip radius b where the effective indices depending on the tip radius b changes with a slower rate for both TM_{01} (photonic) and $\mathrm{TM}_{0\mathrm{Co\text{-}SP}}$ (plasmonic) modes. This means that the interaction length extends (smaller parameter υ) with the increasing surrounding medium's refractive index n_{surr} allowing the coupling efficiency to increase in an optically denser medium compared with air.

When the tip is in a denser medium such as $n_{\mathrm{surr}} = 1.3$, the field overlap integral reduces due to the decreased penetration depth (decreasing parameter δ), and the interaction length increases due to the shift of the phase-matching region to a large tip radius b (decreasing parameter υ). The former effect reduces the coupling efficiency, and the later increases the coupling efficiency. Since the later effect is the dominant one, we have an overall gain in the coupling efficiency that is 5.55× for a plasmonic tip with a coating thickness d of 100 nm in a surrounding medium with $n_{\mathrm{surr}} = 1.3$.

When plasmonic tips are used in real experiments, we concern plasmons that reach the tip apex rather than what is directly excited or coupled from the photonic mode. Consequently, we have to obtain the total power conversion efficiency of plasmons by including the propagation loss that occur during the propagation from the coupling point to the tip apex. The next equation considers this case by multiplying the coupling efficiency by the power decay value due to the propagation loss as

$$T(n_{\mathrm{surr}}) \approx {A_{\mathrm{Pl}}}^{2}(n_{\mathrm{surr}}) \exp\left(-2\int_{0}^{\mathrm{z}_0} \beta''_{\mathrm{Pl}}(z, n_{\mathrm{surr}})\mathrm{d}z\right). \quad (16)$$

Here, both the coupling amplitude and the propagation constants are the function of the surrounding medium. We calculate this total conversion efficiency depending on the surrounding medium n_{surr} and present it in **Figure 15d**. The total conversion efficiency in a medium is normalized by the value that is in air to see the enhancement factor. As the figure shows, the total conversion efficiency is enhanced with the increasing refractive index of the surrounding medium. In a medium with $n_{\mathrm{surr}} = 1.3$, we have the total conversion efficiency enhancement of 2.91× compared with air. This trend, however, doesn't continue when the refractive index of the surrounding medium n_{surr} becomes higher. When $n_{\mathrm{surr}} > 1.32$, the propagation loss starts to dominate (see the supplementary material in Reference 121), and the conversion efficiency no longer increases; rather it starts to decrease. Furthermore, when $n_{\mathrm{surr}} > 1.37$, the phase matching condition is no longer fulfilled for our calculation parameters. Just like the medium with $n_{\mathrm{surr}} = 1.71$ in **Figure 15c**, the dispersion curves of the plasmonic and photonic modes don't cross indicating that the plasmonic mode can no longer be excited. Note that these numbers will differ if the parameters are chosen other than $n_{\mathrm{core}} = 1.4474$ and wavelength of $\lambda_0 = 784$ nm.

We conclude that when plasmonic tips are in a medium such as a liquid, the total power reaching the apex can be enhanced, and the field at the apex is further confined to the metal-surrounding medium interface. This suggests there can be an interesting application of plasmonic tips such as optical tweezers or optical nano-manipulators in a liquid environment.

3 Plasmonic tips‘ emission

In the previous chapter, we have studied analytically the modal characteristics of fiber based SNOM tips that are dielectric tips, aperture tips, and plasmonic tips. Performance-wise, we have concluded, based on our analytical study, that the plasmonic tips have the potential to produce far superior results in both optical and topographic resolutions during a SNOM measurement as compared to the dielectric or aperture tips. Prior to use plasmonic tips in investigating unknown samples, we need to examine their behavior experimentally so that we will be able to interpret correctly the SNOM images. Since the dielectric or aperture tips have been around for more than 30 years,[20,78,80,81,84,122,123] their emission and detection characteristics are rather well documented as compared to the plasmonic tip that has become available only recently. For this reason, we will concentrate on the plasmonic tip in this and the next chapters and study experimentally its emission and detection characteristics in both near- and far-fields. Despite many analytical[68,124–126] and numerical[118,127,128] studies and some attempts in fabricating different types of plasmonic tips,[64,129] fiber based plasmonic tips weren’t available in its true form for experimental study. This is because there was no fiber that could guide the radially polarized beam over a long distance without major disturbance in mode’s polarization state. With the emergence of the vortex fiber that is designed to guide securely the cylindrical vector beams including the radially polarized beam over a long distance,[72,73] we were able to produce plasmonic tips and study their emission and detection characteristics. In this chapter, we explore the far- and near-field emission characteristics of the plasmonic tip that is made by tapering a vortex fiber and then gold coating it with a physical deposition method. We will briefly explain the vortex fiber, the fabrication process of plasmonic tips, and the generation of the radially polarized beam in Section 3.1. In Section 3.2 , we discuss the radially polarized modes in different parts of the plasmonic tip that are in the vortex fiber, in the tapered vortex fiber, and also on the outer gold surface of the plasmonic tip as a plasmonic mode. As we have discussed in Section 2.5.4, the surrounding medium affects the coupling efficiency and also the tip’s emission. We will study this effect by probing the far-field emission of a plasmonic tip in different liquids in Section 3.3 . Furthermore, the plasmonic tip’s near-field emission is studied by using a bull’s eye grating which is discussed in Section 3.4 .

3.1 Fabrication of plasmonic tips and generation of the radially polarized beam

Before start analyzing the plasmonic tip’s emission, we discuss essential preparation steps that are fabricating the plasmonic tip, generating a radially polarized beam, and coupling the beam into the vortex fiber of the plasmonic tip.

Vortex fiber and its tapering. The plasmonic tip is a tapered and fully metal coated vortex fiber that is also called ring-core fiber, orbital angular momentum (OAM) fiber, or M-profile fiber.[72,73] The facet of the vortex fiber with a cladding diameter of 115 µm is imaged with a microscope objective and shown in **Figure 16a**. As the figure shows, the vortex fiber has double ring core structures and is specially designed to guide the cylindrical vector beams including the radially polarized mode over a long distance with a high modal purity.[72,73] This fiber is designed that at a wavelength of about 1500 nm, the outer ring core guides the cylindrically vector modes while the inner core guides the fundamental Gaussian-like fiber mode. The fundamental mode can be transformed into a radially polarized mode by using a long period grating that applies mechanical pressure to intercouple these modes.[72]

We measure the refractive index profile of the vortex fiber with a fiber index profiler (IFA-100, Interfiber Analysis) at wavelengths of 522, 594, 666, 739, and 811 nm. To obtain the refractive index profile of the core at our laser’s operating wavelength of 784 nm, we perform linear fitting by using these five measurements. **Figure 16b** presents the linear fitted refractive index profile of the vortex fiber core. The cladding and core refractive indices range from 1.4474 to 1.4984 at a wavelength of 784 nm. For analytically calculating the waveguide modes in the dielectric core of the plasmonic tip, we assume that the refractive index of the tip core is 1.4474 as same as the cladding refractive index of the vortex fiber (see Section 2.4.6). This is a valid assumption since the cladding to core diameter ratio is conserved during the tapering process as we will show in the next section. Toward the tip apex, the core of the vortex fiber, therefore, shrinks so the core not only comprises the minor part of the plasmonic tip’s core but also no longer guides the waveguide mode in the plasmonic tip. As it can be seen in **Figure 16b**, the inner ring core has a narrow and shallow refractive index modulation so one

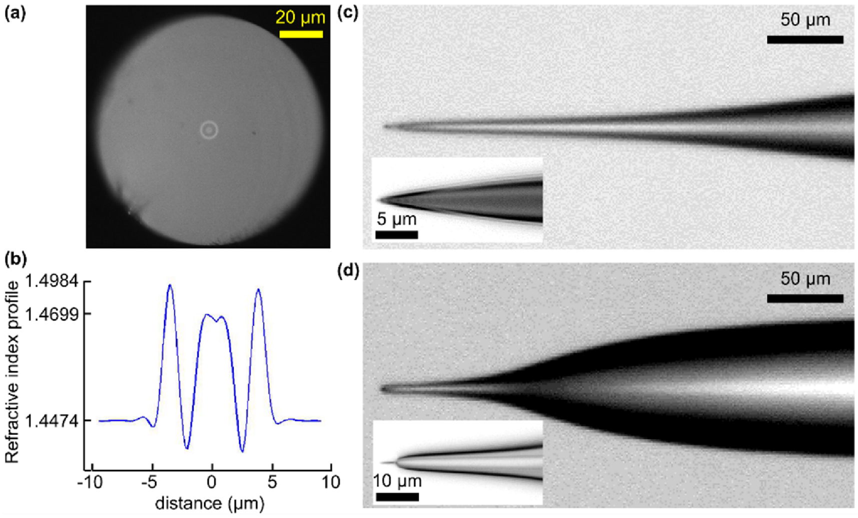

Figure 16. (a) Facet image of a vortex fiber with a cladding diameter of 115 µm. **(b)** Refractive index profile of the vortex fiber’s core at a wavelength of 784 nm. The refractive index profile was measured at 5 different wavelengths and linear fitted to find the one at a wavelength of 784 nm. **(c)** Microscope image of a smoothly tapered vortex fiber. The inset shows the close-up of the apex region. **(d)** Microscope image of a bottle-neck shaped tapered vortex fiber that is produced with multiple phases of heating and pulling steps. The inset shows the close-up of the apex region. The figure shows that the bottle-neck shape repeats itself near the apex region.

might not see it as a ring core in the microscope image in **Figure 16a**. This shallow refractive index modulation in the inner ring core is designed such on purpose to guide both the radially polarized mode and the fundamental Gaussian-like mode. At a wavelength lower than the fiber’s designed wavelength of 1500 nm, this inner core guides the higher order radially polarized modes.[130] In Reference 130, the supported modes of the vortex fiber have been calculated by using COMSOL software for the refractive index profile given in **Figure 16b** and at a wavelength of 784 nm. We will also demonstrate this in the next section when discussing about the radially polarized mode’s evolution in the plasmonic tip.

Next, we taper the vortex fiber by using a laser based micropipette puller (P-2000/F, Sutter Instrument). The machine employs the heating and pulling technique where a CO_2 laser of 10 W is focused onto the fiber while two ends of the fiber are fixed on two separate stages that pull the fiber in two opposite directions.[81,131] When the laser melts the fiber, the pulling force separates the fiber into two pieces of tapered fiber creating two identical tapered tips with apex sizes of about 30 nm.[82] An example of a smoothly tapered fiber is imaged with a microscope and shown in **Figure 16c** where the inset shows the close-up of the apex region. The taper angle (full cone angle) is about 18° near the tip apex, yet away from the tip apex, it reduces and becomes below 5°. For smoothly tapered tips, the taper length is thus long about 0.5 – 1.0 mm from the tip part with a diameter of 50 µm to the tip apex. An

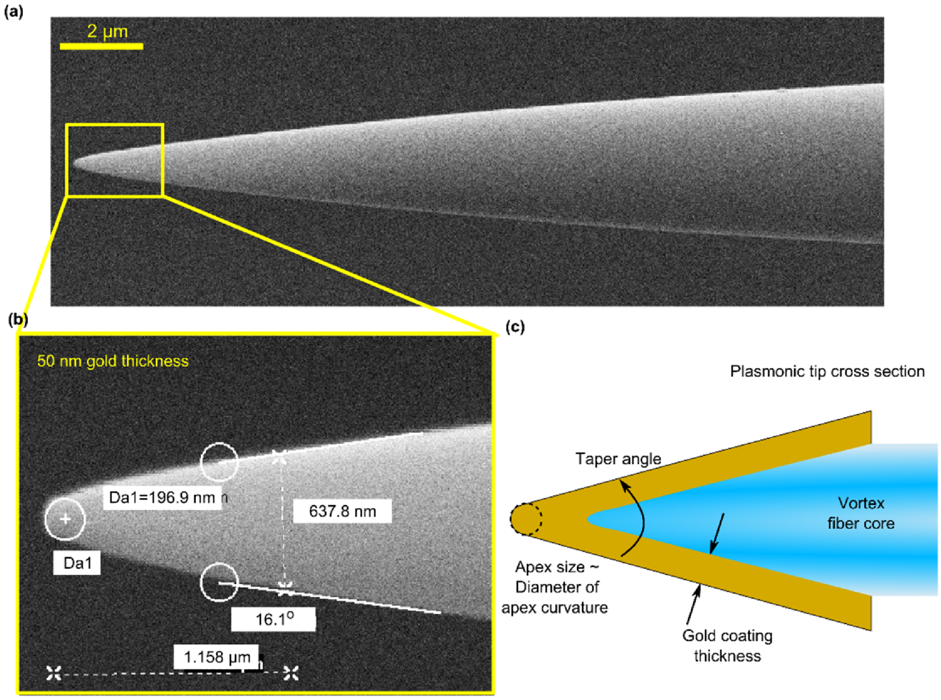

Figure 17. (a) Scanning electron microscope (SEM) image of a typical plasmonic tip. **(b)** Close-up image of the plasmonic tip’s apex region. It is shown that for 50 nm gold thickness, the plasmonic tip’s apex size is about 200 nm. The taper angle of the plasmonic tip is about 16° in the resonant coupling region; however, this taper angle varies along the tip axis. **(c)** Illustration of a plasmonic tip’s cross-section. There are several characteristic parameters of the plasmonic tip that are the apex size, the coating thickness, and the taper angle. These parameters determine the performance of the plasmonic tip in SNOM measurements.

advantage of such taper shape is adiabaticity of a mode propagation in the tapered waveguide. During the tapering, one can use multiple phases of melting and pulling to produce a bottle-neck shaped tip[131] that has a shorter tapered region and a larger taper angle than the smoothly tapered tip. An example of a bottle-neck shaped tip is imaged with a microscope objective and shown in **Figure 16d** where the inset shows the close-up of the apex region. The figures show that the bottle-neck shape repeats itself near the tip apex. The taper angle is about 30° in the first bottle-neck section at a diameter of 50 µm and about 40° in the second bottle-neck section at a diameter of 3 µm. For the tip shown in the **Figure 16d**, the taper length is about 150 µm from the tip part with a diameter of 50 µm to the tip. Due to the less reproducibility in fabricating the bottle-neck shaped tips, the taper length usually ranges in between 0.1 – 0.4 mm. The larger the taper angle is, the smaller the propagation loss is since the taper length or the distance for the mode to propagate is short. Such large taper angle and short taper length is advantageous for aperture tips since they have low transmission efficiency of about 10^{-8} due to the propagation loss (see sections 2.4.3 and 2.4.4). However, it is not the case for plasmonic tips. The short taper length and large taper angle results in non-adiabatic mode propagation that causes a coupling between modes that are propagating forward and backward (back-reflection) directions and an excitation of higher order modes. The polarization state also can be disturbed due to the non-adiabatic mode propagation. Thus, it is preferred to have smoother and adiabatic tapering, like the one in **Figure 16c**, for plasmonic tips. However, to accurately determine the optimal taper angle, we should study experimentally the guided modes in the tapered fiber when a specific mode is excited at the fiber end of the tip by using modal decomposition methods[132–136].

Metal coating of plasmonic tips. The tapered fibers are then gold coated with a physical evaporation deposition method by using a custom made evaporation and deposition chamber. **Figure 17a** shows a typical scanning electron microscope (SEM) image of a plasmonic tip. Although the physical evaporation deposition method usually results in a polycrystalline gold layer with grain/cluster sizes of about 50 nm, the SEM image shows that the coating layer is homogenous and free of major defects. Thus, it is expected that the small clusters will not disturb much the plasmonic mode’s propagation. The apex region, marked with a yellow box in **Figure 17a**, is enlarged and presented in **Figure 17b**. The coating thickness, the coating material, the taper angle, and the tip apex are important parameters since they determine the performance of the SNOM measurement. These parameters are explained and illustrated **Figure 17c**. In each upcoming discussion on experimental results, we will provide these parameters.

In **Figure 17a** and **b**, we obtain a plasmonic tip with an apex size of about 200 nm when the coating thickness is about 50 nm. The apex size increases with the coating thickness increase, and thus to obtain a small tip apex, an additional sharpening step is required such as a wet chemical etching[137,138] or a dry etching with plasma, ion or gases.[139–143] The tip apex is round and smooth as it can be seen in **Figure 17a** and **b**, and this shape is important for plasmonic tip’s detection characteristics. The taper angle is about 16^o in the resonant coupling region where the tip diameter is about 1.5 μm.

Generating and coupling of the radially polarized beam. Besides fabricating a good plasmonic tip, it is crucial to generate the radially polarized beam and excite only the TM_{01} fiber mode in the vortex fiber of the plasmonic tip by using this free space radially polarized mode. **Figure 18** illustrates the experimental setup for generating a radially polarized beam and coupling the beam into the plasmonic tip. We first convert the linearly polarized Gaussian beam into a radially polarized beam by using a radial polarization converter (Arcoptix) that is made of a liquid crystal. We include the intensity profiles of the free space Gaussian beam and the converted radially polarized beams in **Figure 18** where the blue arrows indicate the polarization state. The radially polarized beam is then coupled into

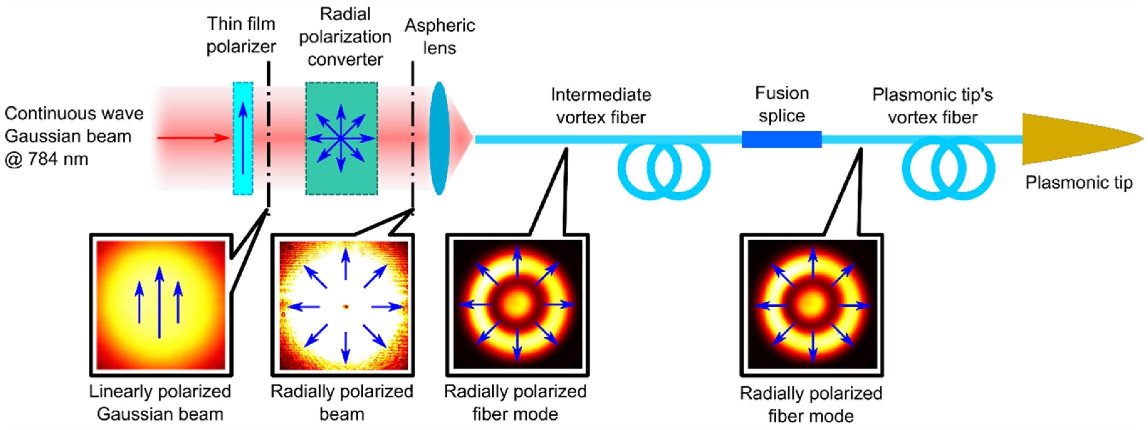

Figure 18. Experimental setup for generating a radially polarized beam and coupling the beam into the vortex fiber of the plasmonic tip. A radial polarization converter changes the linearly polarized Gaussian beam into a radially polarized beam by using liquid crystal cells that locally reorient the Gaussian beam field vector. The radially polarized beam is then coupled into an intermediate vortex fiber with an aspheric lens. To make sure the fiber mode is radially polarized, we align the vortex fiber and monitor the fiber mode. This part of the setup is not shown here. After exciting the radially polarized fiber mode in the vortex fiber, we splice the intermediate vortex fiber with the vortex fiber of the plasmonic tip. The blue arrows show the polarization state of the beams and the fiber modes.

an intermediate separate piece of vortex fiber by using an aspheric lens with a numerical aperture of 0.16 (C260–TMD–B, Thorlabs). Although it is not shown in the figure, one end of the intermediate vortex fiber, the one near the aspheric lens, is fixed on a xyz-translation stage, and the transmission from the other fiber end is monitored with a charge coupled device (CCD) camera. We align the fiber with respect to the aspheric lens until the radially polarized fiber mode is excited in the vortex fiber. After insuring the mode in the intermediate vortex fiber is radially polarized with a thin film polarization analyzer (hereafter called polarization analyzer), we splice the intermediate vortex fiber with the vortex fiber of the plasmonic tip by using an arc fusion splicer (FSM-45PM-LDF, Fujikura). This procedure insures that the mode in the fiber of the plasmonic tip is also radially polarized and thus offers us the best chance to deliver the radially polarized mode to the tapered section of the plasmonic tip. In a separate experiment that is not presented here, we have investigated the fusion splicing parameters that produce a good junction between the fibers through which the radially polarized fiber mode propagates without significant disturbance. Radially polarized fiber modes in the vortex fibers are also included as insets where the blue arrows indicate the polarization state. As it can be seen in the image of the vortex fiber mode **Figure 18**, both ring cores guides light meaning that both TM_{01} (guided in the outer core) and TM_{02} (guided in the inner core) modes are excited in the vortex fiber.[130] This is due to our simple excitation setup. The radial polarization converter only offers a phase change, yet there still exists the amplitude mismatch between the fiber mode and the input beam. This amplitude mismatch often causes an excitation of higher order radially polarized modes.[130] A computer generated hologram or an annular amplitude mask can be added to obtain a better shaped radially polarized beam that is both phase and amplitude matched with that of the fiber mode.[130] Such experiment has been performed and demonstrated that the TM_{01} mode can be selectively excited in the vortex fiber.[130]

3.2 Propagation of the radially polarized mode through the plasmonic tip

Starting from the vortex fiber of the plasmonic tip, we would like to analyze the modes in the different regions of the plasmonic tip when a radially polarized beam is coupled into the vortex fiber of the tip. We use tips that have coating thicknesses of about 90 nm and apex sizes of about 200 nm. First, we concern the modes in the vortex fiber when a radially polarized beam at a free space wavelength of 784 nm is coupled into the fiber. To compare with the guided mode in the vortex fiber, we present the microscope image of the vortex fiber facet showing the double ring core in **Figure 19a**. The outer ring core has a diameter of 9 µm for the vortex fiber when the cladding diameter is 115 µm.[69,72] Now, we couple the radially polarized beam into the vortex fiber and image the guided modes in the vortex fiber when the microscope objective is still focused on the fiber facet. **Figure 19b** shows the intensity images of the guided mode profiles in the vortex fiber. Polarization resolved images are also shown in **Figure 19b** where the yellow arrows indicate the polarization analyzer’s transmission axis. When the analyzer is rotated, the two lobes in the inner and outer ring cores rotate with the polarization analyzer in the same direction. Furthermore, the lobes are oriented along the transmission axis in each cases, and thus we conclude that the mode in the vortex fiber is radially polarized. The figure also shows that both ring cores guide light where it is stronger in the outer core and weaker in the inner core. At our laser operation wavelength of 784 nm, the lowest order radially polarized mode, TM_{01}, of the vortex fiber is guided in the outer core while the next higher order radially polarized mode, TM_{02}, is in the inner core.[130] Consequently, the image confirms that with our simple excitation setup, we excite not only the TM_{01} mode but also the TM_{02} mode. Note that the portion of the TM_{02} mode is much smaller than the TM_{01} mode so we expect the influence of the TM_{02} mode is minor. To avoid exciting the TM_{02} mode, we must improve our excitation setup and match both the amplitude and phase of the incident beam with that of the TM_{01} mode. This matter is thoroughly studied and discussed in Reference 130. Another way to avoid the excitation of the TM$_{02}$ mode is to increase the operation wavelength closer to the vortex fibers’ designed wavelength of about 1500 nm.[72,73] Due to our operation wavelength of 784 nm that is about half of the designed wavelength, the vortex fiber becomes a few mode fiber at our operating wavelength. Although our operating wavelength enables these higher order modes in the fiber, there are some advantages. At shorter wavelengths, the shrinking core structure due to the tapering remains effective in guiding the radially polarize modes closer to the apex than at longer wavelengths. Thus, the shorter wavelength helps to preserve the radially polarized mode in the taper and excite successfully the radially polarized plasmonic mode. Besides, it is not yet clear that how the TM$_{02}$ mode will affect the performance of the plasmonic tip. Depending on the phase difference between the TM$_{01}$ and TM$_{02}$ modes, the existence of the TM$_{02}$ mode might do

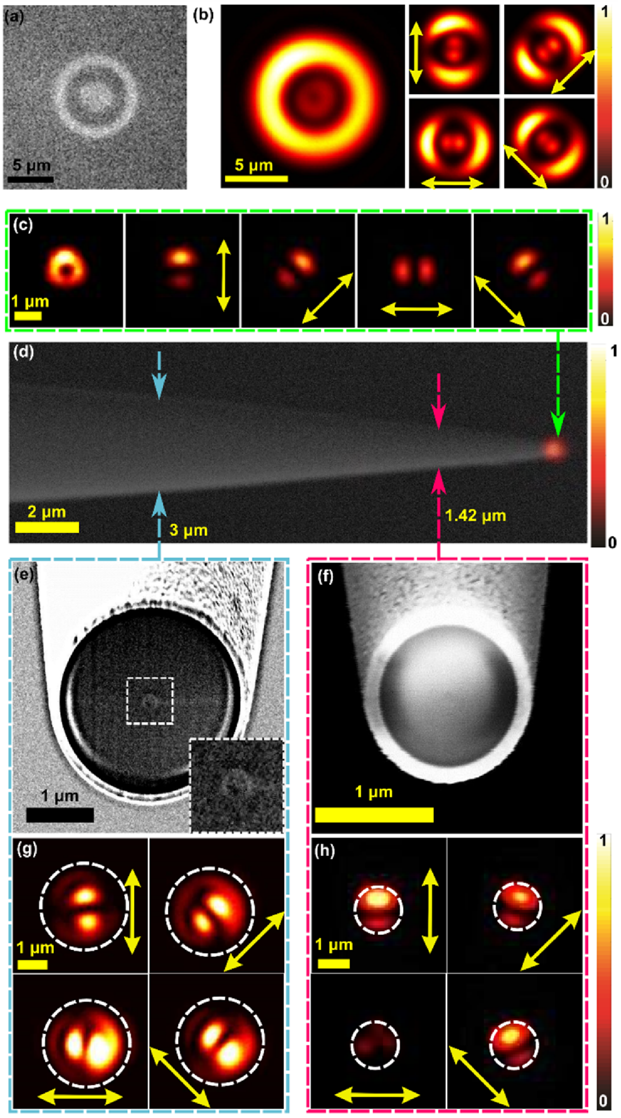

Figure 19. **(a)** Vortex fiber facet. The fiber has double ring core structures, and the outer ring diameter is 9 µm for a fiber for the vortex fiber with a cladding diameter of 115 µm. **(b)** Guided mode within the vortex fiber when a radially polarized beam is coupled into the fiber. **(c)** Plasmonic tip’s emission to the front. **(d)** Plasmonic tip’s emission to the side overlaid with the tip’s scanning electron microscope (SEM) image. **(e)** SEM image of a cross-sectioned plasmonic tip at a diameter of 3.0 µm. **(f)** SEM image of a cross-sectioned plasmonic tip at a diameter of 1.42 µm. **(g)** Guided mode within the cross-sectioned plasmonic tip with a diameter of 3.0 µm. **(h)** Guided mode within the cross-sectioned plasmonic tip with a diameter of 3.0 µm. Yellow arrows in (b-c) and (g-h) indicate the transmission axis of a thin film polarization analyzer. Adapted from Reference 121.

good or bad. Based on **Figure 19b** that shows the intensity of the TM_{02} mode is weaker than that of the TM_{01} mode, however, we can claim that the influence of the TM_{02} mode will be negligible.

The radially polarized mode within the fiber, then, propagates to the tapered part of the plasmonic tip and excites the radially polarized plasmons on the outer surface of the gold coating. The plasmonic mode propagates to the apex and emits to the front and the side directions. We image the tip emission to the front and side with a microscope objective (LD EC Epiplan-Neofluar 100x 0.75NA, Zeiss) and present them in **Figure 19c** and **d**, respectively. The focal plane of the objective was carefully aligned on the plane of the tip apex for imaging the tip's front emission and on the plane of tip's side surface for imaging the tip's side emission. In **Figure 19c**, the tip's front emission image shows that the front emission has a doughnut shape while the polarization resolved images show that the excited plasmons are radially polarized. Since only the fundamental plasmonic mode, $TM_{0Co\text{-}SP}$, is radially polarized, we conclude that this fundamental superfocusing mode is successfully excited. In **Figure 19d**, we show the tip emission to the side overlaid with the tip's SEM image. The figure shows that the plasmonic tip emits from its apex to the side. When the $TM_{0Co\text{-}SP}$ mode propagates toward the plasmonic tip apex, the longitudinal field increases as we have shown in Section 2.5.1. At the tip apex, the plasmons will constructively interfere creating a strong longitudinal field.[67] This longitudinally oscillating field is similar to a longitudinally oscillating dipole along the tip axis, and thus the field will be emitted to the side. The smaller the tip apex is, the stronger the longitudinal field becomes at the apex so does the tip emission to the side. For this particular plasmonic tip, the apex size was about 200 nm; thus, the tip emits not only to the side but also to the front. We expect that the tip emission to the side will increase with the decreasing tip apex size while the emission to the front will decrease.[60,61]

We also take a look at the mode profiles in the tapered region of the plasmonic tips. We cross-section two similar plasmonic tips at diameters of 3.0 μm and 1.42 μm and study the cross-sectioned tips' facets and the profiles of the guided mode within them. The SEM images of the cross-section tips' facets are shown in **Figure 19e** and **f**. When **Figure 19e** (taper diameter of 3 μm) is carefully observed, one can see a faint ring core structure of the vortex fiber that has shrunk from 9 μm down to 200 nm. This can be clearly seen in the inset in **Figure 19e** where the dashed part of the core has been enlarged for better visibility. If we calculate the core to cladding ratios in **Figure 19a** and **e**, they are 12.8 in the fiber (115 μm to 9 μm) and 13.4 in the tapered fiber (≈ 2.68 μm to ≈ 0.2 μm). From this, we can conclude that the heating and pulling technique scales down linearly the core to cladding ratio and preserves the core structure until the very end. This linear and slow transformation of the core helps to preserve the polarization state of the guided mode over a long distance in the tapered region. We can see this in **Figure 19g** and **h** where we show the intensity images of the guided mode at tapered regions with diameters of 3.0 µm and 1.42 µm, respectively. We couple a radially polarized mode into the fiber end of the cross-sectioned fiber tip and image the intensity profiles while having the focal plane of the imaging objective at the facet of the cross-sectioned tip. **Figure 19g** reveals that the intensity profiles contain faint lobes besides the main central lobes. This means that there exists the TM_{02} mode besides the desired TM_{01} mode. This higher order mode exists due to our chosen wavelength of 784 nm as we have mentioned earlier in this section. After the tip diameter of about 3.0 µm, the TM_{02} mode experiences cutoff. Thus, on **Figure 19h**, we only see two lobes meaning that only TM_{01} mode exists at a tip diameter of 1.42 µm. With **Figure 19e-h**, we can deduce that the core structure shrinks monotonously toward the tip apex allowing the guided modes to transform adiabatically and reach safely to the resonant coupling region of the plasmonic tip.

3.3 Plasmonic tips’ emission in liquid environments

As we have discussed in Section 2.5.4, the surrounding medium affects the plasmonic tip’s excitation process and the tip’s emission. Due to the increase of the surrounding medium’s refractive index, the phase matching region shifts to the region where the tip radius is larger. Due to this shift, the interaction region between the plasmonic mode and the fiber mode becomes longer; consequently, the coupling efficiency increases. Furthermore, the penetration depth of the plasmonic mode’s field reduces slightly in the metal so does the coupling efficiency. Since the first effect, the increase of the interaction length, is dominant as we have shown in Section 2.5.4, the overall coupling coefficient increases.

We would like to experimentally study this environmental effect on the plasmonic tip’s emission. To do so, we immerse a plasmonic tip in different liquids and probe its emission while moving the liquid in a cuvette. The experimental setup is illustrated in **Figure 20a**. We make a small hole on the bottom of a glass cuvette and fill it with liquids. The measurements are performed separately for two different liquids with refractive indices of $n = 1.3$ and $n = 1.71$. The plasmonic tip goes through the hole in the cuvette, and its position is fixed with respect to the imaging objective while leaving the last ≈ 50 µm of the tip exposed in air without the liquid covering it. The cuvette with liquid is attached to a piezo

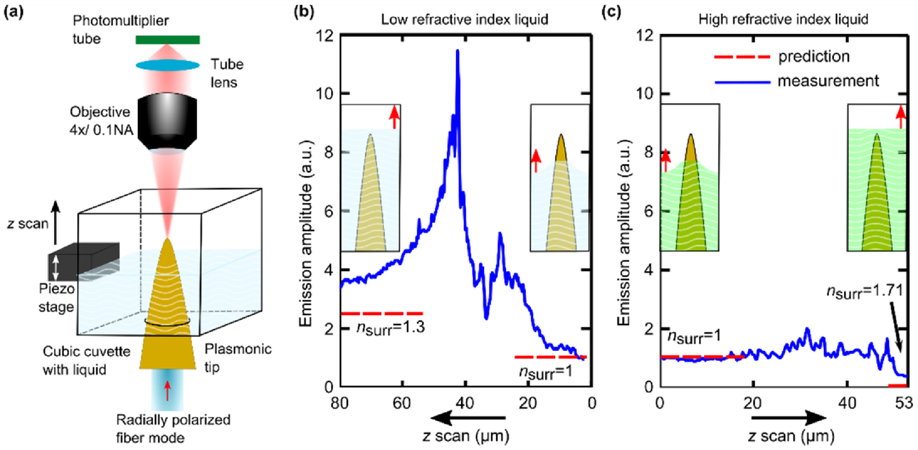

Figure 20. (a) Experimental setup for probing the tip emission while moving the liquid in a cuvette in upward direction. **(b)** Plasmonic tip emission probed in a liquid with $n = 1.3$ **(c)** Plasmonic tip emission probed in a liquid with $n = 1.71$. In (b-c), the insets show the relative position of the liquid surface with respect to the plasmonic tip's apex while the red arrows indicate the liquid surface movement direction. Meanwhile, the black arrows in the bottom z axis shows the scan direction. Red dashed lines show the theoretically estimated values in respective surrounding medium. Adapted from Reference 121.

stage and moves up starting from $z = 0$ µm (tip in air) and ending at $z = 80$ µm (tip in a liquid) where the tip is completely covered by liquid. About ≈ 30 µm of liquid layer forms in between the tip apex and the liquid surface when the stage reaches its maximum height. Since we use an objective (Plan N 4× 0.1NA, Olympus) with a depth of focus of 15 µm, this amount of liquid layer doesn't shift the tip apex out of the focal volume. While the cuvette shifts from $z = 0$ µm to $z = 80$ µm, we measure the tip's emission with a photomultiplier tube (PMT). The measurement, thus, shows the tip's emission change with respect to the amount of distance in which the liquid in a cuvette is moved in upward direction. In this experiment, we use a plasmonic tip with a coating thickness of about 100 nm and a radially polarized beam as an excitation source for the plasmonic tip.

First, we put the tip in a liquid with a refractive index of $n = 1.3$ and measure the tip's emission while moving the cuvette with a liquid in upward direction. The experiment result is shown in **Figure 20b** where the raw data is normalized so that the tip's emission in air is unity. The cuvette's movement direction is indicated with a black arrow on the bottom of the graph. The insets in **Figure 20b** and **c** also show the relative position of the liquid surface with respect to the tip apex, and the red arrows indicate the liquid surface's movement direction. The graph shows that the tip's emission increases about 3.5× in the liquid with $n = 1.3$ compared with air. This increase of emission clearly indicates that the coupling efficiency of the plasmonic tip has increased in this liquid environment as we have anticipated in Section 2.5.4. According to the calculation, we expected that the emission will increase about 2.91× that is indicated with a red dashed line in **Figure 20b**. This difference in the measurement and calculation is likely to be caused by the increased scattering of plasmons in a liquid compared with air. The total coupling efficiency increases by 5.5× as shown in **Figure 15a**, but due to the propagation loss, only some reaches the apex giving a total enhancement of 2.91× at the apex. In a liquid environment, however, plasmons will scatter so we not only measure the tip emission from the apex but also the scattered plasmons.

Next, we change the cuvette with a new one and fill it with a liquid with a refractive index of $n = 1.71$ in the new cuvette. Before repeating the measurement with the same tip, we clean the tip carefully with isopropanol droplets to remove the residue of the previous liquid. Afterwards, we repeat the measurement and show the result in **Figure 20c** where the graph is also normalized so that the tip’s emission in air is unity. Like before, the liquid surface’s movement is indicated in the insets with red and black arrows. Unlike the previous case (a liquid with a refractive index of $n = 1.3$), there is no sharp peaks and increase of emission. The emission rather decreases as the tip fully enters the liquid and reaches the value of 0.4. This sharp decrease of emission indicates that the plasmon excitation is suppressed in the liquid with a refractive index of $n = 1.71$. Theoretically, we expect the emission will be 0 as indicated with a red dashed line on the right side of **Figure 20c** since the phase matching condition is no longer fulfilled in this environment (see the orange curve in **Figure 15c**). However, due to the gold etching caused by increasing plasmon induced heat that enhances the chemical erosion of the surface by the liquid, the gold layer of the tip becomes thinner allowing the light to tunnel through. Thus, we observe some residue emission. This is also the reason why we stop the measurement when stage reaches $z = 53$ µm.

Besides the overall increase of the tip’s emission in a liquid with a refractive index of $n = 1.3$, there appear two sharp peaks at $z = 27.8$ µm and 41.6 µm in **Figure 20b**. Such peaks are usually a sign of some type of resonant effect. Besides the resonant coupling between the radially polarized waveguide (in the fiber core) and plasmonic (at the outer metal-surrounding medium interface) modes, there also can happen (1) a resonant excitation of higher order plasmonic modes or (2) a resonant coupling between the waveguide mode in the fiber core and the waveguide mode in temporarily formed tapered liquid-layer over the tip due to the wetting effect. We showed in the previous section that the waveguide modes in the tapered part the plasmonic tip is radially polarized and composed of TM_{01} and TM_{02} modes. These radially polarized modes are only non-orthogonal to the fundamental plasmonic mode and thus cannot excite the higher order plasmonic modes due to the mode non-orthogonality. Consequently, the resonant excitation of the higher order plasmonic modes is not possible and cannot be the origin of the peaks we observed in **Figure 20b**. The remaining possibility is the resonant coupling between the waveguide mode in the plasmonic tip core and the waveguide mode in a tapered liquid-layer that is formed over the tip. This resonant coupling process is illustrated in **Figure 21a**. The wetting of the plasmonic tip is effective when the tip apex is closer to the liquid surface, and thus the peaks appear shortly before the tip apex submerges under the liquid surface. Furthermore, if one compares the graphs in **Figure 20b** and **c**, the liquid with the refractive indices of $n = 1.3$ seems to provide a favorable condition for the formation of a tapered liquid-layer. To understand this difference, we explore the two liquids and their interaction with a gold surface.

To study this wetting effect, we put two droplets of liquids with refractive indices of $n = 1.3$ and $n = 1.71$ on a gold planar surface and measure the contact angle by imaging the droplets from side with a microscope objective. **Figure 21b** illustrates the definition of the contact angle that is the angle between the gold surface and the tangent to the droplet surface. The stronger the wetting effect is, the smaller the contact angle will be. We image the liquid droplets on a planar gold surface from side with a microscope objectives, and present the results in **Figure 21c** and **d**. For the liquid with a refractive

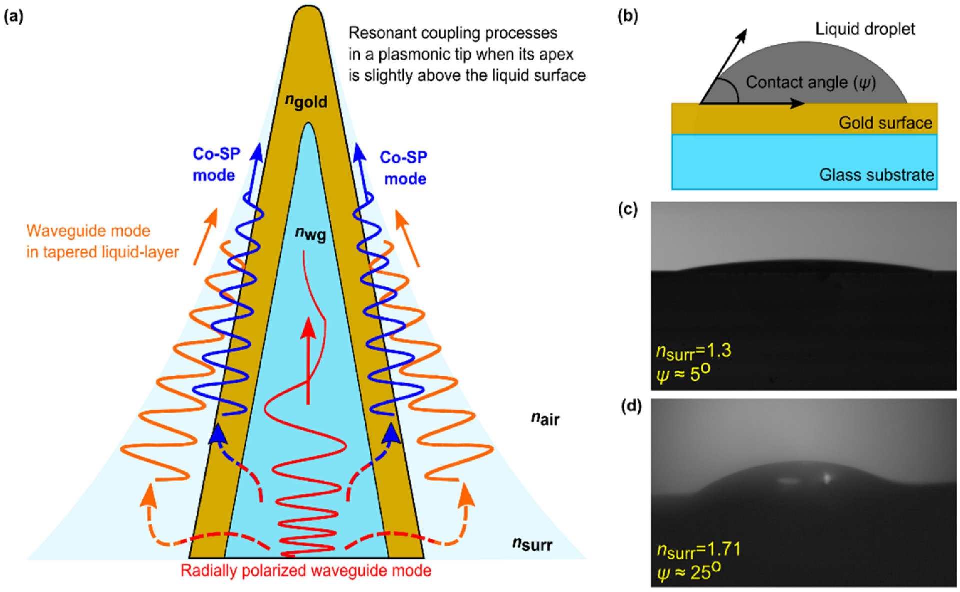

Figure 21. (a) Resonant coupling processes between the waveguide modes in the tip core and the temporarily formed tapered liquid-layer. When the tip apex is above but close to the liquid surface, there can form a tapered liquid-layer over the plasmonic tip surface due to the wetting effect. Thus, besides the resonant coupling between the radially polarized waveguide and plasmonic modes, there also occurs a resonant coupling between the waveguide modes in the fiber core and the tapered liquid-layer. **(b)** Contact angle formed between the gold surface and the tangent to the liquid droplet surface. **(c)** Microscope image of a droplet of a liquid with $n = 1.3$. The contact angle is measured as 5°. **(d)** Microscope image of a droplet of a liquid with $n = 1.71$. The contact angle is measured as 25°. Adapted from Reference 121.

index of $n = 1.3$, the contact angle is 5° so the droplet is almost invisible and indistinguishable from the gold surface. Meanwhile, the contact angle is 25° for the liquid with a refractive index of $n = 1.71$. It is, thus, clear that the liquid with a refractive index of $n = 1.3$ has a stronger wetting effect than the one with $n = 1.71$. Consequently, the liquid with $n = 1.3$ forms effectively a thin tapered liquid-layer over the plasmonic tip that can act like a temporary dielectric tapered waveguide. During the transition of the liquid surface, a right thickness of liquid layer can be formed at the right place of the plasmonic tip so the phase matching condition is satisfied between the waveguide modes in the fiber core and the tapered liquid-layer. In this case, there can occur a resonant coupling between the waveguide modes increasing the total emission of the tip far greater than the anticipated amount in Section 2.5.4. The two peaks in **Figure 20b** can be attributed to the resonant out-coupling of the TM_{01} and TM_{02} modes. Since the wetting effect is weak in the liquid with refractive index of $n = 1.71$, the measurement in **Figure 20c** is free of strong peaks and dips.

3.4 The plasmonic tip’s apex near-field

In this section, we want to measure and study the near-field of the plasmonic tip apex. For accessing the apex near-field, one has to have an evanescent coupling scheme from the tip apex to some other scattering or detecting sample. One can use quantum dots, fluorescent beads, or nanoparticles as scattering centers to scatter and detect the apex near-field in the far-field.[22] Another plasmonic tip can also be used as a detector and measure the apex near-field of a plasmonic tip under study. Though it is challenging, such tip over tip scanning experiment has been done before.[64,144] Above mentioned methods offer direct measurement of the apex near-field by raster scanning the tip over the sample to form the image of the tip’s near-field. However, we avoid such methods because of the uncertainty of the experimental condition. The plasmonic tip’s detection and excitation characteristics are unknown, and it is also difficult to predict the interaction between the plasmonic tip and a sample that can be a nanoparticle or another tip. Instead, we use an indirect yet predicable way for measuring the tip’s near-field where one snapshot can give the whole picture of the apex near-field. In the experiment, a plasmonic tip is placed on a planar gold surface to excite planar SPPs by the tip apex on the gold surface. By analyzing these excited planar SPPs, we can indirectly gain information on the shape and polarization of the tip’s near-field. Since the excitation of SPPs on a planar gold surface is analytically solvable and rather straightforward, this method offers greater simplicity in experimental demonstration and interpretation.

Experimental setup. Our experimental setup is illustrated in **Figure 22a**. The plasmonic tip is glued on a tuning fork and attached to a SNOM head for scanning and positioning purposes. The NT-MDT NTEGRA controller connects the SNOM head with a computer and thus allows us to raster scan the tip over the sample in a shear force mode for obtaining a topographic image of the sample. The sample, used in the experiment, is a bull’s eye grating that consist of a circular disk (9 µm in diameter) and an annular grating with a period of 768 nm (equal to the wavelength of the planar SPPs). The disk and the annular gratings are concentric. To fabricate bull’s eye grating, a gold layer of 100 nm is deposited on a quartz substrate, and then, the grating grooves are milled with a FIB through the gold layer. For imaging the scattered light by the grating to forward (+ *z*) direction, a microscope objective (EC Epiplan 20× 0.4NA, Zeiss) is placed behind the grating sample such that the focal plane of the objective lens is fixed at the grating’s back surface. The real image is formed onto the CCD camera with a tube lens. A thin film analyzer is also added to obtain polarization resolved images of the scattered SPPs. The near-field of a plasmonic tip is measured and analyzed when a radially polarized beam is carefully coupled into the vortex fiber of the tip (see the explanation in Section 3.1).

Figure 22b illustrates the excitation process of the planar SPPs by the plasmonic tip and the scattering process of the planar SPPs by the bull’s eye grating. To perform the experiment, we first bring the tip in contact with the grating surface and scan over the grating to obtain the topographic image by using the SNOM head. An example of topographic image is shown in **Figure 22c**. After this, the tip apex is placed at the center of the annular gratings and about 50 nm above the gold surface. The near-field of the tip apex excites planar SPPs on the grating surface that propagates away from the tip-sample contact point toward the annular grating. When the planar SPPs reach the annular grating, they are

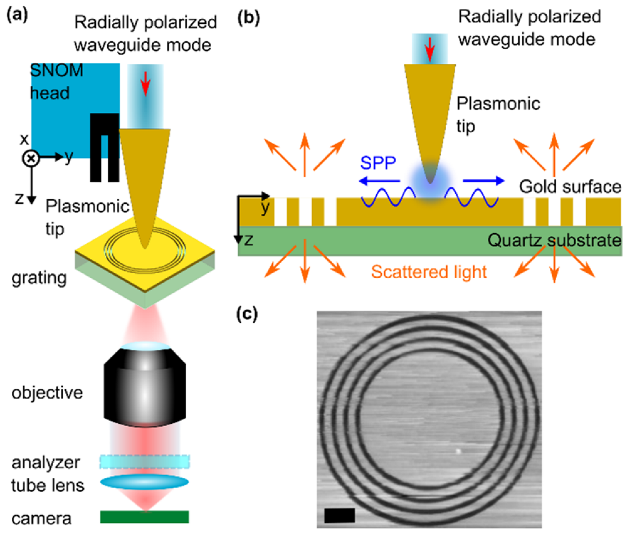

Figure 22. (a) Experimental setup for imaging the scattered light by the bull’s eye grating. **(b)** Schematics of the scattering of the planar SPPs through the bull’s eye grating. When the tip apex that locates about 50 nm above the gold surface, the apex near-field excites planar SPPs on the planar gold surface. The planar SPPs propagate toward the ring grating and get scattered through the grating. **(c)** Topographic image of the bull’s eye grating obtained by scanning the plasmonic tips in shear force method. The black bar has length scale of 2 µm. Adapted from Reference 69.

scattered to forward ($+z$) and backward ($-z$) directions. Depending on the direction to which the planar SPPs are excited on the planar gold surface, the shape of the scattered light pattern through the annular grating changes. Thus, we can indirectly imply the shape and polarization of the tip's near-field by observing the scattered light through the grating.

Results. When a radially polarized waveguide mode is coupled into the vortex fiber of the plasmonic tip, the mode propagates to the tapered part of the plasmonic tip and excites the radially polarized Co-SP mode on the outer surface of the tip. Then, the radially polarized Co-SP mode propagates to the apex and creates a longitudinal field at the apex that is oscillating along the tip axis. This process is demonstrated in **Figure 23a** where the waveguide mode in the vortex fiber is illustrated in red, and the Co-SP mode is in blue. When such longitudinal field is created at the apex and used to excite planar SPPs on a planar gold surface, it is expected that the planar SPPs will be excited to all radial direction from the tip and sample contact point. This process is demonstrated in **Figure 23b**. When the planar SPPs reach the annular grating, they are scattered to forward ($+z$) and backward ($-z$)

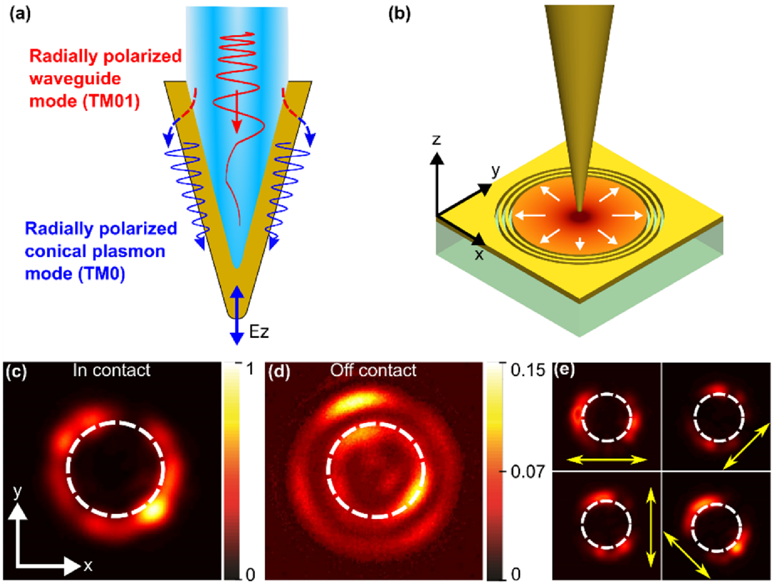

Figure 23. (a) Generation of a longitudinally oscillating field at the plasmonic tip apex. The radially polarized waveguide mode within the vortex fiber resonantly excites the fundamental and radially polarized Co-SP mode on the outer surface of the plasmonic tips. When the radially polarized Co-SP mode reaches the tip apex, it creates a longitudinal field oscillating along the tip axis. **(b)** Excitation of planar SPPs on a planar gold surface by the plasmonic tip when a radially polarized waveguide mode is coupled into the fiber tip. When the tip axis is normal to the grating surface, it is expected that the longitudinal field at the tip apex shall excite planar SPPs to all radial direction. **(c-d)** Microscope image of the scattered light without a polarization analyzer and when the tip was in (c) and out of (d) contact with the gold planar surface. **(e)** Polarization resolved images of the scattered light from the grating's back surface when the tip was in contact with the grating surface. The analyzer's transmission axis is noted with yellow arrows. The inner disk of the grating (9 µm in diameter) is indicated with dashed white circles in (c-e). Adapted from Reference 69.

directions. We image the forward scattered plasmons on the opposite side of the grating surface. The experimental results are presented in **Figure 23c-e** where dashed white circles indicate the grating’s inner disk with a diameter of 9 µm. The **Figure 23c** and **d** show the total intensity images of the scattered SPPs when the plasmonic tip is in and out of contact with the grating surface without the polarization analyzer. The total intensity of the image decreases about 25× when the tip is out of contact or retracted about 4 µm from the surface, but there is still some emission through the grating. This residue emission is due to the scattering of the tip’s far-field emission by the grating. Thus, the image in **Figure 23d** doesn’t correspond to the plasmonic tip’s near-field and is very different from the one in **Figure 23c**. We also obtain polarization resolved images of the scattered SPPs and present the results in **Figure 23e**. The transmission axis of the polarization analyzer is noted with yellow arrows. The figures show that the scattered light by the grating is radially polarized. Hence, we can imply that the planar SPPs excited by the plasmonic tip apex propagate to all radial direction away from the tip and grating contact point. Based on results in **Figure 23c** and **e**, we can conclude that the apex near-field of the plasmonic tip is indeed longitudinally oscillating along the tip axis. The inhomogeneity in **Figure 23c** and **e** can be caused by dust or other scattering particles on the grating surface.

If an aperture tip is used to excite planar SPPs instead of a plasmonic tip, the pattern of scattered light will be very different from the one in **Figure 23c**. When a linearly polarized beam is coupled into the aperture tip, there exist strong transverse field at the aperture plane that is parallel to the in-coupled mode’s polarization axis like an in-plane oscillating dipole.[66,76,96] Hence, when the aperture tip is brought in contact with the bull’s eye grating, it excites planar SPPs in the direction that is parallel to the in-coupled mode’s polarization axis. For the aperture tip, the pattern of the scattered light through the grating has a two-lobe shape.[76]

Influence of tip’s tilt with respect to the surface normal. In an ideal case, the tip is perpendicular to the planar gold surface of the grating so the excited planar SPPs will propagate equally to all radial directions. However, there can be a case where the tip is tilted with respect to the norm of the planar gold surface. The plasmonic tip is glued to a tuning fork, and the tuning fork is then mounted onto the SNOM head. Thus, the tilt of a plasmonic tip can occur due to the way the tip is mounted onto a SNOM head, and the way the tip is glued to the tuning fork. Such tilt of a tip will result in an unexpected SPP excitation pattern on the planar gold surface. To see the effect of tip tilt on the pattern of the scattered SPPs, we tilt the plasmonic tip that is mounted onto a SNOM head at a large angle that is noticeable with naked eyes and repeat the experiment. Similar to the previous case, a radially polarized beam is coupled into the vortex fiber of the tip, and the tilted plasmonic tip is placed at the center of the bull’s eye grating. The scattered planar SPPs (in the direction $+z$) by the grating is imaged when the microscope objective is focused onto the grating’s back surface. The experimental results are presented in **Figure 24a-c** where dashed white circles indicate the grating’s inner disk with a diameter of 9 µm. In **Figure 24a-b**, the total intensity images are shown when the tip was in and out of contact with the grating surface. **Figure 24c** shows the polarization resolved images where yellow arrows indicate the analyzer’s transmission axis. When the tip is out of contact and retracted about 5 µm away from the surface, the emission pattern changes, and the total intensity decreases about 10×. As **Figure 24a** shows, due to the tip’s tilt, the excited planar SPPs propagate in a directional manner rather than homogenously to all directions as shown in **Figure 23c**. If we observe the polarization resolved images in **Figure 24c**, the planar SPPs are more or less radially polarized in the xy-plane. These results suggest that depending on the tip’s tilt, the tip’s excitation pattern can vary significantly. Furthermore, the results imply that we can anticipate the tilt angle of a tip by observing the pattern of the scattered SPPs through the grating.

To estimate the tilt angle of the tip, we approximate the longitudinal field (parallel to the tip axis) at the apex of the plasmonic tip as an electric dipole that is oscillating along the tip axis. The dipole locates above a gold planar surface at a distance of 50 nm, roughly the same distance as the SNOM tip that

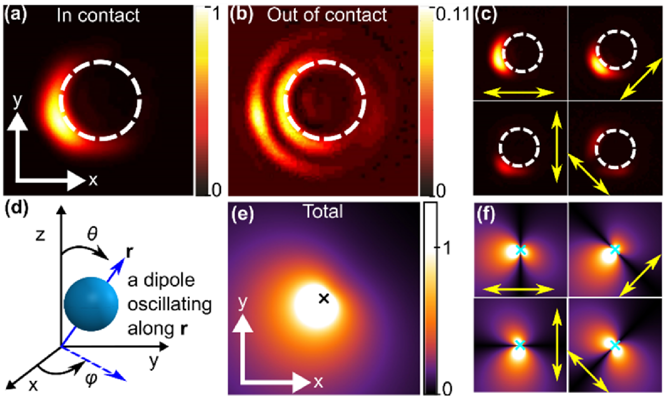

Figure 24. (a-b) Microscope image of the scattered light without a polarization analyzer when the plasmonic tip was in (a) and out of (b) contact with the gold planar surface. **(c)** Microscope image of the gratings back surface with a polarization analyzer and when the tip was in contact with the gold planar surface. The analyzer’s transmission axis is noted with yellow arrows. The inner disk of the grating (9 µm in diameter) is indicated with dashed white circles in (a-c). **(d)** Tilted dipole model. **(e)** Calculated total intensity of the excited planar SPPs by the tilted dipole. **(f)** Polarization resolved intensity of the excited planar SPPs by the tilted dipole. The analyzer’s transmission axis is noted with yellow arrows in **(c)** and **(f)**. Crosses in **(e)** and **(f)** show the dipole location on the xy-plane.

operates in the shear force mode. The electric dipole will excite SPPs that will propagate to different directions depending on the tilt angle that can be calculated analytically.[96] The dipole’s oscillation axis forms azimuthal φ and zenithal θ angles with the z-axis in a spherical coordinate as shown in **Figure 24d**. By varying these angles and comparing the calculated and measured results, we can roughly estimate the tip’s tilt angle. We calculate the absolute of the time averaged Poynting vector of planar SPPs excited by a tilted dipole according to Equation (6) in the supplementary material of Reference 96. With an educated guess, we found that when the dipole is tilted by $\varphi = 10^{o}$ and $\theta = 45^{0}$, the planar SPPs excited by the dipole has a similar pattern to that of the experimental results. The calculated results are presented in **Figure 24e-f**. Crosses in these figures show the projection of the dipole center on the xy-plane while yellow arrows in **Figure 24f** indicate the direction of the Poynting vector from the cross checked point. If we compare **Figure 24a** with **e** and **Figure 24c** with **f**, we can see that the pattern and directionality of the excited planar SPPs are well reproduced with this simple dipole model. Thus, we can conclude that the plasmonic tip in the measurement is also tilted by $\varphi = 10^{o}$ and $\theta = 45^{o}$. Since the excitation pattern of the excited SPPs change due to the tip’s tilt, we can predict that such tilted tip’s detection behavior shall also change accordingly. In many cases, adjusting SNOM tip’s tilt is challenging and often impractical; thus, one might use such bull’s eye grating to characterize the tip’s tilt and later use this information in interpreting measured near-field images by the tilted tip.

4 Plasmonic tips‘ detection

In the previous chapters, we studied theoretically the modes in plasmonic tips and their evolution during the propagation toward the tip apex and demonstrated experimentally that the radially polarized Co-SP mode creates a longitudinal field at the tip apex. The plasmonic tip and the longitudinal field at its apex can serve as a local source as we have discussed in Chapter 3, but in other cases, we would like to also detect near-fields of a sample that is illuminated and excited by a far-field focused beam. Thus, the functionality of plasmonic tips in a detection scheme is an important characteristic that will not only decide the purposes of plasmonic tips in SNOM applications but also demonstrate their performance superiority over other types of SNOM tips. To analyze the detection characteristics, we first raster scan over different focused beams with a plasmonic tip in air without the shear force feedback mechanism of the SNOM head in Section 4.1. Since there is no sample surface, this experiment will help us to understand the pure interaction between the tip apex and the local electric field at the focal plane. Thus, we can neglect the additional multiple interaction between the tip and the sample that can potentially add inclarity in the measured results. Such interaction can also influence the sample’s field distribution and eventually alter the detected fields by the tip. Since there is no feedback mechanism during scanning, there can occur a slight angle difference between the focal plane of the objective and the scanning plane of the SNOM head. This tilt might eventually influence the scanned images that are measured by the plasmonic tip, and the scanned images might be slightly different form the calculated field distributions at the focal plane of the objective. We discuss this matter in Section 4.1.2. We also raster scan over fluorescent beads (20 – 100 nm in diameter) on a glass substrate and obtain both topographic and optical near-field images to study plasmonic tips’ detection characteristics in the near-field. Fluorescent near-field measurements by plasmonic tips are explained in Section 4.2 .

4.1 Detection characteristics analyzed by raster-scanning over focused beams

4.1.1 Scanning over different focused beams

In this section, we explore the plasmonic tip's detection behavior by scanning over different tightly focused beams and measuring the scattered light from the tip apex and the coupled light directly into the tip. By employing a tightly focused beam as a sample, we can study the interaction of the plasmonic tip apex with the local electromagnetic fields of the focused beam depending on the focusing/collecting objective and the tip apex shape and size.

Figure 25a illustrates the experimental setup for raster-scanning the plasmonic tip over a tightly focused beam. As shown in the setup image, we use a high numerical aperture objective (LD EC Epiplan-Neofluar 100x 0.75NA, Zeiss) to focus a linearly polarized Gaussian beam or a radially polarized doughnut beam. The focused linearly polarized Gaussian beam supports a strong transverse field while the focused radially polarized beam provides a strong longitudinal field at the focal plane.[99] Thus, both beams help us to deduce which field component is being preferably coupled into the tip or scattered by the tip apex. The focusing objective is mounted on a nanofocusing piezo stage (P-725.4CL Pifoc, Physik Instrumente) so that the focal plane can be shifted vertically at a small step (as low as 0.5 nm) without losing the tip apex from the field of view of the objective. After the objective, the plasmonic tip is placed nearby the focal plane of the objective. The plasmonic tip is glued to a tuning fork and mounted onto a SNOM head that is controlled by a NOVA software from NT-MDT. During scanning, we turn off the feedback mechanism in the software since we scan in air not over a physical surface. Having no feedback mechanism means that there will be an unavoidable tilt between the focal plane of the objective and the scanning plane of the SNOM head. We will discuss this tilt of scanning plane with respect to the focal plane and its influence on the scanned images in next section. When a light beam is focused by the objective onto the tip apex, some of it will be scattered while others will be coupled onto the tip as plasmons. The back-scattered light from the tip apex is collected by the same focusing objective and detected with a PMT that locates after the beam splitter on the input beam path. We refer this signal to "back-scattered signal", and the optical path for detecting this signal is called as back-scattering arm. The coupled light (collected) into the plasmonic tip is detected with another PMT simultaneously with the back-scattered signal. We call this signal "transmitted signal”, and the optical path for detecting this signal is called transmission arm. The in-coupled mode in the fiber core of the plasmonic tip is also imaged on a CCD. With a thin film polarization analyzer, the polarization resolved images of the in-coupled mode are obtained. These images will help us to judge which mode is coupled into the fiber core of the plasmonic tip.

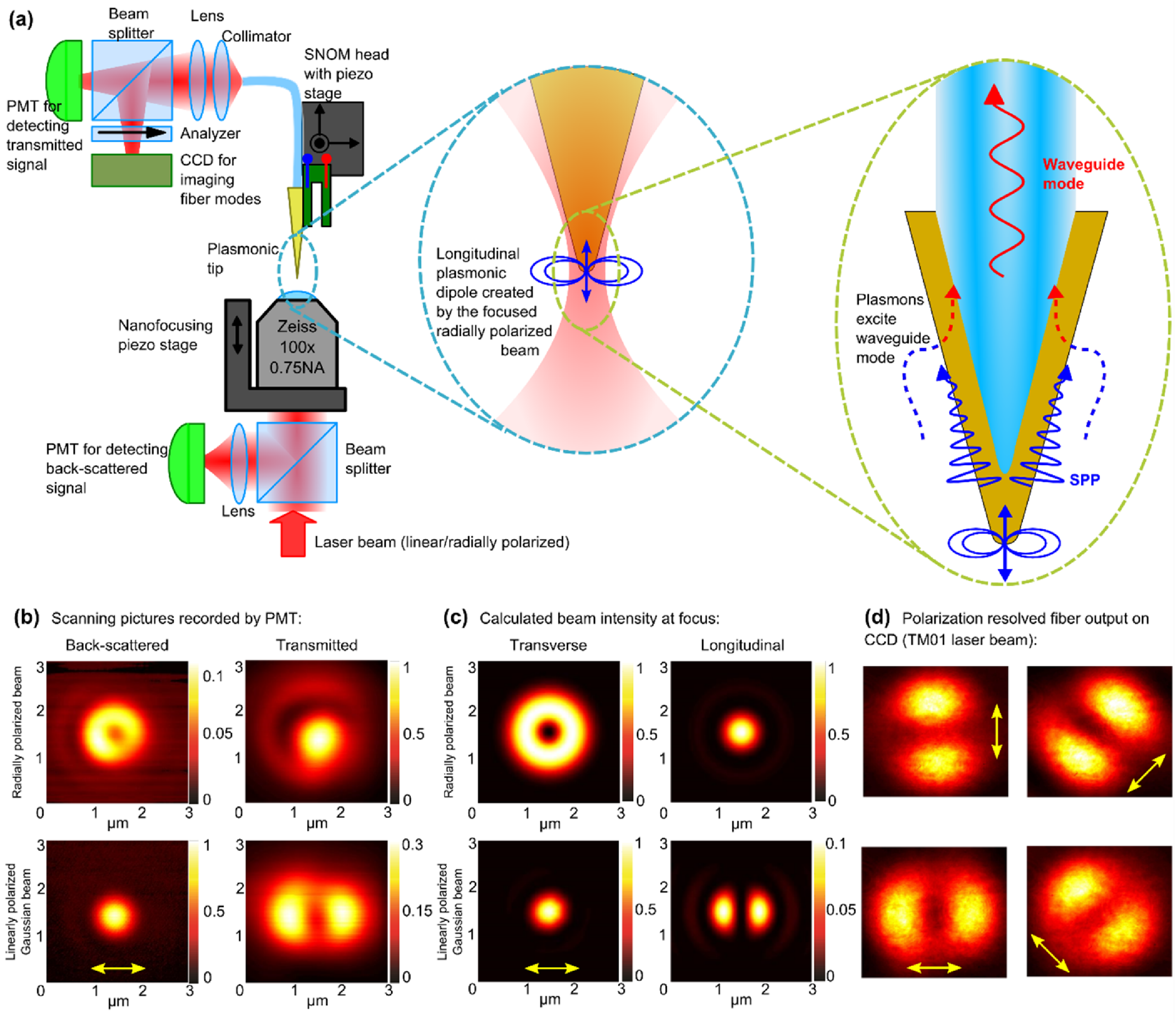

Figure 25. (a) Experimental setup for measuring the transmitted and back-scattered light during a raster scan with the plasmonic tip over a tightly focused linearly polarized Gaussian beam or radially polarized beam. **(b)** Scanned images with the plasmonic tip for two different beams. The first column shows the results from the back-scattering arm, and the second column is for the transmission arm while the first and the second rows correspond to the radially polarized and the linearly polarized Gaussian focused beams, respectively. **(c)** Calculated absolute square of electric fields at the focal plane of the objective (LD EC Epiplan-Neofluar 100x 0.75NA, Zeiss). The first and the second rows correspond to the radially polarized and the linearly polarized Gaussian focused beams, respectively. Meanwhile the first column shows the transverse fields, and the second column shows the longitudinal field. **(d)** Excited waveguide mode within the fiber of the plasmonic tip when the tip apex is placed at the center of the focal spot of the radially polarized beam. The yellow arrows indicate the transmission axis of the polarization analyzer. Adapted from Reference 69.

We can understand and predict the transmitted signal and its behavior as the interaction between the tip apex and the local electromagnetic field of the focused beam at the focal plane. When the plasmonic tip is brought at the focal plane of a tightly focused beam, due to the subwavelength apex size, the longitudinal field of the focused beam will excite plasmons at the apex of the plasmonic tip that is also longitudinally oscillating. This longitudinally oscillating local plasmons will become then a source of the fundamental radially polarized Co-SP mode because only this mode exists at the apex and supports such longitudinal field at the tip apex (see Section 2.5.1). The fundamental Co-SP mode will propagate away from the tip apex toward the increasing tip radius, and at a certain tip radius, it will resonantly excite the radially polarized waveguide mode in the fiber core of the plasmonic tip. This process is illustrated in **Figure 25a**. The interpretation of the back-scattered signal is rather complicated since it has to be thoroughly studied by changing the numerical aperture of the objective lens, the tip apex’s shape and size, and the field distribution of the focal field. Thus, we will draw conclusion based on our experimental parameters. In these experiments, we use plasmonic tips that have coating thicknesses of about 100 nm and apex sizes of 250 nm and made of vortex fibers.

We raster scan over the focused radially polarized (1st row) and linearly polarized Gaussian (2nd row) beams at the focal plane of the objective and present the experimental results in **Figure 25b**. In the figure, the 1st and the 2nd columns show the back-scattered and transmitted signals, respectively. The Gaussian beam is linearly polarized along the horizontal axis that is indicated with a yellow arrow. For the radially polarized focused beam, we obtain a doughnut shaped pattern in the back-scattering arm and a Gaussian-shaped pattern in the transmission arm. For the focused Gaussian beam, we obtain a Gaussian-shaped spot in the back-scattering arm and a two-lobe pattern in the transmission arm. To understand the measured results, we calculate the transverse (1st column) and longitudinal (2nd column) field components of the focused radially polarized (1st row) and linearly polarized Gaussian (2nd row) beams at the focal plane of the objective. In the calculation, we use the objective parameters that is mentioned earlier and apply the formulas in References 145–147. The results are presented in **Figure 25c**. By comparing **Figure 25b** and **c**, we can see that the back-scattered signals resemble the transverse field components while the transmitted signals look like the longitudinal field component. Based on these results, we can draw conclusions for the transmitted and back-scattered signals separately. First, we conclude that the plasmonic tip detects the longitudinal field in transmission. This conclusion is justified since the plasmonic tip has detected only the longitudinal field (2nd row and 2nd column in **Figure 25b**) of the focused Gaussian beam despite it is 10× weaker than the transverse field

(2nd column in **Figure 25c**). It has been shown that the plasmonic tip detects longitudinal field regardless of the focused field’s strength and shape, the numerical aperture of the focusing objective, and the apex size.[148] Keep in mind that the apex shape is a different matter. A round and parabolic shaped tip apex follows the scenario in **Figure 25a** and detects the longitudinal field, yet a flat and sharp-edged tip apex doesn’t detect any light in transmission.[148] Furthermore, the fibers that is used in fabricating the plasmonic tip affect in its detection characteristics. Plasmonic tips made of single mode fibers do not detect any light regardless of the tip apex shape[149] while the ones made of vortex fibers, multimode fibers, or few mode fibers work fine, but the transmission efficiency differs depending on the fiber. The plasmonic tips made of single mode fibers cannot work in transmission because the excited longitudinal field at the tip apex becomes a source of the radially polarized plasmonic mode that would resonantly excite the higher order radially polarized fiber mode in the tapered fiber core. This higher order mode is not supported in the single mode fiber and thus cannot propagate and reach the fiber end of the tip.

While the plasmonic always detects the longitudinal field in transmission, it is much more complicated for the back-scattered signal that should be highly dependent on the apex size and the numerical aperture of the focusing/collecting objective. The focused radially polarized beam has longitudinal and transverse fields that are almost equal in strength (for 0.75 NA) as it is shown in the 1st row of **Figure 25c**. Thus, the total field should be a large Gaussian-like pattern with a maximum intensity at the center. Despite this fact, we detect a doughnut shaped pattern with a minimum intensity at the center in the back-scattering arm as it is shown in the 1st row of **Figure 25b**. Consequently, we can deduce that the back-scattered signal (collected by 0.75 NA objective) from the tip apex with a diameter of 250 nm is mostly composed of the transverse fields. At this point, we cannot say that the plasmonic tip doesn’t scatter the longitudinal field because there can be many reasons for its absence. One reason of only detecting transverse fields could be that although the longitudinal field is scattered by the tip apex, the objective is not being able to collect it. We can anticipate that the longitudinal field at the apex will radiate back at a larger angle (like a longitudinal dipole as shown in **Figure 25a**) so it cannot be collected efficiently by an objective that has a numerical aperture of 0.75 or below compared with the transverse field components. Another reason can be that the tip apex size is so large that it interacts only weakly with the longitudinal field. Due to this weak interaction, the reflected longitudinal field is also weaker in strength than the transverse field components. Thus, one cannot see it in the back-scattered signal. It is known that sharp tips like AFM tips scatter (< 50 nm) only the longitudinal field to all direction including the backward direction that is opposite to the incoming light path.[150] Hence, with these measurements, we can only conclude that the transverse fields will be detected in the back-scattering arm for a plasmonic tip with an apex size of > 150 nm and a numerical aperture of the objective that is < 0.75. It is also evident that the metallic tip’s scattering characteristics are complex and depends on collection direction (back-scattering or side-scattering), collection volume (numerical aperture of the imaging objective), focal fields (radially polarized or linearly polarized), the apex size and shape *etc*.

Finally, we want to image the in-coupled mode in the fiber core of the plasmonic tip when the tip apex locates at the focus of the focused radially polarized beam. We move and locate the plasmonic tip apex at the maxima of the image in 1st row and 2nd column of **Figure 25b** by using the NOVA software and image the in-coupled mode. The polarization resolved images of the in-coupled fiber mode is presented in **Figure 25d** where the yellow arrows indicate the transmission axis of the polarization analyzer. As we can see in the image, the two-lobe patterns are aligned along the transmission axis of the analyzer in all 4 cases, and this behavior is unique to the radially polarized modes. Consequently, based on the experimental results, we confirm the validity of our scenario in **Figure 25a**. The focused radially polarized beam did excite the longitudinal field at the apex that, in-turn, becomes the source of the radially polarized Co-SP mode. The radially polarized Co-SP mode then resonantly excites the radially polarized fiber mode in the fiber core of the plasmonic tip that can be measured and imaged at the fiber end of the plasmonic tip.

4.1.2 Effect of tip tilt with respect to the focal plane

Since the tip is scanning in air without a feedback mechanism of the SNOM head, the scanning plane of the SNOM head and the focal plane are not necessarily parallel. The SNOM head has three legs: one motorized leg for approaching the sample surface and two mechanical legs for adjusting the height of the tip in general. The tilt is inherited from the adjustment of these three legs of the SNOM head. These three legs can only be roughly adjusted so there exists some tilt introduced by these legs’ height differences. Such tilt will influence the detected images by the plasmonic tip during scanning over the focused beam. Note that this tilt is different from the plasmonic tip’s tilt that has been discussed in Section 3.3 where the tip is tilted due to the way the tuning fork is mounted onto the SNOM head and also the way the plasmonic tip’s glued on the tuning fork. Here, the SNOM head as a whole is tilted resulting in a tilt of the scanning plane ($x'y'$ plane) with respect to the focal plane (xy plane) of the

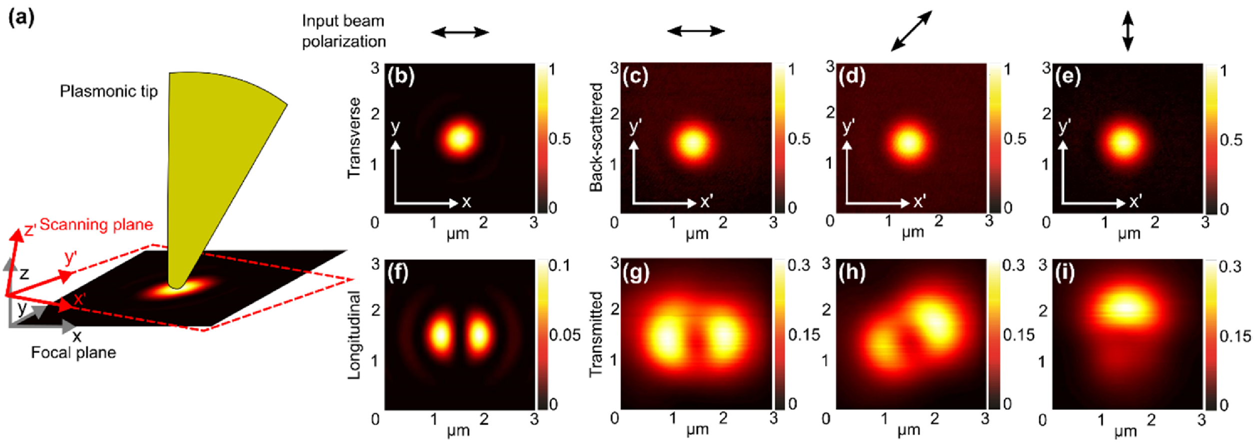

Figure 26. (a) Schematics of the scanning plane’s tilt with respect to the focal plane of the imaging objective. **(b,f)** Calculated absolute squares of transverse (b) and longitudinal (f) electric fields at the focal plane of the objective (Zeiss LD EC Epiplan-Neofluar 100x 0.75NA). The Gaussian beam is polarized along x-axis as it is shown in (f) where the two lobes are oriented along x-axis. The two lobes rotate with the input beam’s polarization axis. **(c-e)** Scanned images measured in the back-scattering arm. **(g-i)** Scanned images measured in the transmission arm. In (b-i), two figures in the same columns are obtained from one measurement where the input beam’s polarization axis is indicated on top of each column. Judging by the two-lobe patterns in (g-i), we can conclude that the scan plane is tilled in y-axis and leveled in x-axis. Adapted from Reference 69.

objective as illustrated in **Figure 26a**. We investigate the effect of the scanning plane’s tilt on the formed images (on x′y′ plane) by scanning over a linearly polarized Gaussian beam at different input polarizations. We place a lambda half plate on the input beam path and rotate it incrementally at a step of 22.5° so that the input polarization is rotated by 45°.

The calculated absolute square of the electric field of the focused Gaussian beam is presented in **Figure 26b** and **f** that are for the transverse and the longitudinal field components, respectively. The measured images in the back-scattering arm are shown in **Figure 26c-e** while the measured images in the transmission arm are presented in **Figure 26g-i**. In these figures, each column corresponds to the measured images from one experiment where the input beam polarization is indicated with a black arrow on top of each column. If **Figure 26b** is compared with **Figure 26c-e**, there is not much change, and thus we cannot say if there is any tilt in the scanning plane. This is because the tip is always aligned at the center of the scanning plane so the deviation of the scanning plane from the focal plane is none at the center and becomes larger toward the edge. The transverse field component’s shape is so small that the deviation of the scanning plane from the focal plane is not noticeable. However, it is different for the longitudinal field component that has a two-lobe pattern. If we look at **Figure 26g-i**, the two-lobe pattern rotates with the input beam polarization axis, and it is symmetric in **Figure 26g** and is not in **Figure 26h** and **i**. One lobe of the two-lobe pattern is hardly visible in **Figure 26i**. Since the pattern is symmetric along x-axis and asymmetric along y-axis, we can deduce that the scanning plane is tilted along y-axis and leveled in x-axis. For the Gaussian beam, the two-lobe pattern of the longitudinal field is sensitive to the tilt of the scanning plane. The two lobes of the longitudinal field are extended over larger area than the Gaussian spot of the transverse fields. Thus, toward the edge of the scanning plane, the tip apex is farther away from the focal plane, and the detected light is weaker in intensity. In case of the radially polarized beam, the doughnut shaped transverse field will be influenced by the tilt of the scanning plane for the same reason as it can be seen in the 1st row and 1st column of **Figure 25b**.

4.2 Fluorescence near-field measurements with plasmonic tips

In this section, we use fluorescent beads as study samples and explore the near-field detection characteristics of plasmonic tips. By doing so, we aim to demonstrate the plasmonic tips’ ability in SNOM applications.

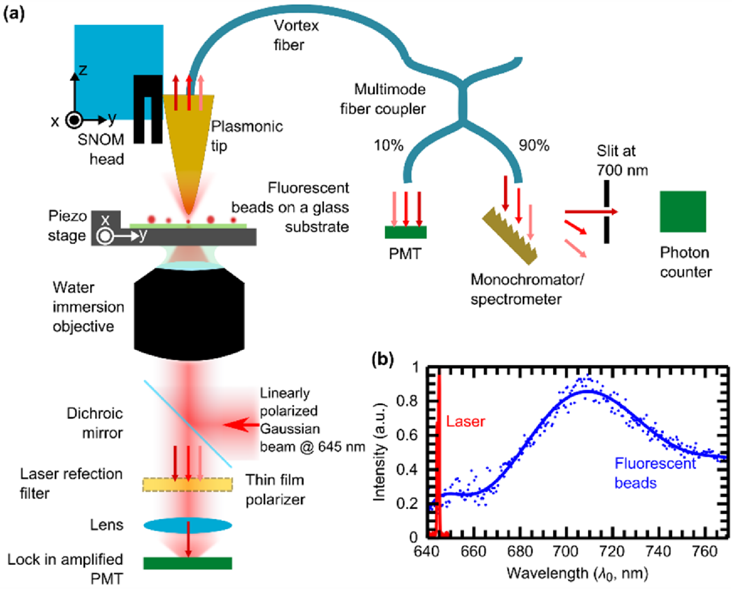

Figure 27. (a) Experimental setup for measuring the fluorescent near-fields. A linearly polarized Gaussian beam, at a wavelength of 645 nm, is used as an excitation source and is focused by a high NA objective (UPlanSApo 60×, 1.2NA, Water immersion, Olympus). There are two scanning possibilities that arewith the SNOM head and the sample piezo stage. The SNOM head is used to locate the focus spot and position the tip in it while the sample piezo stage is used for scanning and measuring the fluorescent emissions from beads. **(b)** Emission spectrum of the fluorescent beads (FP-570-02, Kisker biotech).

Experimental setup. In **Figure 27a**, we illustrate the experimental setup for investigating fluorescent near-fields with the plasmonic tip. In the experiments, we use plasmonic tips that are made of vortex fibers and have a gold coating thicknesses of about 50 nm. The tip apex sizes (diameter of curvature) are about 200 nm for such plasmonic tips. As a study sample, we use fluorescent beads (Sky blue FP-570-02, Kisker biotech) with a mean size of 60 nm. The fluorescent beads have a maximum absorption at a wavelength of 650 nm while the maximum emission is at a wavelength of 700 nm.[151] As an excitation source, we use a diode laser at a wavelength of 645 nm that emits a linearly polarized Gaussian beam. In the experiments, we use a laser beam power of about 200 µW (measured before the objective) to prevent photobleaching of the fluorescent dyes.

The liquid buffer containing the fluorescent polystyrene beads is deposited on a glass substrate and spread over the substrate evenly to achieve isolated fluorescent beads. As shown in **Figure 27a**, the sample substrate is placed on a piezo scanning stage (P-541.2CL, Physik Intstrumente) and is illuminated from bottom with a water immersion objective (UPlanSApo 60× 1.2NA Water immersion, Olympus). The SNOM head is placed above the sample substrate so the plasmonic tip can approach from above to the sample surface where the fluorescent beads are located. The experimental setup has two scanning schemes: the SNOM head scanning and the sample stage scanning. The SNOM head is used to scan with the plasmonic tip over the sample, to locate the focus spot, and eventually to place the tip at a certain position of the focus spot. Once the tip position is fixed with respect to the focus spot, the piezo stage holding the sample scans to obtain the optical and topographic images of the fluorescent beads. Furthermore, there are three optical detection channels that measure the back-scattered and the transmitted lights. The back-scattered light is measured with a PMT, and then the detected signal is lock-in amplified where the tuning fork’s resonance frequency is used as a reference signal for the lock-in amplifier (7270 DSP, Ametek). An optical filter and a dichroic mirror are placed in front of the PMT for filtering out the laser operation wavelength: a laser rejection filter (Omega optical) that blocks wavelengths of 620 – 650 nm and a dichroic mirror (650DRLP, Omega optical) that has cutoff wavelength at 660 nm. Meanwhile, the transmitted light coupled into the plasmonic tip is measured with two detectors with and without spectral filtering. The transmitted light is divided into two channels via fiber-coupler with an intensity ratio of 10% to 90%. The arm with 10% of the transmitted light is measured by a PMT without spectral filtering for imaging and locating the focal spot as has been done in Section 4.1.1. Here, however, we scan over the focused beam in contact with the glass substrate surface. The other arm with 90% of the transmitted light is coupled into a spectrometer/monochromator (HR320i, Horiba Scientific) via optical multimode fiber and then is detected by a photon counter (Count-20c-fc, Laser Components) in combination with a photon counting module (SR400, Stanford Research System). The monochromator has a transmission efficiency of about 10%. The monochromator’s grating is scanned to obtain the fluorescence emission spectrum of the fluorescent beads. We measure the fluorescence spectrum of the beads and present the results in **Figure 27b**. The red curve shows the diode laser spectrum while the fluorescence emission spectrum is illustrated in blue dots and a line that correspond to the measurement and its fitted curve, respectively.

Results. Fluorescence near-field measurement results are presented in **Figure 28**. We bring the plasmonic tip in contact with the substrate surface and scan with the tip over the focused beam. Since

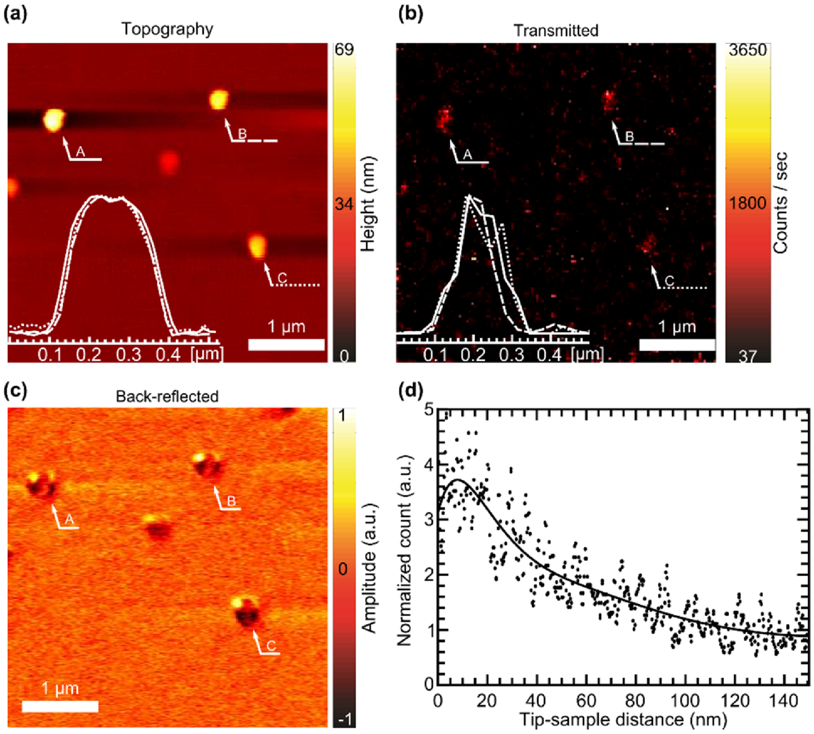

Figure 28. Fluorescent near-field measurements of the fluorescent beads obtained with a plasmonic tip**. (a)** Topographic image. Fluorescent beads are labeled as A, B, and C that have diameters of 64 nm, 44 nm, and 36 nm, respectively. Normalized horizontal cross sections of the topographic image of beads A (solid), B (dashed), and C (dotted) are shows as an inset. **(b)** Transmitted fluorescent signal detected by the photon counter that is attached to the monochromator output. The monochromator is adjusted to transmit at a wavelength of 700 nm. Normalized horizontal cross sections of the transmission image of beads A (solid), B (dashed), and C (dotted) are shows as an inset. **(c)** Back-scattered signal by the plasmonic tip apex. The back-scattered signal is amplified with a lock-in amplifier, and thus the detected back-scattered signal corresponds to the 1st order derivative of the original back-scattered signal where no signal corresponds to 0 and maximum to -1 and 1. **(d)** Fluorescence signal in transmission depending on the tip-sample distance.

we use a linearly polarized Gaussian beam, we obtain a two-lobe pattern, like the ones presented in **Figure 26f**. After this scan, we move the plasmonic tip and place it at the maximum of the longitudinal field component (at the center of the one of two lobes) of the focused beam. Once we fix the tip position with respect to the beam focus, we scan with the sample piezo stage and obtain both optical and topographical images simultaneously. The topographic image is presented in **Figure 28a**. The topographic image shows that the fluorescent beads are isolated and different in diameter that can be identified accurately by the height scale. Three fluorescent beads are selected and labeled as A, B, and C that have diameters of 64 nm, 44 nm, and 36 nm, respectively. Normalized horizontal cross sections of the topographic image of beads A (solid), B (dashed), and C (dotted) are shows as an inset in **Figure 28a**. To determine the topographical resolution, a sharp edge is scanned the rise distance from the minimum to maximum height is measured.[129,152] Although we measured a sphere instead of a sharp edge, we can still say that the topographical resolution with this plasmonic tip is at least 140 nm from the inset in **Figure 28a**. As it can be seen in the inset, the measured lateral sizes of the beads, however, are similar in size about 350 nm and are larger than the actual bead diameters. The reason is that this measured lateral size is defined by the convolution of the contour curves of the bead and the tip apex, and it will be larger than the bead diameter as long as the tip apex size (diameter $\gg$ 10 nm) is much larger than the bead diameter. When the bead diameter is small (diameter $\leq$ 10 nm), the bead acts as the scanning probe, and thus the measured topography of the bead reversely reveals the profile of the tip apex. From the topographic image, we estimate that the tip apex size is about 260 nm in this measurement. There are horizontal black lines next to the beads in the topographic image. These black lines are artifacts created during signal processing (line averaging) and thus have no physical meaning.

Meanwhile, the optical near-field images are shown in **Figure 28b** and **c** which correspond to the measured transmitted and back-scattered signals, respectively. As we can see in the transmitted signal image in **Figure 28b**, the three beads emit a relatively strong fluorescent signal that is distinguishable from the background. Normalized horizontal cross sections of the transmission image of beads A (solid), B (dashed), and C (dotted) are shows as an inset in **Figure 28b** where the edge resolution is about 100 nm. Furthermore, the emission spot maximum corresponds to the center of the fluorescent beads. The fluorescence emission spots from the three beads are similar in size that is about 190 nm, yet they differ in count rate. The larger the bead size is, the more fluorescent molecules are contained within the beads and thus the stronger the count rate will be. The transmitted fluorescence signal level also depends on the tip-sample distance. We measure the transmitted signal while the plasmonic tip approaches a fluorescent bead with a diameter of about 100 nm and present the result in **Figure 28d** where the dots represent the measured data and the line shows the fitted curve. The figure shows that when the tip approaches closer to the bead, the transmitted fluorescence signal increases several times. However, fluorescence molecules are well known to quench when the tip is too close to the molecule.[153,154] The graph in **Figure 28d** clearly shows that the signal decreases for a distance below 10 nm, yet it does not quite reach 0 because of the large bead size (diameter ~ 100 nm). Since the bead contains thousands of molecules, some molecules are still sufficiently far away from the tip apex and thus still fluoresce strongly without being quenched. In our case, we achieved a signal enhancement of about 4 times when the tip-sample distance is about 10 nm for the plasmonic tip with an apex size of about 260 nm. We expect that the enhancement will be greater if the apex size is small. It has been shown that when a sharp AFM tip (apex size ~ 20 nm) is used in fluorescence and Raman spectroscopy in s-SNOM configuration, the signal can be enhanced about 20 – 100 times due to the presence of the tip.[153,154]

Figure 28c shows the back-reflected signal image where the emission patterns are quite different from the transmitted one. The back-scattered signal is lock-in amplified where the tuning fork’s resonance frequency (1st harmonic) is used as a reference signal. Hence, the detected back-scattered signal in **Figure 28c** corresponds to the 1st order derivative of the original back-scattered signal.[155] The normalized signal level ranges from -1 to 1 where 0 indicates no signal. **Figure 28c** shows that the back-scattered signal is mostly detected from the two sides of the fluorescent beads and not from the center of the beads as is the case for the transmitted signal image in **Figure 28b**. This pattern also changes depending on the tip-sample distance. For these isolated beads, we can easily recognize the bead emissions from each individual bead, but when the beads are clustered and close to each other, the back-reflected signal image is not straightforward to understand. There can be different ways in which the image is formed in the back-scattering arm. First, when beads are clustered together and excited by a large illumination spot, multiple scatterings can happen between the bead and the tip and among the beads and coherently interfere with each other.[156–158] Hence, the detected signal no longer corresponds to the fluorescence emission from one bead that locates under the tip. Furthermore, despite the two filters placed in front of the PMT, a small portion of the laser beam can be transmitted through and detected by the PMT. This is possible because the lock-in technique is quite sensitive, and the amount of the scattered light increases compared with the fluorescence signal due to the multiples scatterers such as the tip shaft and the neighboring beads.[156–158] Thus, the back-reflected signal can be a mixture of the fluorescent signal and the laser light. These are some of the reasons for the general difficulty in interpreting the measured results in s-SNOM measurements.[156–158]

Excitation and detection process in the presence of the plasmonic tip. As we have mentioned earlier, the tip apex was placed at the maximum of the longitudinal field component of the focused beam, and we obtained the results that are presented in **Figure 28b** and **c**. After this, we moved the tip apex to the maximum of the transverse field components of the focused beam and repeated the measurement. In such case, we did not detect any signal in transmission (not shown here). This does not necessarily mean that there was no fluorescence signal. It is highly likely that the tip was not able to detect the fluorescence emission from the bead due to the fluorescent bead’s excitation mechanism, the tip’s detection mechanism, and/or the tip’s unique structure. To understand this absence of the transmitted fluorescence signal, we need to identify processes through which the fluorescent beads are excited and the emitted fluorescence signal is detected.

First, we need to look at the excitation mechanism of the fluorescent beads. As illustrated in **Figure 29**, the fluorescent beads can be excited in two ways: by the far-field illumination and by the localized near-field at the tip apex. When a laser beam of certain frequency ω_0, which is within the fluorescent molecule’s absorption spectra, is shined onto a fluorescent bead, the bead can be excited by the far-field incidence beam (see **Figure 29b**). In this case, the total absorption efficiency of the fluorescent

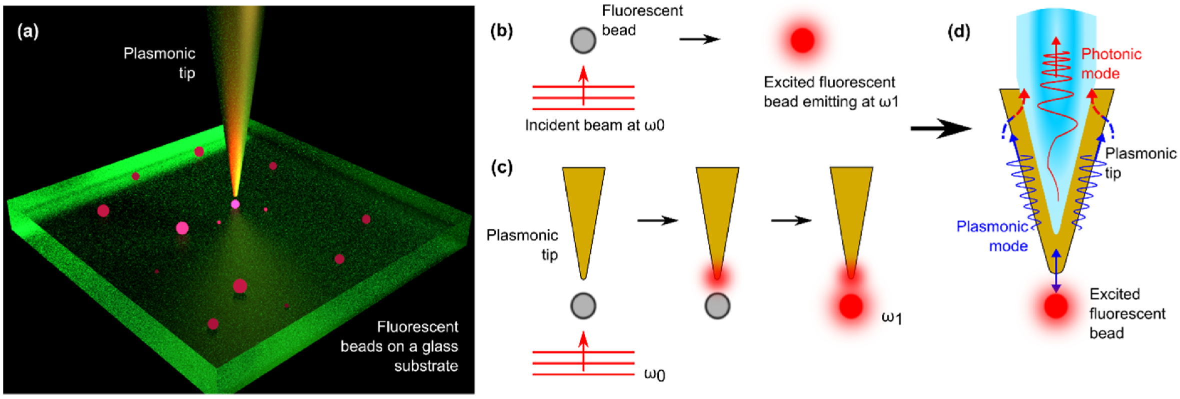

Figure 29. (a) Schematics of excitation and detection of fluorescence emission from a fluorescent bead with a plasmonic tip. When the plasmonic tip apex is at near vicinity of a fluorescent bead, the emitted fluorescence fields excite a longitudinally oscillating plasmonic field at the tip apex that in turn excites the radially polarized plasmonic mode. The plasmonic mode propagates away from the tip apex and resonantly excites the radially polarized photonic mode in the fiber core of the plasmonic tip at a certain tip radius. The photonic mode reaches the fiber end of the tip and is detected by a photo detector. **(b)** Excitation of fluorescent beads by incident beam. **(c)** Excitation of fluorescent beads by localized near-field at the plasmonic tip’s apex. **(d)** Detection of fluorescence emission from the fluorescent bead through excitation of longitudinal field at the tip apex that becomes a source of radially polarized plasmonic mode.

bead ($N\sigma/A$) is given by the ratio between the absorption cross section of the molecule (σ) and the area of the focused beam (A) and multiplied by the total number of molecules within the bead (N).[159] The absorption cross section of the molecule is defined by the nature of the molecule and thus cannot be easily changed. Meanwhile, the far-field focused beam area is defined mainly by the focusing objective's NA. Consequently, this far-field excitation process is governed by the diffraction limit of light and thus limits the absorption efficiency of the fluorescent molecule. Meanwhile, when the tip is present above the fluorescent bead, the different electric field components of the focused beam are expected to excite corresponding dipoles at the tip apex.[160] Note that for sharp tips (apex size ~ 10 nm), only the longitudinal dipole can be efficiently excited at the tip apex.[150] Since these dipoles interact and act back on the fluorescent bead that is in vicinity of the tip apex, the bead can be excited by the near-field at the plasmonic tip apex (see **Figure 29c**). In such case, the presence of the tip not only modifies the absorption cross section of the molecule by reducing the fluorescence decay rate of the molecule but also provides a localized hot spot for the excitation laser light where the spot size is no longer limited by the diffraction of light but rather the tip apex size. Consequently, the absorption efficiency of the fluorescent molecule can be improved when a sharp tip or a nano-antenna is used as a mediator between the fluorescent molecule and the excitation laser light.[153,154] Such tip or nano-antenna enhanced fluorescence excitation can be orders of magnitude more efficient than the direct far-field excitation.[161,162]

Besides these two channels of fluorescent bead excitation, the excitation efficiency of each fluorescent molecule in the bead also depends on the orientation of the fluorescent molecule with respect to the exciting field polarization axis. The maximum excitation efficiency is only possible when the molecule's dipole orientation is aligned with the exciting field's polarization axis. However, we use fluorescent beads that have a mean diameter of about 60 nm, and thus, there is expected to be hundreds of molecules per bead. Since hundreds of molecules are highly unlikely to be aligned with each other within a bead like a crystal structure, we cannot approximate the fluorescent beads as dipoles. It is safe to assume that a fluorescent bead is isotropic. Consequently, the fluorescent beads show no preference to any particular field polarization. The emitted fluorescence field from such bead is also expected to be somewhat unpolarized.

The detection efficiency by the plasmonic tip and the objective in the back-scattering arm, on the other hand, is quite sensitive to field polarization axis. As we have shown in Section 4.1, the plasmonic tip only detects the longitudinal field in transmission. Hence, the fluorescent field component that is parallel to the tip axis is detected in transmission. Such fluorescence field component excites a longitudinally oscillating plasmonic field at the tip apex that becomes the source of a propagating radially polarized plasmonic mode (see **Figure 29d**). Away from the tip apex at a certain tip radius, the plasmonic mode resonantly couples to the fiber mode within the vortex fiber of the plasmonic tip. While the plasmonic tip filters out the transverse field components of the fluorescent emission in transmission, the tip reflects the transverse field components back to the objective (see Section 4.1) that collects effectively the transverse field.

Despite the filtering of field components in transmission, this detection characteristic of the plasmonic tip doesn’t explain why we had no fluorescent signal in transmission. In fact, once the isotropic bead is excited, the amount of fluorescent signal that is transmitted through the tip is determined with respect to the emitted fluorescent signal from the tip. The plasmonic tips’ preference to the longitudinal field component is expected to affect the detection efficiency only when there is a single molecule that has well defined dipole orientation. Hence, the only thing that is changing and influencing the total transmission efficiency is the excitation condition. The longitudinal field is effectively formed at the plasmonic tip apex due to its structure; therefore, the tip enhanced fluorescence excitation is more effective when the tip is located at the maximum of the longitudinal field rather than that of the transverse field component. This could be the reason why we could detect efficiently the fluorescence signal when the tip is located at the maximum of the longitudinal field component of the focused beam.

So far, we have demonstrated the plasmonic tip’s near-field detection mechanism in this section. We believe that there are several ways to further improve the performance of the near-field detection with plasmonic tips. First, the linearly polarized Gaussian excitation beam is not an ideal choice. Only a small portion of the input beam power is translated into the measurable fluorescence transmitted signal because about 20% of the total beam power is contained in the longitudinal field component for the linearly polarized Gaussian beam focused by the given objective (UPlanSApo 60× 1.2NA Water immersion, Olympus). Increasing the beam power would only result in photobleaching of the fluorescent beads without significantly increasing the measured fluorescence signal level. One can use a radially polarized beam instead since the longitudinal field (~50% of the total beam power) is stronger for the focused radially polarized beam than the linearly polarized Gaussian beam. Second, it is crucial to have plasmonic tips with small tip apexes (< 50 nm) for improving the quality of near-field optical images. The smaller is the tip apex, the stronger is the longitudinal field at the tip apex.

Having a strong and highly localized field at the tip apex shall improve the fluorescence excitation efficiency; hence, the detection efficiency both in transmission and reflection should improve. Third, it can be more efficient to use the plasmonic tip as an illuminating source to improve the signal to background ratio (SBR) and reduce photobleaching of the molecules. In the current setup, the transmission through the plasmonic tip always contains both the incident laser beam and the fluorescence signal. Hence, we need not only a monochromator but also an optical filter to effectively reduce the background laser light. Furthermore, since the transmitted fluorescence signal level depends on the tip-sample distance, it requires several scans (each lasts ~20 minutes) to determine the optimal height level in shear-force scanning mode. The exposure of the beads to the laser light during each scan accumulates and reduces the fluorescence emission rate, eventually photobleaching the fluorescent molecules. By illuminating from the plasmonic tip, we could reduce the illumination area and duration so that the fluorescent beads would not be illuminated at all times and stay in the excited state. Instead of a continuous wave laser, we can also use a pulsed laser and synchronize it with the scan movement to reduce the excessive light exposure. Last but not least, one can exploit the strongly localized field at tip’s apex to induce two-photon absorption of the fluorescence molecules to further improve SBR (signal to background ratio) and reduce the photobleaching of the molecules. Assuming the tip apex size is sufficiently small for the superfocusing to occur, we can achieve a hot spot at the tip apex that is sufficiently strong to induce two-photon absorption for the fluorescent molecules. Since such two-photon absorption will only occur when the molecule is in vicinity of the tip apex, the molecules will be excited only when it is needed, and thus, the duration of time in which the molecule is in the excited state will reduce. This will effectively increase the molecules’ longevity.

5 Conclusions and outlook

In this thesis, we have analytically studied the guided modes in different fiber based SNOM tips, experimentally explored the excitation and the detection characteristics of plasmonic tips. We have started our study by analyzing analytically the modes in the fiber based SNOM tips to understand the functionality of different fiber based SNOM tips. In a fiber based SNOM tip, purely linearly polarized modes cannot exist since the waveguide is non-uniform in shape and has a high refractive index difference between the core and the cladding. Since the linearly polarized mode approximation is no longer valid here, we use the quasi-linearly polarized mode formalism. Within this formalism, the hybrid modes can be decoupled into two degenerate quasi-linearly polarized modes, which are orthogonal to each other. This analytical formalism offers deeper insight into the guided modes and their field evolution during the propagation through the tapered region.

We first explored the dielectric tip or the tapered fiber tip that is the simplest of all fiber based SNOM tips. We showed that as the fundamental hybrid photonic mode propagates toward the tip apex, the field penetration depth into the surrounding medium increases, and the mode's propagation constant approaches that of the surrounding medium. These changes imply that the mode slowly leaks out of the tip core and turns into a free space beam. Consequently, the field localization at the apex is not efficient for the dielectric tip despite it offers the smallest apex size among all the fiber based SNOM tips. The poor field confinement at the tip apex makes the dielectric tip a quite poor performer (poor optical resolution and low signal to noise ratio) in SNOM measurements compared with other types of fiber based SNOM tips.

The aperture tip, which is a tapered metal coated fiber with a small aperture at the apex, offers a better field confinement at the tip aperture owing to the fundamental plasmonic mode's nature. The fundamental plasmonic mode doesn't experience cutoff, and the mode size shrinks with the decreasing core radius allowing the mode to adapt and fit into the metallic aperture without restriction in its diameter. With decreasing core radius, the fundamental plasmonic mode also turns into a leaky mode so the field penetration depth increases in the dielectric core, and the field tails overlaps at the center of the core resulting in a maximum field amplitude in the fiber core. Such change of field distribution toward the tip aperture makes the plasmonic mode looking like a photonic mode and thus confuse many to misidentify it as the photonic mode. Furthermore, the transverse field is always the dominant one regardless of the core radius making the aperture tip mostly sensitive to the transverse field components during SNOM measurements. Despite offering a better field localization at the tip aperture, the aperture tip's far- to near-field conversion efficiency is about 10^{-7}% (for an Au coated tip with a full cone angle of 20° and an aperture size of about 100 nm) or less depending on the coating material, the taper angle, and the aperture diameter. The transmission efficiency of the aperture tip is mostly limited by the increasing propagation loss of the photonic and plasmonic mode with the decreasing core radius. The photonic mode, although initially excited at the fiber end of the tip, becomes extremely weak in strength toward the mode cutoff and eventually dies off before reaching the tip aperture. Meanwhile, the plasmonic mode is excited by the photonic mode with an efficiency of 0.0001% and experiences smaller propagation loss (0.1%) than the photonic one and thus reaches the tip aperture. Based on our modal analysis, we claim that the aperture tip is plasmonic in nature contrary to the conventional SNOM paradigm where it was commonly believed that the evanescent tail of the fundamental photonic mode dominates in the near-field at the aperture plane.

Meanwhile, the plasmonic tip, which is a fully metal coated tapered vortex fiber tip, provides a greater improvement in the field localization at the tip apex and in the conversion efficiency from the far- to near-fields owing to the superfocusing effect and the resonant coupling scheme. For the plasmonic tip's functionality, the radially polarized fundamental plasmonic mode at the outer metal layer (surrounding medium-metal cladding) plays a crucial role since it is the one and only mode that gives rise to the superfocusing effect. During the propagation toward the tip apex, the propagation constant of the plasmonic mode increases so the effective wavelength of the plasmonic mode shrinks. Due to this effect, the plasmonic mode becomes confined in the longitudinal direction in addition to the natural transverse confinement of surface plasmon polaritons. Furthermore, the penetration depth of the longitudinal field increases in the metal core with decreasing core radius, and thus the field tails start to overlap in the metal core. This means that there will be an in-phase (due to the symmetric field distribution of the radially polarized beam) free-electron oscillation in the metal core that enhances the plasmonic field amplitude even more. Because of this effect and also the shrinking size of the waveguide dimension, the field amplitude of the plasmonic mode increases as the mode propagates toward the tip aperture. Together, the confinement of fields longitudinally and transversally and the enhancement of field amplitude result in a strong and highly confined field at the tip apex. The smaller is the apex size of the plasmonic tip, the stronger is the superfocusing effects. The small apex size also ensures a better topographic resolution. The radially polarized plasmonic mode at the outer metal interface can be resonantly excited by the radially polarized photonic mode in the tapered fiber core or vice versa for excitation and detection schemes in SNOM measurements. Unlike the low transmission efficiency of the aperture tip, the conversion efficiency of the plasmonic tip can be as high as ≈ 90% depending on the coating thickness, the coating metal type, the taper angle, and the operation wavelength. By employing the superfocusing effect and having a large power conversion efficiency, the plasmonic tip has the potential to outperform other types of SNOM tips, both fiber based SNOM tips and apertureless s-SNOM tips.

We fabricated plasmonic tips by using the vortex fiber, which has double ring cores for guiding safely the radially polarized beams over a long distance, and explored experimentally their excitation and detection characteristics. By carefully and selectively exciting only the radially polarized fiber mode in the vortex fiber of the plasmonic tip, we showed that the radially polarized photonic mode propagates and evolves adiabatically in the plasmonic tip keeping its polarization state. We also showed that when the radially polarized plasmonic mode reaches the tip apex, it emits to the side and as well as to the front. The tip's front emission is shown to be doughnut shaped and radially polarized whilst the side emission of the tip apex is polarized along the tip axis. Since such characteristics are unique to the fundamental radially polarized plasmonic mode, these far-field emissions prove that the fundamental radially polarized plasmonic mode, that has the superfocusing capability, is indeed successfully excited. The plasmonic mode and its excitation depends on the surrounding medium since the mode is at the outer metal interface. By immersing the tip in different liquids and probing the tip emission, we demonstrated that the plasmonic tip's coupling efficiency and the field confinement can be improved in optically dense media. Such effect can be used for optical tweezing and trapping applications in liquid environments. We also measured the plasmonic tip's apex near-field by exciting surface plasmon polaritons on a planar gold surface, scattering them with an annular grating, and then imaging the scattered surface plasmon polaritons with a microscope objective. The measurement results showed that the plasmonic tip excites planar surface plasmon polaritons to all radial directions indicating that the field at the tip apex is longitudinally oscillating along the tip axis. Due to this longitudinal field at the apex, the plasmonic tip also detects the longitudinal field in a transmission scheme. We demonstrated this characteristic by scanning over tightly focused linearly and radially polarized beams. Such behavior is very different from the aperture tip that detects and excites mostly the transverse fields. Lastly, we explored the plasmonic tip's detection ability in the near-field by scanning over fluorescent beads and measuring the fluorescent signals with the plasmonic tip. By selectively exciting the fluorescent beads either by the longitudinal or by the transverse field of the focused Gaussian beam, we demonstrated that the tip and the longitudinal plasmonic field at its apex act back on the beads improving the absorption of the fluorescent beads and thus the fluorescence emission.

So far, we have presented a detailed analytical and experimental study on the plasmonic tip's functionality and the excitation and detection characteristics. The plasmonic tip is at its early development stage and can be further improved in its performance significantly by sharpening its tip apex further below 50 nm. However, at the current stage, we would still like to compare its performance with other conventional SNOM tips and discuss where it stands in terms of its performance capability. Among many different criteria, the most important ones, that determine the SNOM measurements' quality, are the optical and the lateral topographical resolutions, the near-field contrast from background or the signal to background ratio, and the far- to near-field conversion efficiency. First, with the current state of the art technology, the best optical and lateral topographical resolution can be obtained with the AFM based s-SNOM where the tip size is about 20 nm so the both resolutions are about 50 nm. Meanwhile, they are worst with the conventional circular aperture tip (topographical resolution > 300 nm and optical resolution > 100 nm). The plasmonic tip stands somewhere in between (topographical resolution ≈ 150 nm and optical resolution ≈ 100 nm). Second, the near-field contrast and signal to background strongly depend on the sample that is being investigated and the experimental configuration. Although the physical background signal is huge compared with the near-field signal from the tip, the AFM tip in s-SNOM offers a better contrast by employing sophisticated background suppression techniques such as heterodyne, pseudo-heterodyne, cross-polarization *etc*. However, when studying clustered particles or propagating surface plasmon polaritons, the interference between the scattered light and the incident light can make the interpretation of the measured image difficult for the AFM tip in s-SNOM. While the conventional aperture tip is not well known for its optical resolution and contrast, it can offer a better near-field contrast in such cases. In certain experimental configuration, the plasmonic tip can potentially offer better or similar optical contrast as the AFM tip in s-SNOM without employing sophisticated background suppression techniques. Lastly, the far- to near-field conversion efficiency is expected to be greatest for the plasmonic tip (as high as 70%) that is at least several orders of magnitude larger than both aperture tip (less than 10^{-5}%) and AFM tip in s-SNOM (less than 1%). The far- to near-field conversion efficiency is worst for the aperture tips due to the strong absorption of the photonic mode by the metal cladding. In general, the plasmonic tip offers a simple (no need for more instruments to suppress background light) and easily accessible (fiber in- and out-coupling) experimental condition at the cost of moderate to good enough optical and topographical resolutions.

Nevertheless, there is more to be done to exploit the full potential of the plasmonic tip especially the superfocusing effect in SNOM measurements. The most important next step is the sharpening of the tip apex (in our case was normally larger than 150 nm) down to 50 nm or below since every aspect of plasmonic tip's performance depends on the apex size. The superfocusing effect itself occurs below the tip radius of about 50 nm for a gold coated plasmonic tip operating at a laser wavelength around 800 nm. Once a small tip apex size is achieved, there are many interesting applications for the plasmonic tip. Single molecules and particles can be studied with great versatility. Fluorescent and Raman spectroscopy with sharpened plasmonic tips are expected to be as good as or even better than the ones performed with s-SNOM. Furthermore, instead of the conventional far-field excitation, we can employ the plasmonic tip as both a local source and a detector by introducing a decoupling mechanism in the input beam path where the light is coupled into the vortex fiber of the plasmonic tip. This experimental scheme would reduce the laser exposure time of the fluorescent molecules or dyes so reducing the possibility of photobleaching. Since the excitation and detection process of the fluorescent molecules will employ the superfocusing effect, this could result in huge improvements in measurements' resolution, signal to noise ratio, contrast, and detection efficiency. Furthermore, single molecules and nanoparticles can be studied spectrally and temporally with the plasmonic tip. The presence of the tip or the substrate is expected to alter the molecular energy diagram so both the emission spectrum and relaxation decay time of a molecule can be different than for the case where the single molecules are isolated and excited by a far-field focused beam. By using the plasmonic tip as a tweezer in a liquid environment, one can trap and levitate a single nanoparticle at the tip apex to study its characteristics without the influence from the substrate. Tip enhanced Raman spectroscopy (TERS) is another interesting application for plasmonic tips. During TERS measurements, the plasmonic tip might preferentially enhance and detect certain vibrational states depending on the molecular orientation with respect to the tip axis. Currently, our plasmonic tips are glued to a tuning fork and scan over a sample in the shear force mode which offers the possibility of measuring the optical near-field signal in the constant height mode and thus is good for fluorescence and Raman measurements. However, in the shear force mode, the feedback measurement for controlling the tip-sample distance is not as sensitive as that of the tapping mode operation. For a sharp plasmonic tip with a small and sharp tip apex, it can be advantageous to operate in the tapping mode since it requires more sensitivity to prevent the tip apex from damage during the scanning and landing on the sample. One could explore a way of producing bent plasmonic tips that would enable the tapping mode operation and study their excitation and detection characteristics during SNOM measurements.

Overall, we would like to emphasize the high potential of plasmonic tips for scanning near-field optical microscopy and spectroscopy applications, and we hope that this thesis can be a valuable contribution to the field of high resolution and highly efficient scanning near-field optical microscopy.

6 Zusammenfassung

In dieser Arbeit untersuchen wir analytisch und experimentell plasmonische Tips, die vollständig metallbeschichtete getaperte Vortex-Faserspitzen für die optische Nahfeldmikroskopie sind. Verglichen mit anderen Typen von faserbasierten SNOM-Tips liefert die plasmonische Tips eine Verbesserung bezüglich der Feldlokalisierung am Ende der Spitze und bezüglich der Umwandlungseffizienz von den Fernfeldern zu den Nahfeldern, was die besondere Eigenschaft der radial polarisierten Plasmon Polaritonen auf der konischen und metallischen Spitze und dem resonanten Kopplungsprozess von Plasmon Polaritonen zu Fasermoden entspringt. Aufgrund der schrumpfenden Größe des Spitzendurchmessers in Richtung des Apex nimmt die effektive Wellenlänge des radial polarisierten plasmonischen Mode ab, wodurch das plasmonische Feld zusätzlich zur natürlichen transversalen Lokalisierung der Oberflächenplasmonenpolaritonen in Längsrichtung lokarlisiert wird. Darüber hinaus nimmt die Feldamplitude des plasmonischen Mode durch die phasengleiche Oszillation der freien Elektronen gases im Metallkern und die schrumpfende Größe der Wellenleiterdimension zu. Die 3-dimensionale Eingrenzung des elektromagnetischen Feldes und die Erhöhung der Feldamplitude führen zu einem starken und lokalisierten Feld an der Spitze. Dieser Effekt wird als Plasmon-Superfokussierungseffekt bezeichnet und tritt nur für den radial polarisierten plasmonischen Mode auf, der durch den radial polarisierten Fasermode im Faserkern der Spitze resonant angeregt werden kann.

In den Experimenten stellten wir plasmonische Spitzen mittels der Vortex-Faser, die einen Doppelringkern hat, her und legten ihre Anregungs- und Detektionscharakteristika offen. Mittels selektiver Anregung der radial polarisierten Fasermode in der Vortex-Faser der plasmonischen Spitze und mittels Analyse der Fernfeldemissionsbilder des Spitzenendes zeigten wir, dass die fundamentale radial polarisierte plasmonische Mode, die superfokussierende Eigenschaft hat, tatsächlich erfolgreich anregbar ist. Durch Immersion der Spitze in Flüssigkeiten mit unterschiedlicher Brechzahl und Testen der Spitzen-Emission demonstrierten wir, dass die plasmonische Spitzen-Kopplungseffizienz und die

Feldbegrenzung in optisch dichten Medien weiter verbessert werden kann. Wir sondieren auch das Nahfeld des Endes plasmonischer Spitze mit einem Ringgitter auf einer ebenen Goldoberfläche. Die Ergebnisse zeigten, dass die plasmonische Spitze planare SPP-Moden in allen radialen Richtungen anregt, was darauf hinweist, dass das Feld am Ende der Spitze longitudinal entlang der Achse der Spitze oszilliert. Aufgrund dieses longitudinalen Feldes am Ende detektiert die plasmonische Spitze auch das longitudinale Feld in Transmission, was durch Scannen über eng fokussierte, linear und radial polarisierte Strahlenbündel gezeigt wurde. Letztlich charakterisieren wir das Nahfeld von fluoreszierenden Kügelchen mit der plasmonischen Spitze und zeigten, dass die Spitze und das longitudinale Feld an ihrem Ende auf die Kügelchen zurückwirken, was die Absorption der fluoreszierenden Kügelchen und somit die Fluoreszenzemission verbessert.

Insgesamt möchten wir das hohe Potenzial der plasmonischen Spitzen für die optische Nahfeldmikroskopie und Spektroskopie betonen und hoffen, dass diese Arbeit einen wertvollen Beitrag zum dem Gebiet der hochauflösenden und hocheffizienten optische Nahfeldmikroskopie liefert.

A Symbols, constants, and conventions

$\mathrm{H}_m^{(1)}(r)$	Hankel function of the 1st kind of m-th order where r is a variable
$\mathrm{J}_m(r)$	Bessel function of the 1st kind of m-th order where r is a variable
δ^2	Coupling constant that is described by the overlap integral of the individual mode's field profile
$\mathbf{E}_{\parallel}$	Longitudinal electric field
$\mathbf{E}_{\perp}$	Transverse electric field
$\bar{A}$	Field amplitude
E_j	j electric field component
H_j	j magnetic field component
k_0	Free-space wavenumber
n_l	Refractive index of a medium l
$\alpha_{1\to 2}$	Coupling coefficient that describes the coupling strength from the mode 1 to the mode 2
β'	Real part of the propagation constant
β''	Imaginary part of the propagation constant
ε_0	Vacuum permittivity
ε_l	Dielectric constants of a medium l
η_{x}	Coupling coefficient of the mode x
λ_0	Free-space wavelength
μ_0	Vacuum permeability
ξ_{WG}	Power of the mode x
ρ_0	Waveguide core radius
υ	Propagation constant difference rate per unit length
A	Field amplitude
B	Field amplitude
C	Field amplitude
D	Field amplitude
P	Total time averaged power
T	Power conversion efficiency

a	Waveguide core radius
b	Tip radius
d	Coating thickness
t	Time
z	Height axis
β	Propagation constant or the wavevector along z-axis
γ	Transversal wavevector in the cladding
ζ	Transversal wavevector in the core
θ	Tapering angle
ν	Azimuthal mode number
ρ	Radial axis
φ	Azimuthal axis
ψ	Phase constant
ω	Angular frequency

B Abbreviations

3D	Three dimensional
AFM	Atomic force microscopy
CCD	Charge coupled device
CoSP	Conical surface plasmon
DUV	Deep ultraviolet
EUV	Extreme ultraviolet
FIB	Focused ion beam
FWHM	Full width half maxima
MFM	Magnetic force microscopy
NA	Numerical aperture
OAM	Orbital angular momentum
PALM	Photoactivated localization microscopy
PMT	Photomultiplier tube
SBR	Signal to background ratio
SEM	Scanning electron microscopy
SIM	Structured illumination microscopy
SNOM	Scanning near-field optical microscopy
SNR	Signal to noise ratio
SPM	Scanning probe microscopy
SPP	Surface plasmon polariton
s-SNOM	Scattering SNOM
STED	Stimulated emission depletion microscopy
STM	Scanning tunneling microscopy
STORM	Stochastic optical reconstruction microscopy
TE	Transverse electric
TERS	Tip enhanced Raman spectroscopy
TM	Transverse magnetic
UV	Ultraviolet

C Publications

C.1 Peer-reviewed journals

- B. N. Tugchin, N. Janunts, M. Steinert, K. Dietrich, E.-B. Kley, A. Tunnermann, and T. Pertsch: *Quasi-linearly polarized hybrid modes in tapered and metal-coated tips with circular apertures: understanding the functionality of aperture tips.* New Journal of Physics, 2017, 19, 063024.
- B. N. Tugchin, N. Janunts, M. Steinert, K. Dietrich, D. Sivun, S. Ramachandran, K. V. Nerkararyan, A. Tunnermann, and T. Pertsch: *Controlling the excitation of radially polarized conical plasmons in plasmonic tips in liquids*. RCS Advances, 2016, 6, 53273.
- B. N. Tugchin, N. Janunts, A. E. Klein, M. Steinert, S. Fasold, S. Diziain, M. Sison, E.-B. Kley, A. Tunnermann, and T. Pertsch: *Plasmonic Tip Based on Excitation of Radially Polarized Conical Surface Plasmon Polariton for Detecting Longitudinal and Transversal Fields.* ACS Photonics, 2015, 2, 1468–1475.

C.2 In preparation

- R. Brüning, B. N. Tugchin, F.Zimmermann, N. Janunts, S. Schröter, S.Nolte, T. Pertsch, and M. Duparré: *Excitation of conical vector plasmonic modes in vortex-fiber-plasmonic tip.* In preparation.

C.3 Conference talks

- T. Pertsch, B. N. Tugchin, and N. Janunts: *Towards superfocusing SNOM tips: Coupling of surface plasmon polaritons to dielectric waveguide modes in tapered ring-profile fibers,* International Symposium “20 Years Nano-Optics”, 19th September to 21st September 2017, Erlangen, Germany.

- B. N. Tugchin, N. Janunts, A. E. Klein, M. Steinert, S. Fasold, K. Dietrich, A. Tunnermann, and T. Pertsch: *Plasmonic tip based on excitation and superfocusing of the radially polarized surface plasmon polaritons*. SPIE Photonics Europe, 3rd April to 7th April 2016, Brussels, Belgium.
- B. N. Tugchin, N. Janunts, A. E. Klein, M. Steinert, S. Fasold, K. Dietrich, A. Tunnermann, and T. Pertsch: *Plasmonic tip based on excitation of radially polarized conical surface plasmon polaritons*. DokDok 2015, 11th October to 15th October 2015, Eisenach, Germany.
- B. N. Tugchin, N. Janunts, A. E. Klein, M. Steinert, S. Fasold, K. Dietrich, A. Tunnermann, and T. Pertsch: *Scanning near-field optical microscope probe based on plasmonic superfocusing*. ASP-Seminar, 24th April 2015, Jena, Germany.

C.4 Conference poster presentations

- B. N. Tugchin, N. Janunts, M. Steinert, S. Fasold, K. Dietrich, and T. Pertsch: *Plasmonic tips based on the resonant coupling between radially polarized photonic and plasmonic modes* International Symposium "20 Years Nano-Optics", 19st September to 21st September 2017, Erlangen, Germany.
- B. N. Tugchin, N. Janunts, A. Tunnermann, and T. Pertsch: *Probing Plasmon Excitation in a Plasmonic Tip Immersed in Liquids.* The 7th International Conference on Surface Plasmon Polariton, 31st May to 5th June 2015, Jerusalem, Israel.
- N. Janunts, B. N. Tugchin, A. E. Klein, M. Steinert, D.Sivun, M.Sison, E.-B. Kley, A. Tunnermann, and T. Pertsch: *Excitation of Radially Polarized Conical Surface Plasmon Polariton.* The 7th International Conference on Surface Plasmon Polariton, 31st May to 5th June 2015, Jerusalem, Israel.

D Acknowledgements

I would like to express my deepest gratitude to Prof. Dr. Thomas Pertsch and Abbe School of Photonics for giving me the opportunity to study and work in the nanooptics group at the Institute of Applied Physics at Friedrich-Schiller-University Jena. Prof. Dr. Thomas Pertsch has provided supported my research work with abundance of scientific instruments and support that created favorable research and working environment.

During my study, Dr. Norik Janunts shared his invaluable time and wisdom in discussing my work and direct the research to the right direction for which I'm immensely grateful.

The current work would have been impossible without collaboration with experts and collaborators. I would like to thank Dr. Norik Janunts, Dr. Angela Klein, Dr. Severine Diziain, Kay Dietrich, Michael Steinert, and Stefan Fasold with Institute of Applied Physics, Friedrich-Schiller-University Jena; Dr. Michael Duparré and Robert Brüning with Institute of Applied Optics, Friedrich-Schiller-University Jena; and Prof. Dr. Siddhard Ramachandran with Boston University; and Prof. Dr. Khachatur V. Nerkararyan with Yerevan State University. Dr. Norik Janunts, Dr. Angela Klein, and Dr. Severine Diziain have shared their experience and knowledge in SNOM and helped in improving the experimental setups. Kay Dietrich, Michael Steinert, and Stefan Fasold have produced the SNOM tips and manufactured micro and nano-structured samples. Although not included in the current work, I would like to thank Dr. Michael Duparré and Robert Brüning for our collaboration on the vectorial modal analysis of the vortex fibers. I'm also grateful that Prof. Dr. Siddhard Ramachandran introduced us the vortex fiber and shared his expert opinion with us. I would also like to express my deepest appreciation to Prof. Dr. Khachatur V. Nerkararyan for valuable discussion and advice.

I would like express my gratitude to the nanooptics group members and colleagues and all the staff members of Institute of Applied Physics for their help and support.

My sincere thanks also goes to Alexander Brown, Dr. Norik Janunts, Dr. Michael Gölles, and Prof. Dr. Thomas Pertsch for proof-reading this dissertation and sharing their invaluable and constructive comments to improve the quality of the work.

Last but not least, I would like to thank my dear family and friends for their unconditional support and positive influence that gave me the determination and strength when in doubt.

E Curriculum vitae

Personal data

Name	Bayarjargal Narantsatsralt Tugchin
Date of birth	March 8, 1984
Place of birth	Ulaanbaatar, Mongolia

Academic career

01/2018	Submitted the doctoral thesis entitled “Excitation and Superfocusing of the Radially Polarized Conical Surface Plasmon Polaritons”
01/2013 – current	Scientific employee and PhD student at the Institute of Applied Physics at the Friedrich-Schiller-Universität Jena, Germany

Education

07/2012	Earned Master of Science degree from the Friedrich-Schiller-Universität Jena, Germany
06/2012	Master thesis entitled “Resonant Excitation of Conical Surface Plasmon Polaritons”
10/2009 – 06/2012	Studied Master of Photonics at the Friedrich-Schiller-Universität Jena, Germany
02/2008	Earned Bachelor of Engineering degree from Inha University, Incheon, Korea
11/2007	Bachelor thesis entitled “Performance Analysis on Optical Fiber Hydrophone”
03/2004 – 02/2008	Studied Information and Technology at Inha University, Incheon, Korea
09/2002 – 11/2003	Korean language course at Ulaanbaatar College, Ulaanbaatar, Mongolia
09/2001 – 07/2002	Studied at Mongolian University of Science and Technology, Ulaanbaatar, Mongolia
06/2001	Earned diploma of secondary education, Ulaanbaatar, Mongolia
09/1991 – 06/2001	13th School of secondary education, Ulaanbaatar, Mongolia

08.01.2018, Jena Bayarjargal Narantsatsralt Tugchin

F Ehrenwörtlich Erklärung

Ich erkläre hiermit ehrenwörtlich, dass ich die vorliegende Arbeit selbständig, ohne unzulässige Hilfe Dritter und ohne Benutzung anderer als der angegebenen Hilfsmittel und Literatur angefertigt habe. Die aus anderen Quellen direkt oder indirekt übernommenen Daten und Konzepte sind unter Angabe der Quelle gekennzeichnet.

Bei der Auswahl und Auswertung folgenden Materials haben mir die nachstehend aufgeführten Personen in der jeweils beschriebenen Weise entgeltlich/unentgeltlich geholfen:

1. Prof. Dr. Thomas Pertsch hat die gesamte Promotion betreut.
2. Dr. Norik Janunts hat das Projekt betreut und die experimentellen Studien begleitet und beraten.
3. Kay Dietrich und Stefan Fasold halfen bei der Goldbeschichtung der plasmonische Spitzen, die in den experimentellen Studien verwendet wurden.
4. Michael Steinert half bei der Nanostrukturierung der Proben, die in den experimentellen Studien verwendet wurden.
5. Dr. Michael Gölles und Prof. Dr. Thomas Pertsch halfen bei der Übersetzung der Zusammenfassung and Thesen ins Deutsche.

Weitere Personen waren an der inhaltlich-materiellen Erstellung der vorliegenden Arbeit nicht beteiligt. Insbesondere habe ich hierfür nicht die entgeltliche Hilfe von Vermittlungs- bzw. Beratungsdiensten (Promotionsberater oder andere Personen) in Anspruch genommen.

Niemand hat von mir unmittelbar oder mittelbar geldwerte Leistungen für Arbeiten erhalten, die im Zusammenhang mit dem Inhalt der vorgelegten Dissertation stehen.

Die Arbeit wurde bisher weder im In- noch im Ausland in gleicher oder ähnlicher Form einer anderen Prüfungsbehörde vorgelegt.

Die geltende Promotionsordnung der Physikalisch-Astronomischen Fakultät ist mir bekannt.

Ich versichere ehrenwörtlich, dass ich nach bestem Wissen die reine Wahrheit gesagt und nichts verschwiegen habe.

08.01.2018 Bayarjargal Narantsatsralt Tugchin

G Bibliography

(1) Abbe, E. Beiträge Zur Theorie Des Mikroskops Und Der Mikroskopischen Wahrnehmung. *Arch. für Mikroskopische Anat.* **1873**, *9* (1), 413–468.

(2) Wagner, C.; Harned, N. EUV Lithography: Lithography Gets Extreme. *Nat. Photonics* **2010**, *4* (1), 24–26.

(3) Colon, D. J. New Lithography Excimer Light Source Technology for ArF (193 Nm) Semiconductor Manufacturing. In *Advanced Semiconductor Manufacturing Conference and Workshop, 2003 IEEEI/SEMI*; IEEE; pp 304–309.

(4) Leading Chipmakers Eye EUV Lithography to Save Moore's Law - IEEE Spectrum http://spectrum.ieee.org/semiconductors/devices/leading-chipmakers-eye-euv-lithography-to-save-moores-law (accessed Feb 14, 2017).

(5) Semiconductor Engineering: The Week In Review: Manufacturing http://semiengineering.com/the-week-in-review-manufacturing-116/ (accessed Feb 14, 2017).

(6) Carl Zeiss Microscopy, Objective Assistant https://www.micro-shop.zeiss.com/index.php?s=77609713acbd04&l=en&p=us&f=o (accessed Feb 15, 2017).

(7) Gross, H. *Imaging and Aberration Theory*; Friedrich-Schiller-Universität Jena, 2016.

(8) Quabis, S.; Dorn, R.; Eberler, M.; Glöckl, O.; Leuchs, G. Focusing Light to a Tighter Spot. *Opt. Commun.* **2000**, *179* (1–6), 1–7.

(9) Sheppard, C. J. R.; Choudhury, A. Annular Pupils, Radial Polarization, and Superresolution. *Appl. Opt.* **2004**, *43* (22), 4322.

(10) Klar, T. A.; Jakobs, S.; Dyba, M.; Egner, A.; Hell, S. W. Fluorescence Microscopy with Diffraction Resolution Barrier Broken by Stimulated Emission. *Proc. Natl. Acad. Sci.* **2000**, *97* (15), 8206–8210.

(11) Geumann, U.; Schäfer, C.; Riedel, D.; Jahn, R.; Rizzoli, S. O. Synaptic Membrane Proteins Form Stable Microdomains in Early Endosomes. *Microsc. Res. Tech.* **2009**, *73* (6), 606–617.

(12) Halemani, N. D.; Bethani, I.; Rizzoli, S. O.; Lang, T. Structure and Dynamics of a Two-Helix SNARE Complex in Live Cells. *Traffic* **2010**, *11* (3), 394–404.

(13) Engelhardt, J.; Keller, J.; Hoyer, P.; Reuss, M.; Staudt, T.; Hell, S. W. Molecular Orientation Affects Localization Accuracy in Superresolution Far-Field Fluorescence Microscopy. *Nano Lett.* **2011**, *11* (1), 209–213.

(14) Betzig, E.; Patterson, G. H.; Sougrat, R.; Lindwasser, O. W.; Olenych, S.; Bonifacino, J. S.; Davidson, M. W.; Lippincott-Schwartz, J.; Hess, H. F. Imaging Intracellular Fluorescent Proteins at Nanometer Resolution. *Science (80-.).* **2006**, *313* (5793), 1642–1645.

(15) Rust, M. J.; Bates, M.; Zhuang, X. Sub-Diffraction-Limit Imaging by Stochastic Optical Reconstruction Microscopy (STORM). *Nat. Methods* **2006**, *3* (10), 793–796.

(16) Heintzmann, R.; Cremer, C. G. Laterally Modulated Excitation Microscopy: Improvement of Resolution by Using a Diffraction Grating. In; International Society for Optics and Photonics, 1999; pp 185–196.

(17) Karadaglić, D.; Wilson, T. Image Formation in Structured Illumination Wide-Field Fluorescence Microscopy. *Micron* **2008**, *39* (7), 808–818.

(18) G. Binnig, H. R. Scanning Tunneling Microscopy. *IBM J. Res. Dev.* **1986**, *30* (4), 355.

(19) Binnig, G.; Quate, C. F.; Gerber, C. Atomic Force Microscope. *Phys. Rev. Lett.* **1986**, *56* (9), 930–933.

(20) Pohl, D. W.; Denk, W.; Lanz, M. Optical Stethoscopy: Image Recording with Resolution λ/20. *Appl. Phys. Lett.* **1984**, *44* (7), 651.

(21) Lewis, A.; Isaacson, M.; Harootunian, A.; Muray, A. Development of a 500 Å Spatial Resolution Light Microscope. *Ultramicroscopy* **1984**, *13* (3), 227–231.

(22) Betzig, E.; Chichester, R. J. Single Molecules Observed by Near-Field Scanning Optical Microscopy. *Science (80-.).* **1993**, *262* (5138), 1422–1425.

(23) van Hulst, N. F.; Veerman, J.-A.; García-Parajó, M. F.; Kuipers, L. (Kobus). Analysis of Individual (Macro)molecules and Proteins Using near-Field Optics. *J. Chem. Phys.* **2000**, *112* (18), 7799.

(24) Gersen, H.; García-Parajó, M. F.; Novotny, L.; Veerman, J. A.; Kuipers, L.; Van Hulst, N. F. Near-Field Effects in Single Molecule Emission. *J. Microsc.* **2001**, *202*, 374–378.

(25) Zenhausern, F.; Martin, Y.; Wickramasinghe, H. K. Scanning Interferometric Apertureless Microscopy: Optical Imaging at 10 Angstrom Resolution. *Science* **1995**, *269* (5227), 1083–1085.

(26) Knoll, B.; Keilmann, F.; Kramer, A.; Guckenberger, R. Contrast of Microwave near-Field Microscopy. *Appl. Phys. Lett.* **1998**, *70* (20), 2667.

(27) Hillenbrand, R.; Keilmann, F. Complex Optical Constants on a Subwavelength Scale. *Phys. Rev. Lett.* **2000**, *85* (14), 3029–3032.

(28) Kawai, S. Revealing Mechanical and Structural Properties of Molecules on Surface by High-Resolution Atomic Force Microscopy. *Polym. J.* **2017**, *49* (1), 3–11.

(29) Vohnsen, B.; Bozhevolnyi, S.; Olesen, R. Study of Shear Force Technique for near-Field Microscopy with an Uncoated Fiber Tip. *Ultramicroscopy* **1995**, *61* (1–4), 207–213.

(30) Durkan, C.; Shvets, I. V. Investigation of the Physical Mechanisms of Shear-Force Imaging. *J. Appl. Phys.* **1996**, *80* (10), 5659.

(31) Karraï, K.; Grober, R. D. Piezo-Electric Tuning Fork Tip—sample Distance Control for near

Field Optical Microscopes. *Ultramicroscopy* **1995**, *61* (1–4), 197–205.

(32) Ruiter, A. G. T.; van der Werf, K. O.; Veerman, J. A.; Garcia-Parajo, M. F.; Rensen, W. H. J.; van Hulst, N. F. Tuning Fork Shear-Force Feedback. *Ultramicroscopy* **1998**, *71* (1–4), 149–157.

(33) http://www.ntmdt.com/. Atomic Force Microscopy for Nanotechnology & Scientific Research | NT-MDT http://www.ntmdt.com/ (accessed Jun 12, 2015).

(34) A. Cvitkovic; N. Ocelic, A.; Hillenbrand, R. Material-Specific Infrared Recognition of Single Sub-10 Nm Particles by Substrate-Enhanced Scattering-Type Near-Field Microscopy. *Nano Lett.* **2007**, *7* (10), 3177–3181.

(35) Huth, F.; Govyadinov, A.; Amarie, S.; Nuansing, W.; Keilmann, F.; Hillenbrand, R. Nano-FTIR Absorption Spectroscopy of Molecular Fingerprints at 20 Nm Spatial Resolution. *Nano Lett.* **2012**, *12* (8), 3973–3978.

(36) Johnson, C. M.; Böhmler, M. Nano-FTIR Microscopy and Spectroscopy Studies of Atmospheric Corrosion with a Spatial Resolution of 20nm. *Corros. Sci.* **2016**, *108*, 60–65.

(37) Hillenbrand, R.; Stark, M.; Guckenberger, R. Higher-Harmonics Generation in Tapping-Mode Atomic-Force Microscopy: Insights into the Tip–sample Interaction. *Appl. PhysicsL etters* **2000**.

(38) Stark, R. W.; Heckl, W. M. Fourier Transformed Atomic Force Microscopy: Tapping Mode Atomic Force Microscopy beyond the Hookian Approximation. *Surf. Sci.* **2000**, *457* (1), 219–228.

(39) S. John T., J. van N.; Oscar H., W.; Kees O., van W.; Bart G., de G.; Greve. Mapping Electrostatic Forces Using Higher Harmonics Tapping Mode Atomic Force Microscopy in Liquid. *Langmuir* **1999**, *15* (21), 7101–7107.

(40) Diziain, S.; Adam, P. M.; Bijeon, J. L.; Lamy de la Chapelle, M.; Royer, P. Development of an Apertureless near-Field Optical Microscope for Fluorescence Imaging and Spectroscopy. *Synth. Met.* **2003**, *139* (3), 557–560.

(41) Kikuta, H.; Nasu, K.; Kato, N.; Iwata, K. Atomic Force Microscope Using Optical Heterodyne Detection Incorporated in an Optical Microscope. *Rev. Sci. Instrum.* **1995**, *66* (1), 87–90.

(42) Kim, M.-S.; Manzardo, O.; Dändliker, R.; Herzig, H. P.; Aeschimann, L.; Staufer, U.; Vettiger, P.; Lee, J.-H. Atomic Force Microscopy with Optical Heterodyne Detection Method. In *IEEE/LEOS Optical MEMS 2005: International Conference on Optical MEMS and Their Applications*; IEEE, 2005; pp 173–174.

(43) Ocelic, N.; Huber, A.; Hillenbrand, R. Pseudoheterodyne Detection for Background-Free near-Field Spectroscopy. *Appl. Phys. Lett.* **2006**, *89* (10), 101124.

(44) Keilmann, F.; Huber, A. J.; Hillenbrand, R. Nanoscale Conductivity Contrast by Scattering-Type Near-Field Optical Microscopy in the Visible, Infrared and THz Domains. *J. Infrared, Millimeter, Terahertz Waves* **2009**, *30* (12), 1255–1268.

(45) Amarie, S.; Zaslansky, P.; Kajihara, Y.; Griesshaber, E.; Schmahl, W. W.; Keilmann, F.

Nano-FTIR Chemical Mapping of Minerals in Biological Materials. *Beilstein J. Nanotechnol.* **2012**, *3* (1), 312–323.

(46) Lundeberg, M. B.; Gao, Y.; Woessner, A.; Tan, C.; Alonso-González, P.; Watanabe, K.; Taniguchi, T.; Hone, J.; Hillenbrand, R.; Koppens, F. H. L. Thermoelectric Detection and Imaging of Propagating Graphene Plasmons. *Nat. Mater.* **2016**, *16* (2), 204–207.

(47) Zheng, Z.; Wang, W.; Ma, T.; Deng, Z.; Ke, Y.; Zhan, R.; Zou, Q.; Ren, W.; Chen, J.; She, J.; Zhang, Y.; Liu, F.; Chen, H.; Deng, S.; Xu, N. Chemically-Doped Graphene with Improved Surface Plasmon Characteristics: An Optical near-Field Study. *Nanoscale* **2016**, *8* (37), 16621–16630.

(48) Gramotnev, D. K.; Bozhevolnyi, S. I. Plasmonics beyond the Diffraction Limit. *Nat. Photonics* **2010**, *4*, 83–91.

(49) Juan, M. L.; Righini, M.; Quidant, R. Plasmon Nano-Optical Tweezers. *Nat. Photonics* **2011**, *5*, 349–356.

(50) Kühn, S.; Håkanson, U.; Rogobete, L.; Sandoghdar, V. Enhancement of Single-Molecule Fluorescence Using a Gold Nanoparticle as an Optical Nanoantenna. *Phys. Rev. Lett.* **2006**, *97* (1), 17402.

(51) Höppener, C.; Novotny, L. Antenna-Based Optical Imaging of Single Ca2+ Transmembrane Proteins in Liquids. *Nano Lett.* **2008**, *8*, 642–646.

(52) Taminiau, T. H.; Stefani, F. D.; Segerink, F. B.; van Hulst, N. F. Optical Antennas Direct Single-Molecule Emission. *Nat. Photonics* **2008**, *2* (4), 234–237.

(53) Mivelle, M.; van Zanten, T. S.; Neumann, L.; van Hulst, N. F.; Garcia-Parajo, M. F. Ultrabright Bowtie Nanoaperture Antenna Probes Studied by Single Molecule Fluorescence. *Nano Lett.* **2012**, *12*, 5972–5978.

(54) Berthelot, J.; Aćimović, S. S.; Juan, M. L.; Kreuzer, M. P.; Renger, J.; Quidant, R. Three-Dimensional Manipulation with Scanning near-Field Optical Nanotweezers. *Nat. Nanotechnol.* **2014**, *9*, 295–299.

(55) Cunningham, S. L.; Maradudin, A. A.; Wallis, R. F. Effect of a Charge Layer on the Surface-Plasmon-Polariton Dispersion Curve. *Phys. Rev. B* **1974**, *10*, 3342–3355.

(56) Zayats, A. V.; Smolyaninov, I. I.; Maradudin, A. A. Nano-Optics of Surface Plasmon Polaritons. *Phys. Rep.* **2005**, *408* (3), 131–314.

(57) Nerkararyan, K. V. Superfocusing of a Surface Polariton in a Wedge-like Structure. *Phys. Lett. A* **1997**, *237*, 103–105.

(58) Babadjanyan, A. J.; Margaryan, N. L.; Nerkararyan, K. V. Superfocusing of Surface Polaritons in the Conical Structure. *J. Appl. Phys.* **2000**, *87*, 3785.

(59) Stockman, M. Nanofocusing of Optical Energy in Tapered Plasmonic Waveguides. *Phys. Rev. Lett.* **2004**, *93*, 137404.

(60) Ropers, C.; Neacsu, C. C.; Elsaesser, T.; Albrecht, M.; Raschke, M. B.; Lienau, C. Grating-Coupling of Surface Plasmons onto Metallic Tips: A Nanoconfined Light Source. *Nano Lett.* **2007**, *7*, 2784–2788.

(61) Berweger, S.; Atkin, J. M.; Olmon, R. L.; Raschke, M. B. Light on the Tip of a Needle: Plasmonic Nanofocusing for Spectroscopy on the Nanoscale. *J. Phys. Chem. Lett.* **2012**, *3* (7), 945–952.

(62) Umakoshi, T.; Saito, Y.; Verma, P.; Inouye, Y.; Iotti, S.; Rossinelli, A.; Norris, D. J.; Ishitobi, H.; Tarun, A.; Hayazawa, N.; Verma, P.; Inouye, Y.; Kawata, S.; Hillenbrand, R.; Koppens, F. H. L.; Cingolani, R.; Fabrizio, E. D. Highly Efficient Plasmonic Tip Design for Plasmon Nanofocusing in near-Field Optical Microscopy. *Nanoscale* **2016**, *8* (10), 5634–5640.

(63) De Angelis, F.; Das, G.; Candeloro, P.; Patrini, M.; Galli, M.; Bek, A.; Lazzarino, M.; Maksymov, I.; Liberale, C.; Andreani, L. C.; Di Fabrizio, E. Nanoscale Chemical Mapping Using Three-Dimensional Adiabatic Compression of Surface Plasmon Polaritons. *Nat. Nanotechnol.* **2010**, *5*, 67–72.

(64) Tortora, P.; Descrovi, E.; Aeschimann, L.; Vaccaro, L.; Herzig, H.-P.; Dändliker, R. Selective Coupling of HE11 and TM01 Modes into Microfabricated Fully Metal-Coated Quartz Probes. *Ultramicroscopy* **2007**, *107*, 158–165.

(65) Berweger, S.; Atkin, J.; Olmon, R. L.; Raschke, M. B. Adiabatic Tip-Plasmon Focusing for Nano-Raman Spectroscopy. *J. Phys. Chem. Lett.* **2010**, *1*, 3427–3432.

(66) Novotny, L.; Pohl, D. W.; Hecht, B. Light Confinement in Scanning near-Field Optical Microscopy. *Ultramicroscopy* **1995**, *61* (1–4), 1–9.

(67) Bouhelier, A.; Renger, J.; Beversluis, M. R.; Novotny, L. Plasmon-Coupled Tip-Enhanced near-Field Optical Microscopy. *J. Microsc.* **2003**, *210*, 220–224.

(68) Janunts, N.; Baghdasaryan, K.; Nerkararyan, K.; Hecht, B. Excitation and Superfocusing of Surface Plasmon Polaritons on a Silver-Coated Optical Fiber Tip. *Opt. Commun.* **2005**, *253*, 118–124.

(69) Tugchin, B. N.; Janunts, N.; Klein, A. E.; Steinert, M.; Fasold, S.; Diziain, S.; Sison, M.; Kley, E.-B.; Tünnermann, A.; Pertsch, T. Plasmonic Tip Based on Excitation of Radially Polarized Conical Surface Plasmon Polariton for Detecting Longitudinal and Transversal Fields. *ACS Photonics* **2015**, *2*, 1468–1475.

(70) Ding, W.; Andrews, S.; Maier, S. Internal Excitation and Superfocusing of Surface Plasmon Polaritons on a Silver-Coated Optical Fiber Tip. *Phys. Rev. A* **2007**, *75*, 63822.

(71) Barthes, J.; Colas des Francs, G.; Bouhelier, A.; Dereux, A. A Coupled Lossy Local-Mode Theory Description of a Plasmonic Tip. *New J. Phys.* **2012**, *14*, 83041.

(72) Ramachandran, S.; Kristensen, P.; Yan, M. F. Generation and Propagation of Radially Polarized Beams in Optical Fibers. *Opt. Lett.* **2009**, *34*, 2525.

(73) Bozinovic, N.; Yue, Y.; Ren, Y.; Tur, M.; Kristensen, P.; Huang, H.; Willner, A. E.; Ramachandran, S. Terabit-Scale Orbital Angular Momentum Mode Division Multiplexing in Fibers. *Science* **2013**, *340*, 1545–1548.

(74) Ramachandran, S.; Kristensen, P. Optical Vortices in Fiber. *Nanophotonics* **2013**, *2*, 455–474.

(75) Klein, A. E.; Janunts, N.; Steinert, M.; Tünnermann, A.; Pertsch, T. Polarization-Resolved near-Field Mapping of Plasmonic Aperture Emission by a Dual-SNOM System. *Nano Lett.*

2014, *14* (9), 5010–5015.

(76) Tugchin, B. N.; Janunts, N.; Steinert, M.; Dietrich, K.; Kley, E.-B.; Tünnermann, A.; Pertsch, T. Quasi-Linearly Polarized Modal Analysis of Aperture SNOM Tips: Understanding the Functionality of Aperture Tips. *New J. Phys.* **2017**, *19*, 63024.

(77) Lin, J.; Wang, H.; Zheng, W.; Lu, F.; Sheppard, C.; Huang, Z. Numerical Study of Effects of Light Polarization, Scatterer Sizes and Orientations on near-Field Coherent Anti-Stokes Raman Scattering Microscopy. *Opt. Express* **2009**, *17* (4), 2423.

(78) Stöckle, R.; Fokas, C.; Deckert, V.; Zenobi, R.; Sick, B.; Hecht, B.; Wild, U. P. High-Quality near-Field Optical Probes by Tube Etching. *Appl. Phys. Lett.* **1999**, *75* (2), 160.

(79) Lambelet, P.; Sayah, A.; Pfeffer, M.; Philipona, C.; Marquis-Weible, F. Chemically Etched Fiber Tips for Near-Field Optical Microscopy: A Process for Smoother Tips. *Appl. Opt.* **1998**, *37* (31), 7289.

(80) Garcia-Parajo, M.; Tate, T.; Chen, Y. Gold-Coated Parabolic Tapers for Scanning near-Field Optical Microscopy: Fabrication and Optimisation. *Ultramicroscopy* **1995**, *61* (1–4), 155–163.

(81) Williamson, R. L.; Miles, M. J. Melt-Drawn Scanning near-Field Optical Microscopy Probe Profiles. *J. Appl. Phys.* **1996**, *80* (9), 4804.

(82) Sutter Instrument Company. P-2000 Laser-Based Micropipette Puller http://www.sutter.com/MICROPIPETTE/p-2000.html.

(83) Synge, E. H. A Suggested Method for Extending Microscopic Resolution into the Ultra-Microscopic Region. *Philos. Mag. J. Sci.* **1928**, *6* (35), 356–362.

(84) Dürig, U.; Pohl, D. W.; Rohner, F. Near-Field Optical-Scanning Microscopy. *J. Appl. Phys.* **1986**, *59* (10), 3318.

(85) Isaacson, M.; Betzig, E.; Harootunian, A.; Lewis, A. Scanning Optical Microscopy at λ/10 Resolution Using Near-Field Imaging Methods. *Ann. N. Y. Acad. Sci.* **1986**, *483*, 448–456.

(86) Selvakumar, N.; Barshilia, H. C. Review of Physical Vapor Deposited (PVD) Spectrally Selective Coatings for Mid- and High-Temperature Solar Thermal Applications. *Sol. Energy Mater. Sol. Cells* **2012**, *98*, 1–23.

(87) Babayan, A. E.; Nerkararyan, K. V. The Strong Localization of Surface Plasmon Polariton on a Metal-Coated Tip of Optical Fiber. *Ultramicroscopy* **2007**, *107* (12), 1136–1140.

(88) Marcuse, D. *Light Transmission Optics*, 2nd ed.; Van Nostrand Reinhold Company Inc., 1982.

(89) Okamoto, K. *Fundamentals of Optical Waveguides*, 2nd ed.; Elsevier, 2006.

(90) Chavez-Pirson, A.; Chu, S. T. A Full Vector Analysis of near-Field Luminescence Probing of a Single Quantum Dot. *Appl. Phys. Lett.* **1999**, *74* (11), 1507.

(91) Kelso, C. M.; Flammer, P. D.; DeSanto, J. A.; Collins, R. T. Integral Equations Applied to Wave Propagation in Two Dimensions: Modeling the Tip of a near-Field Scanning Optical Microscope. *J. Opt. Soc. Am. A* **2001**, *18* (8), 1993.

(92) Bethe, H. A. Theory of Diffraction by Small Holes. *Phys. Rev.* **1944**, *66* (7–8), 163–182.

(93) Bouwkamp, C. On Bethe's Theory of Diffraction by Small Holes. *Philips Res. Rep.* **1950**, *5*, 321–332.

(94) Greffet, J.-J.; Carminati, R. Image Formation in near-Field Optics. *Prog. Surf. Sci.* **1997**, *56* (3), 133–237.

(95) Colas des Francs, G.; Girard, C.; Weeber, J.-C.; Dereux, A. Relationship between Scanning near-Field Optical Images and Local Density of Photonic States. *Chem. Phys. Lett.* **2001**, *345* (5–6), 512–516.

(96) Mueller, J. P. B.; Capasso, F. Asymmetric Surface Plasmon Polariton Emission by a Dipole Emitter near a Metal Surface. *Phys. Rev. B* **2013**, *88*, 121410.

(97) Thorlabs - 780HP Single Mode Optical Fiber, 780 - 970 nm, Ø125 µm Cladding https://www.thorlabs.com/thorproduct.cfm?partnumber=780HP.

(98) Sutter Instrument Company. P-2000 Laser-Based Micropipette Puller.

(99) Novotny, L.; Hecht, B. *Principles of Nano-Optics*, 2nd ed.; Cambridge University Press, 2006.

(100) Rakic, A. D.; Djurišic, A. B.; Elazar, J. M.; Majewski, M. L. Optical Properties of Metallic Films for Vertical-Cavity Optoelectronic Devices. *Appl. Opt.* **1998**, *37*, 5271.

(101) Bakunov, M. I.; Bodrov, S. B.; Hangyo, M. Intermode Conversion in a near-Field Optical Fiber Probe. *J. Appl. Phys.* **2004**, *96* (4), 1775.

(102) Novotny, L.; Hafner, C. Light Propagation in a Cylindrical Waveguide with a Complex, Metallic, Dielectric Function. *Phys. Rev. E* **1994**, *50*, 4094–4106.

(103) Verhagen, E.; Spasenović, M.; Polman, A.; Kuipers, L. Nanowire Plasmon Excitation by Adiabatic Mode Transformation. *Phys. Rev. Lett.* **2009**, *102* (20), 203904.

(104) Burresi, M.; Engelen, R. J. P.; Opheij, A.; van Oosten, D.; Mori, D.; Baba, T.; Kuipers, L. Observation of Polarization Singularities at the Nanoscale. *Phys. Rev. Lett.* **2009**, *102* (3), 33902.

(105) Lan, T.-H.; Tien, C.-H. Study on Focusing Mechanism of Radial Polarization with Immersion Objective. *Jpn. J. Appl. Phys.* **2008**, *47* (7), 5806–5808.

(106) Guo, L.; Min, C.; Wei, S.; Yuan, X. Polarization and Amplitude Hybrid Modulation of Longitudinally Polarized Subwavelength-SizedOptical Needle. *Chinese Opt. Lett.* **2013**, *11* (5), 52601.

(107) Snyder, A. W.; Love, J. *Optical Waveguide Theory*, 1st ed.; Springer, 1983.

(108) Katsenelenbaum, B. Z.; Mercader del Rio, L.; Pereyaslavets, M.; Sorolla Ayza, M.; Thumm, M. *Theory of Nonuniform Waveguides: The Cross-Section Method*; IET: The Institution of Engineering and Technology, Michael Faraday House, Six Hills Way, Stevenage SG1 2AY, UK, 1998.

(109) Fountaine, K. T.; Whitney, W. S.; Atwater, H. A. Resonant Absorption in Semiconductor Nanowires and Nanowire Arrays: Relating Leaky Waveguide Modes to Bloch Photonic

Crystal Modes. *J. Appl. Phys.* **2014**, *116* (15), 153106.

(110) Evlyukhin, A. B.; Eriksen, R. L.; Cheng, W.; Beermann, J.; Reinhardt, C.; Petrov, A.; Prorok, S.; Eich, M.; Chichkov, B. N.; Bozhevolnyi, S. I. Optical Spectroscopy of Single Si Nanocylinders with Magnetic and Electric Resonances. *Sci. Rep.* **2014**, *4*, 60–69.

(111) Mirzaei, A.; Shadrivov, I. V.; Miroshnichenko, A. E.; Kivshar, Y. S. Superabsorption of Light by Multilayer Nanowires. *Nanoscale* **2015**, *7* (42), 17658–17663.

(112) Fountaine, K. T.; Kendall, C. G.; Atwater, H. A. Near-Unity Broadband Absorption Designs for Semiconducting Nanowire Arrays via Localized Radial Mode Excitation. *Opt. Express* **2014**, *22* (S3), A930.

(113) Antosiewicz, T. J.; Szoplik, T. Corrugated Metal–coated Tapered Tip for Scanning Near–field Optical Microscope. *Opt. Express* **2007**, *15* (17), 10920.

(114) Kupec, J.; Witzigmann, B. Dispersion, Wave Propagation and Efficiency Analysis of Nanowire Solar Cells. *Opt. Express* **2009**, *17* (12), 10399.

(115) Heinzelmann, H.; Pohl, D. W. Scanning near-Field Optical Microscopy. *Appl. Phys. A Solids Surfaces* **1994**, *59* (2), 89–101.

(116) Hecht, B.; Bielefeldt, H.; Novotny, L.; Inouye, Y.; Pohl, D. Local Excitation, Scattering, and Interference of Surface Plasmons. *Phys. Rev. Lett.* **1996**, *77* (9), 1889–1892.

(117) Babadjanyan, A. J.; Margaryan, N. L.; Nerkararyan, K. V. Superfocusing of Surface Polaritons in the Conical Structure. *J. Appl. Phys.* **2000**, *87*, 3785.

(118) Lee, J. S.; Han, S.; Shirdel, J.; Koo, S.; Sadiq, D.; Lienau, C.; Park, N. Superfocusing of Electric or Magnetic Fields Using Conical Metal Tips: Effect of Mode Symmetry on the Plasmon Excitation Method. *Opt. Express* **2011**, *19* (13), 12342.

(119) Thu, N. T.; Tanaka, K.; Tanaka, M.; Chien, D. N. Superfocusing of Surface Plasmon Polaritons by Metal-Coated Dielectric Probe of Tilted Conical Shape. *J. Opt. Soc. Am. A* **2013**, *30* (6), 1113.

(120) Lindquist, N. C.; Nagpal, P.; Lesuffleur, A.; Norris, D. J.; Oh, S.-H. Three-Dimensional Plasmonic Nanofocusing. *Nano Lett.* **2010**, *10* (4), 1369–1373.

(121) Tugchin, B. N.; Janunts, N.; Steinert, M.; Dietrich, K.; Sivun, D.; Ramachandran, S.; Nerkararyan, K. V.; Tünnermann, A.; Pertsch, T. Controlling the Excitation of Radially Polarized Conical Plasmons in Plasmonic Tips in Liquids. *RSC Adv.* **2016**, *6* (58), 53273–53281.

(122) Betzig, E.; Lewis, A.; Harootunian, A.; Isaacson, M.; Kratschmer, E. Near Field Scanning Optical Microscopy (NSOM). *Biophys. J.* **1986**, *49* (1), 269–279.

(123) Betzig, E.; Harootunian, A.; Lewis, A.; Isaacson, M. Near-Field Diffraction by a Slit: Implications for Superresolution Microscopy. *Appl. Opt.* **1986**, *25* (12), 1890.

(124) Nerkararyan, K. Superfocusing of a Surface Polariton in a Wedge-like Structure. *Phys. Lett. A* **1997**, *237*, 103–105.

(125) Stockman, M. Nanofocusing of Optical Energy in Tapered Plasmonic Waveguides. *Phys. Rev. Lett.* **2004**, *93*, 137404.

(126) Gramotnev, D. K.; Vogel, M. W.; Stockman, M. I. Optimized Nonadiabatic Nanofocusing of Plasmons by Tapered Metal Rods. *J. Appl. Phys.* **2008**, *104* (3), 34311.

(127) Bouhelier, A.; Beversluis, M.; Novotny, L. Plasmon Coupled Tip-Enhanced near-Field Optical Microscopy. In *Summaries of Papers Presented at the Quantum Electronics and Laser Science Conference*; Opt. Soc. America; p 134.

(128) Yatsui, T.; Kourogi, M.; Ohtsu, M. Highly Efficient Excitation of Optical near-Field on an Apertured Fiber Probe with an Asymmetric Structure. *Appl. Phys. Lett.* **1997**, *71* (13), 1756.

(129) Neacsu, C. C.; Berweger, S.; Olmon, R.; Saraf, L. V; Ropers, C.; Raschke, M. B. Near-Field Localization in Plasmonic Superfocusing: A Nanoemitter on a Tip. *Nano Lett.* **2010**, *10* (2), 592–596.

(130) Brünning, R.; Tugchin, B. .; Zimmermann, F.; Schröter, S.; Janunts, N.; Nolte, S.; Pertsch, T.; Duparré, M. Excitation of Conical Vector Plasmonic Modes in Vortex-Fiber-Plasmonic Tip. *Manuscript-in-preparation*.

(131) Valaskovic, G. A.; Holton, M.; Morrison, G. H. Parameter Control, Characterization, and Optimization in the Fabrication of Optical Fiber near-Field Probes. *Appl. Opt.* **1995**, *34* (7), 1215–1228.

(132) Bartelt, H.O.; Lohmann, A.W.; Freude, W.; Grau, G. K. Mode Analysis of Optical Fibres Using Computer-Generated Matched Filters. *Electron. Lett.* **1983**, *19* (7), 247–249.

(133) Nicholson, J. W.; Yablon, A. D.; Ramachandran, S.; Ghalmi, S. Spatially and Spectrally Resolved Imaging of Modal Content in Large-Mode-Area Fibers. *Opt. Express* **2008**, *16* (10), 7233.

(134) Nguyen, D. M.; Blin, S.; Nguyen, T. N.; Le, S. D.; Provino, L.; Thual, M.; Chartier, T. Modal Decomposition Technique for Multimode Fibers. *Appl. Opt.* **2012**, *51* (4), 450–456.

(135) Fatemi, F. K.; Beadie, G. Rapid Complex Mode Decomposition of Vector Beams by Common Path Interferometry. *Opt. Express* **2013**, *21* (26), 32291.

(136) Flamm, D.; Naidoo, D.; Schulze, C.; Forbes, A.; Duparré, M. Mode Analysis with a Spatial Light Modulator as a Correlation Filter. *Opt. Lett.* **2012**, *37* (13), 2478.

(137) Zeeb, B.; Jäger, S.; Schäfer, C.; Nill, P.; Meixner, A. J.; Kern, D. P.; Fleischer, M. Self-Aligned Gold Nanocone Probe Tips. *J. Vac. Sci. Technol. B Microelectron. Nanom. Struct.* **2010**, *28* (6), C6O34.

(138) Duan, J. L.; Lei, D. Y.; Chen, F.; Lau, S. P.; Milne, W. I.; Toimil-Molares, M. E.; Trautmann, C.; Liu, J. Vertically-Aligned Single-Crystal Nanocone Arrays: Controlled Fabrication and Enhanced Field Emission. *ACS Appl. Mater. Interfaces* **2016**, *8* (1), 472–479.

(139) Carta, S.; Bagni, R.; Giovine, E.; Foglietti, V.; Evangelisti, F.; Notargiacomo, A. Fabrication of Bulk and Epitaxial Germanium Field Emitter Arrays by Dry Etching Techniques. *Microelectron. Eng.* **2013**, *110*, 230–233.

(140) Jung, B. J.; Kong, H. J.; Cho, Y.-H.; Park, C. H.; Kim, M. K.; Jeon, B. G.; Yang, D.-Y.; Lee, K.-S. Fabrication of 15 Nm Curvature Radius Polymer Tip Probe on an Optical Fiber via Two-Photon Polymerization and O2-Plasma Ashing. *Curr. Appl. Phys.* **2013**, *13* (9), 2064–

2069.

(141) Xie, F. Y.; Gong, L.; Liu, X.; Chen, J.; Xie, W. G.; Zhang, W. H.; Chen, S. H. Preparation and Characterization of the Amorphous Tungsten Cone Field Emitter Arrays by Ar+ Etching. *Appl. Surf. Sci.* **2009**, *256* (3), 693–697.

(142) Li, Y. L.; Shi, C. Y.; Li, J. J.; Gu, C. Z. Local Field-Emission Characteristic of Individual AlN Cone Fabricated by Focused Ion-Beam Etching Method. *Appl. Surf. Sci.* **2008**, *254* (15), 4840–4844.

(143) Hoffrogge, P.; Kopf, H.; Reichelt, R. Nanostructuring of Tips for Scanning Probe Microscopy by Ion Sputtering: Control of the Apex Ratio and the Tip Radius. *J. Appl. Phys.* **2001**, *90* (10), 5322–5327.

(144) Tugchin, B. N. Resonant Excitation of Conical Surface Plasmon Polaritons in Conical Metallic Structure, Friedrich-Schiller- Universität Jena, 2012.

(145) Richards, B.; Wolf, E. Electromagnetic Diffraction in Optical Systems. II. Structure of the Image Field in an Aplanatic System. *Proc. R. Soc. A Math. Phys. Eng. Sci.* **1959**, *253*, 358–379.

(146) Youngworth, K.; Brown, T. Focusing of High Numerical Aperture Cylindrical-Vector Beams. *Opt. Express* **2000**, *7*, 77.

(147) Yew, E. Y. S.; Sheppard, C. J. R. Tight Focusing of Radially Polarized Gaussian and Bessel-Gauss Beams. *Opt. Lett.* **2007**, *32*, 3417.

(148) Younesi, M. Probing Focused Beam with Different Metallic Tips, Internship report, Friedrich-Schiller-Universität Jena, 2016.

(149) Krzic, A. Plasmonic Tip Based Optical Setup for Investigating Intensities of Transversal and Longitudinal Components of Focused Beam, Internship report, Friedrich-Schiller-Universität Jena, 2015.

(150) Bouhelier, A.; Beversluis, M. R.; Novotny, L. Near-Field Scattering of Longitudinal Fields. *Appl. Phys. Lett.* **2003**, *82* (25), 4596.

(151) Particles - Polystyrene- Coated- Flow Cytometry- PMMA - Kisker Produkte - Kisker Biotech http://www.kisker-biotech.com/frontoffice/product?produitId=KI0A-11-01 (accessed Feb 8, 2017).

(152) Bozhevolnyi, S. I. Topographical Artifacts and Optical Resolution in near-Field Optical Microscopy. *J. Opt. Soc. Am. B* **1997**, *14* (9), 2254.

(153) Azoulay, J.; Débarre, A.; Richard, A.; Tchénio, P. Quenching and Enhancement of Single-Molecule Fluorescence under Metallic and Dielectric Tips. *Europhys. Lett.* **2000**, *51* (4), 374–380.

(154) Anger, P.; Bharadwaj, P.; Novotny, L. Enhancement and Quenching of Single-Molecule Fluorescence. *Phys. Rev. Lett.* **2006**, *96* (11), 113002.

(155) Billaud, P.; Marhaba, S.; Grillet, N.; Cottancin, E.; Bonnet, C.; Lermé, J.; Vialle, J.-L.; Broyer, M.; Pellarin, M. Absolute Optical Extinction Measurements of Single Nano-Objects by Spatial Modulation Spectroscopy Using a White Lamp. *Rev. Sci. Instrum.* **2010**, *81* (4),

43101.

(156) Hamann, H. F.; Kuno, M.; Gallagher, A.; Nesbitt, D. J. Molecular Fluorescence in the Vicinity of a Nanoscopic Probe. *J. Chem. Phys.* **2001**, *114* (19), 8596.

(157) Fragola, A.; Aigouy, L.; Boccara, C. Interference Effect in Apertureless near-Field Fluorescence Imaging. *Appl. Opt.* **2003**, *42* (34), 6880.

(158) Diziain, S.; Adam, P.-M.; Bijeon, J.-L.; Royer, P. Coherent Scattering Phenomena in Apertureless Scanning near-Field Fluorescence Microscopy. *Opt. Commun.* **2007**, *276* (1), 180–185.

(159) Moerner, W. E.; Fromm, D. P. Methods of Single-Molecule Fluorescence Spectroscopy and Microscopy. *Rev. Sci. Instrum.* **2003**, *74* (8), 3597–3619.

(160) Younesi, M. Scattering Properties of Scanning near-Field Optical Microscopy Tips, Master thesis, Friedrich-Schiller-Universität Jena, 2017.

(161) Bidault, S.; Devilez, A.; Maillard, V.; Lermusiaux, L.; Guigner, J.-M.; Bonod, N.; Wenger, J. Picosecond Lifetimes with High Quantum Yields from Single-Photon-Emitting Colloidal Nanostructures at Room Temperature. *ACS Nano* **2016**, *10* (4), 4806–4815.

(162) Koenderink, A. F. Single-Photon Nanoantennas. *ACS Photonics* **2017**, *4* (4), 710–722.